Semiconductor surface plasmons: a route to terahertz waveguides and sensors

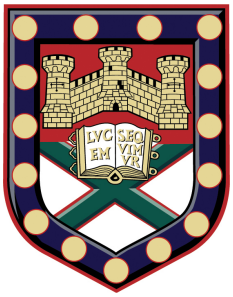

Edmund Keith Stone

School of Physics

University of Exeter

A thesis submitted for the degree of

Doctor of Philosophy

March 2012

Semiconductor surface plasmons: a route to terahertz waveguides and sensors

Submitted by Edmund Keith Stone to the University of Exeter as a thesis for the degree of Doctor of Philosophy in Physics
2012

I certify that all material in this thesis which is not my own work has been identified and that no material has previously been submitted and approved for the award of a degree by this or any other University.

Edmund Keith Stone
2012

I would like to dedicate this thesis to Phyllis Mary Hamblen my loving gran who passed away during my second year.

Acknowledgements

During my time at Exeter many people have helped me, kept me sane and fed the insanity, all of which seem to be required for completing a PhD. To all those people, thank you. Lots are listed below, those who are not, I am sorry.

A special thank you must be said to my supervisor. Euan's enthusiasm for science is unshakable and affects all those around him. Even when the list of failed attempts appeared unending he was still positive. On a similar note, Professor Roy Sambles, thank you for suggesting my name to Euan and for your help in group meetings. Without my first summer project with you I'm not sure I would be writing a thesis currently. Tom Isaac, I am indebted to for teaching me all he knew about terahertz spectroscopy. Tom, the lock-in amplifier still only works if you catch it off guard when switching it on. During my time I have become more worried about the apparent sentience of some of our equipment.

I'd like to thank Professor Bill Barnes for many useful meetings whether it was 'back to basics,' terahertz or generation orientated. Always happy, and friendly with an insightful comment on the subject at hand. A great contributor to those early meetings was Baptiste, who along with Martin, Tim A, Tim T, John, Joe and Steph showed me just how interesting a PhD could be during my summer projects as an undergraduate. Others from the group who have moved on, Chris Burrows and James Parsons, you guys helped a lot with HFSS. James, your antics in the basement are still the topic of discussion, soon I feel the stuff of legend. Not forgetting Andy and George, your knowledge of the FIB and SEM was indispensable.

Matt L and Ian, as much as you might not like to admit it, you are both full of knowledge and happy to spread it about and help people, and between the unreproducible comments the discussions are nearly always useful. Two fellow terahertz spectroscopers, thanks for all your help Dmitry and Rostislav.

Matt B, Helen and Liz, since being undergrads together it's always been good to have a chat with you guys. Mel, thanks for helping me with maths when I hit a brick wall, even when the questions were ridiculously simple and I'd argued myself into a hole. It was always a pleasure helping you with your computer woes. Also, Mel, thanks for talking me through the panic, you'll be a great teacher! Celia, you should probably be mentioned several times in this section but tough. Thank you for all the talks, whether physics or unrelated, both at network and in uni you have always been a help and had

sensible words of advice. Tim 'starkles' Starkey, you are a unique individual, whether you're fighting with HFSS or looking confused at experiments it's always interesting. I'd like to thank the other members of the electromagnetics group who I've not named specifically and also the guys in other groups who've been good to talk to especially graphene about fabrication issues. On that note Pete Hale and Sam Hornett, two more of Euan's students who have a wealth of knowledge and are happy to pass it on when it's needed. And of course the workshop guys, Nick Cole especially, with Pete Cann, and Adam and Dave for finding me Helium when I was desperate to get some experiments done before the laser moved to its new home.

I did some demonstrating whilst doing my PhD, second year labs would not have been the same if it were not for Martin Smith, Lee Summers, and Steve Hubbard (and others mentioned in other places here), thank you guys for keeping me sane, especially you Lee, if the astro doesn't work out you can always be a stand up.

There are several people who might be thinking they have been forgotten at this point, but a special mention has to go with those of us who spend our time in the basement of physics. Alfie, you are annoyingly funny, despite your similarities to Holmes. Steve, thanks for the discussions especially recently. Matt N, you missed the best times in the basement, sorry about that. Tom C, having you in the same office has been useful for someone to bounce ideas off, I hope I've helped you in the same way. Your proof reading of some of the chapters below was indispensable, thank you. Finally for physics, Caroline and Chris 'CJ' 'Holmesey' Holmes. I have spent most of the last 4 years with you guys. There is so much to say, the arguing, the word game, the list is pretty long. Thank you. Chris, you annoyed me greatly at some points, earthquakes, and using me as a drum kit are two things that spring to mind. But despite that you are a great friend and someone who I hope I do not lose contact with. Likewise Caroline, there are many things that could go here, none of which you would like me to write, I therefore will not. Just a heartfelt thank you, finish soon, we never did find the time to play a game of mini golf. I think that pretty much completes the list of people from physics, if I've missed you, sorry.

Outside physics there are a group of people who have helped keep me routed. Helped distract me when I've needed it and helped me get to this point in my life. My parents of course, they have always believed in me and supported me through everything I have done. If it was not for the way they have brought me up I do not know where I would be at this point. I should also thank my brother, Tris, for constantly suggesting I could wear things as a special hat. When Celia first met Tris, she was surprised as from when I talked about him she had assumed I was the older brother.

Some friends and influences from other places have also enabled me to get to this point. Friends from scouting, especially James and Matt, two of my oldest friends who

are always good for a distraction. And Mr Bushrod, a great inspiration, my first real science teacher when I was around 9 years old, he inspired me to find out how the world worked with some truly great teaching.

Lastly, Sarah, thank you for being honest and for being there, when discussing me day with you, you always listened and then pointed out you didn't know what I was talking about. And of course thank you for making me some amazing food, your cheesecake is just fantastic.

Abstract

The terahertz regime has until recently been some what neglected due to the difficulty of generating and measuring terahertz radiation. Terahertz time domain spectroscopy has allowed for affordable and broadband probing of this frequency regime with phase sensitive measurements (chapter 3). This thesis aims to use this tool to add to the knowledge of the interactions between electromagnetic radiation and matter specifically in regard to plasmonics.

This thesis covers several distinct phenomena related to plasmonics at terahertz frequencies. The generation of terahertz radiation from metal nanoparticles is first described in chapter 4. It is shown that the field strength of the plasmon appears to relate to the strength of the generated field. It is also shown that the power dependence of the generated terahertz radiation is not consistent with the optical rectification description of this phenomenon. An alternative explanation is developed which appears more consistent with the observations. A simple model for the power dependence is derived and compared to the experimental results.

In chapter 5 the parameters that make good plasmonic materials are discussed. These parameters are used to assess the suitability of semiconductors for terahertz surface plasmon experiments. The Drude permittivity of InSb is measured here, leading to a discussion of terahertz particle plasmons in chapter 6. Finite element method modelling is used to show some merits of these over optical particle plasmons. This also includes a discussion of fabrication methods for arrays of these particles.

Finally, chapter 7 is a discussion of so called spoof surface plasmons. This includes some experimental work at microwave frequencies and an in depth analysis of open ended square hole arrays supported by model matching method modelling. Perfect endoscope effects are discussed and compared to superlensing. The thesis ends with a brief conclusions chapter where some of the ideas presented are brought together.

Contents

Contents vi

List of Figures ix

Nomenclature xviii

1 Introduction 1

2 Theory 4

2.1 Surface plasmons . . . 4

2.1.1 Dispersion relation of surface plasmons . . . 5

2.1.2 Surface plasmon polariton length scales . . . 8

2.1.3 Surface plasmon coupling methods . . . 11

2.2 Drude model . . . 12

2.3 Localised surface plasmons resonances . . . 15

2.3.1 Quasi-static approximation . . . 16

3 Methods 19

3.1 THz Spectroscopy . . . 19

3.1.1 Generation and detection . . . 23

3.1.2 Photodiode detectors . . . 29

3.2 Sample self adhesive support . . . 32

3.3 Optical spectra . . . 32

3.4 Finite Element Method Modelling . . . 33

3.4.1 Boundaries . . . 34

3.4.2 Incident wave solutions . . . 35

3.4.3 Eigenmode solutions . . . 35

3.4.4 Element meshing . . . 36

3.4.5 Uses . . . 36

4 Nanoparticle plasmonic generation of terahertz radiation **37**
4.1 Samples . . . 38
4.2 Experimental set up . . . 41
4.3 Islandised films . . . 42
4.4 Nanosphere lithography arrays . . . 43
4.4.1 Thickness dependency . . . 44
4.4.1.1 Experimental results . . . 44
4.4.1.2 Numerical modelling . . . 45
4.4.2 Optical intensity dependency . . . 49
4.4.2.1 Simple model . . . 49
4.4.3 Angle dependence . . . 53
4.5 Conclusions and future proposals . . . 55

5 Terahertz plasmonic materials **56**
5.1 Drude parameters of optical plasmonic metals . . . 56
5.2 Drude model and semiconductors . . . 57
5.3 Terahertz plasmonic materials . . . 59
5.3.1 Measuring the Drude parameters . . . 59
5.3.2 Results . . . 61
5.3.2.1 Temperature dependence . . . 63
5.3.3 Comparison between semiconductors . . . 66
5.3.3.1 Modelling of gratings with different semiconductors . . . 68
5.3.4 Photoexcitation of InSb . . . 70
5.4 Conclusions . . . 76

6 Terahertz particle plasmons **77**
6.1 Fabrication . . . 80
6.1.1 Chemical wet etch . . . 80
6.1.2 Focused ion beam . . . 82
6.1.2.1 Post etching positioning . . . 83
6.1.2.2 Results . . . 85
6.1.3 Reactive ion etching and chromium masks . . . 86
6.2 Modelling results . . . 89
6.2.1 Particle pairs . . . 91
6.2.2 Varying sharpness . . . 92
6.2.3 Photomodulation . . . 97
6.3 Conclusions . . . 98

7 Surface modes on open ended hole arrays **99**
7.0.1 Terahertz hole array measurement . . . 99
7.0.2 Motivations . . . 100
7.1 Theoretical formalism . . . 101
7.1.1 Modal matching approach . . . 101
7.1.2 Dispersion relations . . . 105
7.2 Results and discussion . . . 108
7.2.1 Measurement of surface mode dispersion . . . 108
7.2.2 Asymptotic frequencies and mode splitting . . . 112
7.3 Role of surface modes in hole arrray transmission . . . 114
7.3.1 Near field transmission of hole arrays . . . 114
7.3.2 Far field transmission of hole arrays . . . 117
7.4 Conclusions . . . 118

8 Conclusions and future work **121**
8.1 Publications . . . 122

References **123**

List of Figures

2.1 An incident p-polarised electromagnetic wave on the interface between two materials of different permittivity (ϵ_d and ϵ_m). 5

2.2 The dispersion relation for silver using a frequency dependent permittivity found from the Drude model 8

2.3 The field confinement in the z direction (normal to the surface) using a permittivity found using the Drude parameters of silver, (a) into the metal, and (b) into the dielectric, ... 10

2.4 A schematic of the electric fields on the metal-dielectric interface for a surface plasmon polariton, the decay into the metal and dielectric are shown. For any moment in time the field must change direction along the surface as the surface charge wave is longitudinal. 11

2.5 Schematic diagram of the blade coupling method, a form of scattering coupling. 12

2.6 The path traced by an electron in a metal according to the Drude model. The electron undergoes many random scattering events resulting in a random walk. The solid line indicates the situation where there is no applied electric field and the dotted line the case when there is an applied electric field resulting in a drift velocity v_d. 14

2.7 Example complex permittivity for metals in the optical regime, the solid lines represent the real part, and the dashed lines the imaginary part, for (a) silver and (b) aluminium, found using the Drude model. 15

3.1 Schematic of the focusing terahertz time domain spectrometer (THz-TDS) used in this project, the optical 800nm path is shown in red with the terahertz beam path shown in green. 20

3.2 (a) Schematic of the collimated terahertz time domain spectrometer (THz-TDS) in the transmission configuration used in this project, the optical 800nm path is shown in red with the terahertz beam path shown in green. (b) Schematic of the dry air box section of the collimated THz-TDS in the reflection configuration. 20
3.3 Example traces from a THz-TDS setup, (a) shows the time domain trace, whereas (b) shows the modulus of the complex frequency domain trace, also shown is the phase measured through the system. 23
3.4 An example photoconductive device, a bias voltage is applied across the antenna gap, when the incident optical pulse excites charge carriers their resultant acceleration results in an emitted pulse of terahertz radiation. 24
3.5 (a) The atomic structure of ZnTe . (b) The non-linear potential due to the assymetric bond between the Zn and Te atoms. (c) the optical excitation pulse, with the induced polarisation in a very thin non-linear crystal, and the resulting terahertz pulse. 26
3.6 The dependence of the peak terahertz electric field on the fluence of the generating optical pulse for ZnTe (solid line), a non-linear optical rectification crystal, and a photoconductive antenna device (dotted line) with a 4 kV bias voltage. 28
3.7 The three considered circuit diagrams for balanced photodiodes. It should be noted that these diagrams are simplified containing only the most important components. (a) The situation where the diodes are unpowered and in parallel, their direct differential is then amplified. (b) Has two 'pre-amps', one for each of the diodes, the differential operation is conducted using an op-amp. (c) The pre-amps and differential amplifier are supplemented by a sample and hold stage to conduct the stretching, this is then amplified by a fourth op-amp. 31
3.8 The time domain transmission through 4 different self adhesive pressure sensitive films, shown with a free space transmission through the focussing THz spectrometer. 33

4.1 A schematic of the proposed generation method. 38
4.2 A scanning electron microscope image of an islandised film, with a mass-thickness of 12 nm, the narrow channels the film are clearly illustrated. 39
4.3 Nanosphere lithography process for fabricating nanoscale triangles. . . . 40
4.4 A scanning electron microscope image of an array of triangles fabricated using 780 nm diameter spheres using nanosphere lithography with a deposited metal depth of 50 nm. 40

4.5 Optical extinction spectra for islandised films, and triangles fabricated by nanosphere lithography. 41
4.6 The peak terahertz intensity measured from islandised films with different mass-thickness. 42
4.7 (a) The time domain generated terahertz transmission from a 1 mm ⟨1 1 0⟩ ZnTe crystal (dashed line), and an array of triangular particles fabricated from nanosphere lithography using 780 nm (solid line) diameter spheres. (b) The frequency domain measurements of the generated terahertz signal, also shown (as the dotted line) is an array of triangles fabricated using and 390 nm diameter spheres. 43
4.8 Dependence of the peak generated terahertz intensity on the thickness of particles at normal incidence (solid line, filled circles) and an inclination angle (angle of incidence) of 40° (dashed line, filled squares). The lines are shown to guide the eye. Both datasets are normalised to their respective peaks and the normal incidence measurements are around a factor of 10 smaller. The arrays was fabricated using 780 nm diameter spheres. 44
4.9 Characteristic field enhancement distributions for 40 nm thick curved particles in a rhombic unit cell calculated using finite element modelling, illuminated with a wavelength of 800 nm. (a) In cross-section, where the inset shows the probe position for the maximum field enhancement plots. (b) Looking in plan of the particles. 45
4.10 The dipolar plasmon resonance shown in the reflection spectra for different realistic modifications, modelled for triangles made from spheres with a diameter of 780 nm. 46
4.11 The realistic modifications made to the model. (a) The starting point with straight pointed triangles, (b) The difference between the straight sided and sloped particles, (c) The modification to the straight triangles to make the sides and points curved, and (d) showing the modification to the top (and bottom) edges to include a small amount of curvature. 47
4.12 Results of numerical modelling for curved triangular particles with rounded edges, (a) reflection spectra for different thicknesses, $h = 20$, 30, 40, 50, 60, and 90 nm, the arrow shows the direction of increasing thickness and (b) the dependence of the peak field enhancements at 800 nm on the thickness of particles at normal incidence. 48

4.13 Dependence of generated terahertz fluence as a function of the intensity of the optical pulse incident onto the sample. ZnTe is shown as the circles and dashed line, with the squares and solid lines representing measurements of a NSL fabricated array, using spheres of diameter 780 nm and with a particle thickness of 50 nm. 50
4.14 Measured angle dependence of the generated terahertz intensity, from an array of 50 nm thick triangles fabricated using NSL with spheres of diameter 780 nm. Also shown are two predictions from (4.16) where $n_4 = 1$ (the dashed line) and $n_4 = 5$ (the doted line). 54

5.1 Schematic of idealised conduction and valence electron bands for metals, semiconductors and insulators. The Fermi level is indicated by E_F, up to which the electron states are filled. 58
5.2 Schematic of the transmission through a slab of material with refractive index n_2. 60
5.3 (a) Real and (b) imaginary parts of the transmission of the two silicon samples in the frequency domain. Also shown is the (c) real and (d) imaginary parts of the permittivity found from the fitting parameters. The experimental results are show as symbols and the lines are the fits. Sample a is shown as the circles and solid lines and sample b as the diamonds and dashed lines. 62
5.4 (a) Time domain and (b) real and (c) imaginary parts of the Fourier transformed frequency domain of the transmission through InSb sample at room temperature. The time domain results are only experimental. In the frequency domain the experimental results are represented as a symbol for every 75^{th} data point and the lines are the fits. (d) Shows the permittivity from the fitted Drude parameters, the solid line is the real part and the dashed imaginary. The inset shows where the real permittivity crosses -1 (shown as the dashed straight line). 64
5.5 The extracted (a) scattering rate and (b) plasma frequency from the InSb sample at various temperatures. 65

5.6 A log log plot of the surface plasmon frequency (ω_{sp}) plotted against the scattering rate (γ) for different semiconductors found in the literature (open shapes) and measured in this paper (filled shapes). The black data points represent room temperature measurements, red ones are above room temperature and blue below. It is discussed in the text that ω_{sp} needs to be in the range of typical terahertz time domain spectrometers ($0.2 \rightarrow 2$ THz, the shaded region) with γ as low as possible. It can therefore be said that InSb is the best candidate for terahertz plasmonic experiments. The bold silicon result is used below for modelling. 66
5.7 Schematic of the grating profile used for the finite difference time domain modelling. 68
5.8 Finite difference time domain results for a monograting with a mark to space ratio of 50%. The depth of the grating is varied showing the changing coupling efficiency. The two panels are (a) InSb using the Drude parameters found above, and (b) silicon using Drude parameters from the literature. 69
5.9 Schematic of the focusing terahertz spectrometer with a third path, allowing the sample to be optically pumped. 70
5.10 Time domain transmission measurement of InSb at 10 K with no photoexcitation (solid line) and illuminated by a 400 nm pulse (dashed line). 71
5.11 Decay of the induced reduction in the terahertz transmission with time from an optical photoexcitation pulse. Each sub figure shows various temperatures (indicated in the figure) for a single fluence. The fluences are described in the text where (a) shows *iii*, and (b) shows *iv*. 72
5.12 Three consecutive measurements of the photoexcitation decay using pump fluence *iv* at a temperature of 100 K. The first measurement is the solid line with the first repeat being the dotted line and the second the dashed one. 73
5.13 Schematic of the conduction and valence bands showing filled electron states as the system is photoexcited. (a) When the system starts without being photoexcited, and (b) where the system has already been photoexcited. 73
5.14 Decay of the induced reduction in the terahertz transmission with time from an optical photoexcitation pulse. Each sub figure shows various fluences (indicated in each figure) for a single temperature. The temperatures are (a) 50K, and (b) 150K. 74

5.15 The first part of the decay trace measured at 10 K with pump fluence *iii* (symbols are the measured values). The rise time can be seen with a fitted Gaussian function (solid line) with a full width half maxima of 27 ps. 75
5.16 Schematic showing impact ionisation. Here energy from the photoexcited electron a is transfered to electron b as it decays to c, providing energy for b to be excited to d. 75

6.1 A schematic of the unit cell for pillar localised surface plasmon resonances with example field profiles. 78
6.2 Reflection spectra for InSb rods (a) connected by an InSb substrate with varying particle heights, $h = 10\ \mu m, 50\ \mu m, 100\ \mu m$ and 150 µm, and (b) disconnected square rods ($h = 10\ \mu m$). The dimensions of the rods modelled are length 20 µm, and width 10 µm, with a separation between the particles of 10 µm. The array has a long axis pitch of 60 µm and short axis pitch of 20 µm. 79
6.3 Snapped side of InSb wafers at 35° where the scale bars are 100 µm. (a) An unetched wafer, some stress damage from breaking the sample can be seen, (b) a sample etched using a lactic and nitric acid mix, where the etchant was only incident on the top surface, damage can be seen over 200 µm under the surface of the sample, and (c) the material has been etched by $\approx 250\ \mu m$ in nitric acid no damage other than that due to the stress on breaking the sample can be seen. 81
6.4 The surface of an InSb wafer after etching in nitric acid, (a) an optical microscope image and (b) an SEM image, where the scale bar is 20 µm. 82
6.5 The surface of an InSb wafer after etching in nitric acid with a chromium mask of curved triangles being deposited before etching. This is an optical microscope image, the base to point length of each triangle is around 100 µm. 83
6.6 (a) Schematic view showing the four cuts required to cut a triangular prism particle using a FIB on a flat InSb substrate, the cuts are tapered slightly similar to the shape of the FIB. (b) Three remaining particles on the side of an InSb wafer after teeth have been etched into the edge of the angled side of the wafer before another cut is made to remove the particles from the substrate. (c) An SEM image of a single particle cut from the side of the wafer. 84

6.7 An optical microscope image showing the positioning of the triangular shaped particles cut using the FIB. The red mark is a positioning point. The cuts into the substrate in the bottom right are where the particles were made. 85
6.8 (a) A SEM image of the array of triangles cut using a FIB and positioned using a micropositioner. The outer ring is a metallic aperture. (b) The normalised transmission intensity measured through the InSb particles. 86
6.9 Two regions of the same sample after the lift off procedure. Remaining on the surface should be chromium triangles on a PMMA protective layer on an InSb substrate. The difference between the regions is very visible. The base to point length of the triangles is 100 µm. 88
6.10 Curling of the chromium layer on the photo resist is observed originating at the edges of some triangles. The point of the stretched pipette is also shown. 88
6.11 The optical microscope setup used for scraping the chromium mask to clean it. (a) An overview of the microscope, with the camera used shown. (b) The hydraulic micropositioner that was utilised. 90
6.12 Part of a cleaned array of chromium triangles on a PMMA protective layer on an InSb substrate. 91
6.13 Photographs of two InSb wafers with PMMA and chromium masks on top. Both show burning from the RIE process. (a) shows the case with the surrounding PMMA and (b) where the surrounding PMMA was first removed. 91
6.14 Optical microscope images of etched InSb pillars. (a) Side on at an angle of $\approx 75^\circ$ and (b) top down. 92
6.15 Spectra of field enhancement in between the particles of particle pairs as the separation distance is decreased. These are shown for (a) spherical particles and (b) triangular particles. 93
6.16 Field plots of the time averaged electric field in a plane cutting through the particles halfway from their base to their top. The spheres have a diameter of 30 µm and the triangles a base to tip length of 30 µm with a thickness of 10 µm. 93
6.17 Three different methods of altering the sharpness of particles, (a) truncation, (b) rounding and (c) changing the internal angle (α). 94
6.18 Rounded and pointed triangles overlaid showing the difference between the two modelled particle shapes. 94
6.19 Transmission response for rounded and pointed triangle arrays, the curved triangles are shown as the solid line and the pointed as the dashed. . . . 95

6.20 Time averaged electric field profiles on a plane cut through the middle of the particle, modelled in an infinite array. The particle thickness is 10 μm, the long axis 61 μm and they are modelled for an array with a pitch of 150 μm. These field plots are for pointed particles as shown, at (a) 0.8 THz, (b) 1.025 THz, and (c) 1.175 THz. 95
6.21 Time averaged electric field profiles on a plane cut through the middle of the particle, modelled in an infinite array. The particle thickness is 10 μm, the long axis 61 μm and they are modelled for an array with a pitch of 150 μm. These field plots are for curved particles as shown, at (a) 0.85 THz, and (b) 1.125 THz. 96
6.22 Optical microscopy images of two arrays of (a) triangles and (b) truncated triangles fabricated using the same photolithography mask. 96
6.23 (a)A schematic of the three triangle types reproduced on the photolithography mask. (b) The transmission through modelled arrays of these three triangles. The sharpest triangles ($\alpha = 15°$) are shown as the solid line, the intermediary particles ($\alpha = 30°$) as the dashed line, and the broad particles ($\alpha = 60°$) as the dotted line. 96
6.24 Calculated transmission through arrays of InSb triangles, the dashed line is the normal response with the solid line showing the effect of an increase in carrier concentration of 1×10^{16} cm^{-3} an increase of 50%. . 97

7.1 (a) Scanning electron microscope image of the array of dimples in aluminium, with diameter = 50 μm, depth = 90 μm, and pitch = 90 μm. The sample array is square with the direction of propagation, shown by the arrow, at 45° to the lattice vectors. (b) The measured (solid curved line) and analytical modelled (dashed line) dispersion of the terahertz hole array sample. (c) 3D schematic of the unit cell used in numerical modelling. 101
7.2 Schematic diagrams showing (a) the open hole array sample configuration, (b) the experimental set up, and (c) the unit cell of the experimental sample, with the propagation direction indicated. 102
7.3 Measured dispersion relations for open and closed metallic hole arrays in the microwave regime, with analytical and finite element method modelling dispersions shown. The field profiles for the symmetric and antisymmetric surface modes are shown on open ended hole arrays, found using the finite element method. 110

7.4 The transmission measured across the surface of an array of open ended square holes defined by $d = 9.25$mm, $a = 6.96$mm, $h = 15$mm, and $\epsilon_h = 2.29$, normalised against the transmission across a flat metal surface. 111

7.5 Surface wave dispersion from the analytical model for open ended hole arrays, (a) where the thickness is varied, and (b) where the surrounding permittivity is asymmetric above and below the sample. 113

7.6 Dispersion relations for an open ended hole array defined by $a = 6.96$mm, $h = 15$mm, and $\epsilon_h = 2.29$ when $d = 15$mm (solid curved line) and $d = 9.25$mm (dashed curved lines). 115

7.7 (a) Spoof surface mode dispersion relations in the reduced zone representation. For hole arrays defined by $\omega_{co} < \omega_{diff}$, a number of modes associated with each grating vector are observable in the 1$^{\text{st}}$ Brillouin zone. For hole arrays with $\omega_{co} > \omega_{diff}$ (b), only the first two (surface plasmon) modes are defined below cut-off. (c) Transmission as a function of hole height h for an array with dimensions $a = 0.8d$. One can clearly observe the multimodal transmission, with several peaks in the frequency region between the cut-off frequency (marked by a solid arrow) and $\omega = \omega_{diff}$. (d) Transmission as a function of hole height h for an array with dimensions $a = 0.4d$, showing the transmission mediated by the symmetric and antisymmetric surface plasmon modes. The lower panels show transmission spectra at heights indicated by dotted arrows. All calculations are for $\epsilon_h = 1$. 119

Definitions

FEM	Finite element method
FIB	Focussed ion beam
$InSb$	Indium antimonide
SEM	Scanning electron microscope
SPP	Surface plasmon polariton
TE	Transverse electric (s-polarised)
$THz-TDS$	Terahertz time domain spectroscopy
TM	Transverse magnetic (p-polarised)

Microwave regime	$1 \rightarrow 200$ GHz
Optical/Visible regime	$300 \rightarrow 1000$ THz
Terahertz regime	$0.2 \rightarrow 2$ THz

Chapter 1

Introduction

> "That wonderful production of the human mind, the undulatory theory of light, with the phenomena for which it strives to account, seems to me, who am only an experimentalist to stand midway between what we may conceive to be the coarser mechanical actions of matter, with their explanatory philosophy, and that other branch which includes, or should include, the physical idea of forces acting at a distance; and admitting for the time the existence of the ether, I have often struggled to perceive how far that medium might account for or mingle in with such actions, generally; and to what extent experimental trials might be devised which, with their results and consequences, might contradict, confirm, enlarge, or modify the idea we form of it, always with the hope that the corrected or instructed idea would approach more and more to the truth of nature, and in the fullness of time coincide with it." (Michael Faraday 1856 [1])

The purpose behind this project was to build upon the understanding of surface plasmons by further investigating them in the terahertz regime. Of particular interest are the properties that allow materials to support surface modes, both surface plasmons and so called spoof surface plasmons and modifying the structure of these materials to create particles for particle plasmon investigations. The advantage of this study over similar optical ones are the reduction of thermodynamic limitations to the sharpness of features relative to the wavelength, the tunability of the permittivity of the materials used, the adaptation of microwave domain spoof surface plasmon structures, and the ability to use a spectrometer that not only measures the intensity but also the relative phase of the electromagnetic radiation detected.

Surface plasmons are responsible for a host of interesting phenomena. They have been utilised to explain effects such as the surface-enhanced Raman effect [2] and

anomalous transmission through subwavelength arrays of holes in metal films [3]. Surface plasmons have also been used for applications such as the detection of individual molecules [4] and surface enhanced fluorescence [5].

The 'terahertz gap' is a region of the electromagnetic spectrum that has been poorly studied. It lies between the far infrared and microwave regimes ($\approx 0.3 \rightarrow \approx 10$ THz). This is due to the difficulty of constructing desktop terahertz sources. Optical methods for creating a continuous spectrum rely mainly on the heating of a material and thus its blackbody radiation. Terahertz radiation is relatively low in energy ($0.0012 \rightarrow 0.041$ eV) which is produced at temperatures around and below room temperature, therefore an attempt at making a lab based generator in this way would not be feasible. On the other side of the 'gap', microwaves are generated by using a wave generator and oscillating electrons in an antenna. The current electronic limitations of this technology means that the oscillating electrons cannot reach a high enough frequency to generate radiation in the range of interest this is due to parasitic capacitance effects. These low and high frequency sources have been in common use for scientific enquiry since the 1800s and 1900s respectively [6, 7]. Whereas the coherent sources needed for terahertz radiation from frequency mixing processes were not avaliable until the invention of the laser in the mid 1960s [8, 9]. Since these early generation methods there has been many others developed, some are quite narrow band, such as modified cascade lasers [10] and free-electron lasers [11]. Broadband sources have also been developed, using ultra short laser pulses to photoexcite charge carriers in biased semiconductor antenna [12] and in a similar technique utilising non-linear crystals [13]. These combined with related detection methods form the basis for terahertz time domain spectroscopy (THz-TDS) which is discussed further in chapter 3. More recently, ultrashort pulses have also been shown to generate terahertz radiation from optical plasmon structures, this is discussed in depth in chapter 4.

Being difficult to generate and detect is not in itself a valid reason for investigating terahertz domain phenomena this frequency range does bring some advantages for applications. Terahertz spectrometry using high-energy optical pulses can employ pump-probe techniques to conduct dynamic, time-resolved alterations and observations of different photonic and plasmonic structures. This coupled with the phase resolved measurements produces a very powerful experimental tool. As well as adding to the underlying physical understanding of the phenomena studied, it is hoped that some of the work presented here can be utilised for real world applications. The recent adoption of small x-ray analysis devices for probing the contents of liquid bottles in airports (Kromek bottle scanner) and t-ray cameras [14] again for security at airports indicates that there is a need for new small scale sensitive chemical detectors. Surface plasmons have been shown to be useful for creating very sensitive detectors [15, 16], and

it is hoped that with the high and characteristic absorption for many chemicals in the terahertz regime that these detectors can be enhanced for applications such as diagnostics on human breath and DNA sequencing [17–19]. The advantages of extending these studies and applications into the terahertz domain are discussed in greater depth in the chapters on terahertz plasmonic materials (chapter 5) and particle plasmons (chapter 6).

Chapter 2

Theory

For over a century there has been both experimental [1, 20, 21], and theoretical [22, 23] investigations into the interaction of metals and electromagnetic radiation. The following is a summary of some of this work with some historic background for context and interest.

2.1 Surface plasmons

The first observation of a surface plasmon polariton (SPP) was by Wood [20] in 1902. He observed two bands, one bright and one dark in the reflection of a white light spectrum from a grating. This anomaly was not explained until 1941 by Fano [22], who realised these were a special case of surface waves previously investigated by Zenneck and Sommerfeld [24, 25]. Fano's description of the modes observed by Wood has proved a very useful and accurate model for a large amount of surface plasmon phenomena. These waves are now well understood and have been thoroughly investigated at optical frequencies and the following discussion will begin by considering these [26].

It is known that a surface plasmon is a quantised longitudinal oscillation in the free electron gas of a metal on a metal dielectric interface where the fields are highly confined to the interface between the metal and dielectric. These surface modes can be coupled to incident transverse oscillating electromagnetic radiation. The resulting surface wave is called a surface plasmon polariton and is a combination of the charge carrier oscillation and the coupled electromagnetic radiation. In this section the dispersion of the coupled surface wave will be derived along with some characteristic length scales for SPPs, with a discussion of how these vary as emphasis moves from the optical regime to terahertz and microwave frequencies. A brief discussion of coupling light to surface plasmons will also follow.

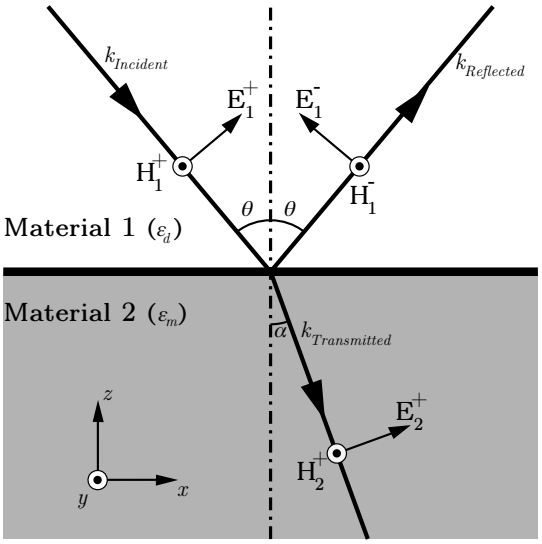

Figure 2.1: An incident p-polarised electromagnetic wave on the interface between two materials of different permittivity (ϵ_d and ϵ_m).

2.1.1 Dispersion relation of surface plasmons

The following is adapted from Raether [26]. Consider an interface between two materials, as shown in fig. 2.1, with an incident transverse magnetic (TM, p-polarised) electromagnetic wave. For simplicity, assume that the materials are semi-infinite and non-magnetic. Take the top material to be a dielectric with a complex permittivity $\epsilon_d = \epsilon_d' + i\epsilon_d''$ and the transmitting lower material to be a metal with a complex permittivity $\epsilon_m = \epsilon_m' + i\epsilon_m''$. Consider the incident electromagnetic wave shown in fig. 2.1, with wavevector, $\vec{k} = (k_x, 0, k_z)$, the fields can then be written as:

$$\vec{E} = [E_x, 0, E_z] \exp(i(k_x x + k_z z - \omega t)), \tag{2.1}$$

$$\vec{H} = [0, H, 0] \exp(i(k_x x + k_z z - \omega t)), \tag{2.2}$$

where, ω is the frequency of incident light. Maxwell's equation, in the absence of free charge can now be applied,

$$\vec{\nabla} \times \vec{H} = \epsilon \frac{\partial \vec{E}}{\partial t} \tag{2.3}$$

to find,

$$H_y = \frac{\epsilon \omega E_x}{k_z} = -\frac{\epsilon \omega E_z}{k_x}. \tag{2.4}$$

Combining this with (2.1) and (2.2) the expressions for the incident ($\vec{E}_1^+$ and $\vec{H}_1^+$), reflected ($\vec{E}_1^-$ and $\vec{H}_1^-$) and transmitted ($\vec{E}_2^+$ and $\vec{H}_2^+$) fields can be found:

$$\vec{E}_1^+ = E_{x1}^+[1, 0, -\frac{k_x}{k_z}] \exp(i(k_x x + k_z z - \omega t)), \tag{2.5a}$$

$$\vec{E}_1^- = E_{x1}^-[1, 0, +\frac{k_x}{k_z}] \exp(i(k_x x - k_z z - \omega t)), \tag{2.5b}$$

$$\vec{E}_2^+ = E_{x2}^+[1, 0, -\frac{k_x}{k_z}] \exp(i(k_x x + k_z z - \omega t)), \tag{2.5c}$$

$$\vec{H}_1^+ = E_{x1}^+[0, +\frac{\omega\epsilon_m}{k_{z1}}, 0] \exp(i(k_x x + k_z z - \omega t)), \tag{2.5d}$$

$$\vec{H}_1^- = E_{x1}^-[0, -\frac{\omega\epsilon_m}{k_{z1}}, 0] \exp(i(k_x x - k_z z - \omega t)), \tag{2.5e}$$

$$\vec{H}_2^+ = E_{x2}^+[0, +\frac{\omega\epsilon_d}{k_{z2}}, 0] \exp(i(k_x x + k_z z - \omega t)). \tag{2.5f}$$

Three conditions can now be applied. As the SPP is non-radiative either the incident or reflected field can arbitrarily be set to zero. The other two are the boundary conditions that the tangential components of the electric and magnetic fields have to be continuous across the interface. Therefore,

$$E_{x1} = E_{x2}, \tag{2.6}$$

and

$$H_{y1} = H_{y2}. \tag{2.7}$$

Assuming that the incident field is zero and combining these, (2.4) yields,

$$H_y = -E_{x1}^- \frac{\epsilon_m \omega}{k_{z1}} = -E_{x2}^+ \frac{\epsilon_d \omega}{k_{z2}}, \tag{2.8}$$

and subsequently combining with the field equations, (2.5), above, provides

$$\frac{\epsilon_m}{k_{z1}} = \frac{\epsilon_d}{k_{z2}}. \tag{2.9}$$

It must also be considered that the surface is translationally invariant, therefore momentum is conserved in the plane of the surface, $k_{x1} = k_{x2} = k_x$. This is also implied by the continuity conditions above, (2.6) and (2.7). It can also be easily shown from $\epsilon_j k_0^2 = k_x^2 + k_{zj}^2$, where j denotes the medium through which the field is propagating,

that

$$k_{zj} = (\epsilon_j k_0^2 - k_x^2)^{1/2}. \tag{2.10}$$

This can then be substituted into (2.9), and thus the SPP dispersion relation is obtained.

$$k_x = \frac{\omega}{c}\sqrt{\frac{\epsilon_m \epsilon_d}{\epsilon_m + \epsilon_d}} = k_{spp}, \tag{2.11}$$

where $k_0 = \omega/c$. This is often simplified in the optical regime by taking ϵ_m and ϵ_d to be purely real, as $|\epsilon'| >> |\epsilon''|$, for ϵ_m. However, this is not a good approximation for the physics discussed below and therefore, it will be left as complex. The dielectric used most commonly in this project is air, ϵ_d is considered to be purely real, as the losses in air can be well approximated to zero.

An example dispersion relation is shown in fig. 2.2, the frequency dependent permittivity used is for silver, found using the Drude model, which is discussed in more depth below [27]. In this figure, the light line, the line a free space electromagnetic wave would follow, is shown as the solid straight line, the surface plasmon frequency (see below) as the broken straight line, and the dispersion relation as the curved solid line. The left pane, 2.2(a), shows a log log plot over a large range of frequencies with three different regimes indicated, whereas the right pane shows only the optical and ultraviolet regime where the surface wave is closely confined to the surface and can be considered to be a plasmon.

From this characteristic dispersion relation it can be seen that as $-\epsilon_m \to \epsilon_d$, ω approaches an asymptotic frequency, defined as the surface plasmon frequency (ω_{sp}). For metals in air ($\epsilon_d = 1$) this condition is met when $\epsilon'_m = -1$. Although as ϵ_m is complex, the imaginary part of the frequency dependent permittivity controls the losses of the SPP. With "good" plasmonic metals having a much lower ϵ''_m than "poor" plasmonic metals, this is discussed in more depth in chapter 5. From fig. 2.2 and (2.11) two things can be easily inferred. As the asymptotic limit is approached the group velocity approaches zero, there is also a momentum gap between that of free space electromagnetic waves and the surface wave; the surface plasmon modes cannot be coupled to by free space electromagnetic radiation.

Fig. 2.2(a) indicates that the plasmon only becomes influential close to the surface plasmon frequency. For metals this frequency falls in the ultraviolet region, showing effects in the optical regime. Far from this frequency, any surface mode is grazing photon like and cannot be described as confined to the surface.

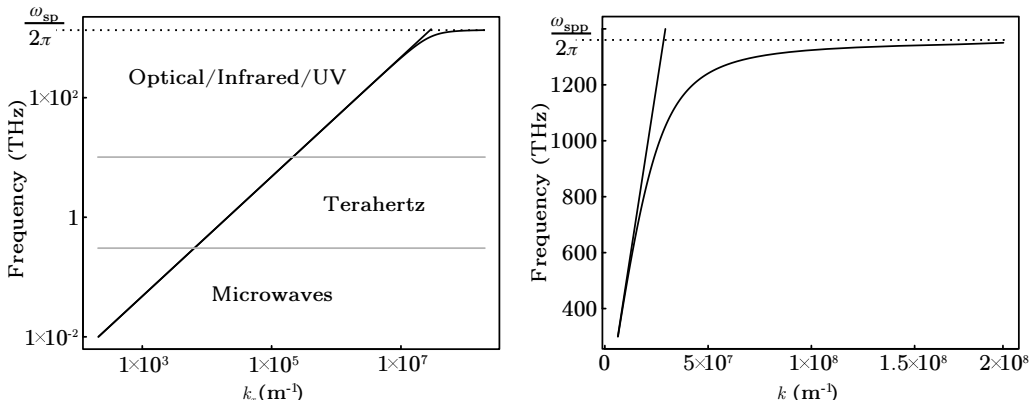

Figure 2.2: The dispersion relation for silver using the permittivity found using the Drude parameters from the literature [27]. (a) The relation on a log log plot from the microwave regime through to the ultraviolet regime, with the terahertz, optical and microwave frequency regimes shown. (b) Only the optical and ultraviolet proportion of the electromagnetic spectrum is shown.

2.1.2 Surface plasmon polariton length scales

The real and imaginary parts of the SPP dispersion relation can be found by substituting the complex forms of ϵ_m and k_x into (2.11). The real and imaginary parts can then be separated and solved simultaneously, resulting in two quadratic equations, for k'_x and k''_x,

$$k'_x = k'_{spp} = k_0 \sqrt{\frac{\epsilon_d(\epsilon_e^2 + \sqrt{\epsilon_e^4 + \epsilon_d^2 \epsilon_m''^2})}{2((\epsilon_d + \epsilon'_m)^2 + \epsilon_m''^2)}}, \tag{2.12a}$$

$$k''_x = k''_{spp} = k_0 \sqrt{\frac{\epsilon_d(\sqrt{\epsilon_e^4 + \epsilon_d^2 \epsilon_m''^2} - \epsilon_e^2)}{2((\epsilon_d + \epsilon'_m)^2 + \epsilon_m''^2)}}, \tag{2.12b}$$

where $\epsilon_e^2 = \epsilon_m'^2 + \epsilon_m''^2 + \epsilon_d \epsilon'_m$. These are useful, as the imaginary part of k_{spp} controls the length over which the propagating SPP decays. The fields fall off with $\exp(k''_{spp} x)$ and the intensity drops off with $\exp(2k''_{spp} x)$. The propagation length (L_{spp}) is defined as the distance after which the intensity decreases by $1/e$, which is minimised at ω_{spp}. Therefore,

$$L_{spp} = \frac{1}{2k''_{spp}} = \frac{1}{2k_0} \sqrt{\frac{2((\epsilon_d + \epsilon'_m)^2 + \epsilon_m''^2)}{\epsilon_d(\sqrt{\epsilon_e^4 + \epsilon_d^2 \epsilon_m''^2} - \epsilon_e^2)}}. \tag{2.13}$$

Similarly in the out of plane (z) direction decaying fields can be observed. Consider

the total momentum equation, $k_0^2 = k_x^2 + k_z^2$, when $k_x > k_0$, i.e. where the plasmon is in existence, k_z is imaginary, which implies the fields decay exponentially in the z direction. This characteristic decay can be quantified by the confinement (penetration depth or skin depth, δ), which is defined as the distance in the z direction at which the fields have dropped to $1/e$ that at the surface, thus

$$\delta_m = \frac{1}{k''_{zm}} = \frac{1}{\sqrt{\epsilon_m k_0^2 - k_x^2}}, \tag{2.14a}$$

for the confinement in the metal and

$$\delta_d = \frac{1}{k''_{zd}} = \frac{1}{\sqrt{\epsilon_d k_0^2 - k_x^2}}, \tag{2.14b}$$

for confinement into the dielectric. The real and imaginary parts of k_z can be solved in a similar way to that described above for k_x. Take $\epsilon_m = \epsilon'_m + i\epsilon_m$, $\epsilon_d = \epsilon'_d$, $k_z = k'_z + ik''_z$ and k_x given by equations (2.12) and substitute together before the equations are split into the real and imaginary parts and solved simultaneously yielding

$$k''_{mz} = k_0 \sqrt{\frac{\epsilon'_m - \frac{\epsilon_d \epsilon_e^2}{(\epsilon_d+\epsilon'_m)^2+\epsilon''^2_m} - \sqrt{\left(\epsilon'_m - \frac{\epsilon_d \epsilon_e^2}{(\epsilon_d+\epsilon'_m)^2+\epsilon''^2_m}\right)^2 + \left(\epsilon''_m - \frac{\epsilon_d^2 \epsilon''_m}{(\epsilon_d+\epsilon'_m)^2+\epsilon''^2_m}\right)^2}}{-2}}, \tag{2.15a}$$

for the metal and

$$k''_{dz} = k_0 \sqrt{\frac{\epsilon'_d - \frac{\epsilon_d \epsilon_e^2}{(\epsilon_d+\epsilon'_m)^2+\epsilon''^2_m} - \sqrt{\left(\epsilon'_d - \frac{\epsilon_d \epsilon_e^2}{(\epsilon_d+\epsilon'_m)^2+\epsilon''^2_m}\right)^2 + \left(\epsilon''_d - \frac{\epsilon_d^2 \epsilon''_m}{(\epsilon_d+\epsilon'_m)^2+\epsilon''^2_m}\right)^2}}{-2}}, \tag{2.15b}$$

for the dielectric. From (2.14) it can now be said that:

$$\delta_m = \frac{c}{\omega} \sqrt{\frac{-2}{\epsilon'_m - \frac{\epsilon_d \epsilon_e^2}{(\epsilon_d+\epsilon'_m)^2+\epsilon''^2_m} - \sqrt{\left(\epsilon'_m - \frac{\epsilon_d \epsilon_e^2}{(\epsilon_d+\epsilon'_m)^2+\epsilon''^2_m}\right)^2 + \left(\epsilon''_m - \frac{\epsilon_d^2 \epsilon''_m}{(\epsilon_d+\epsilon'_m)^2+\epsilon''^2_m}\right)^2}}}, \tag{2.16a}$$

for the metal and

$$\delta_d = \frac{c}{\omega} \sqrt{\frac{-2}{\epsilon'_d - \frac{\epsilon_d \epsilon_e^2}{(\epsilon_d+\epsilon'_m)^2+\epsilon''^2_m} - \sqrt{\left(\epsilon'_d - \frac{\epsilon_d \epsilon_e^2}{(\epsilon_d+\epsilon'_m)^2+\epsilon''^2_m}\right)^2 + \left(\epsilon''_d - \frac{\epsilon_d^2 \epsilon''_m}{(\epsilon_d+\epsilon'_m)^2+\epsilon''^2_m}\right)^2}}}, \tag{2.16b}$$

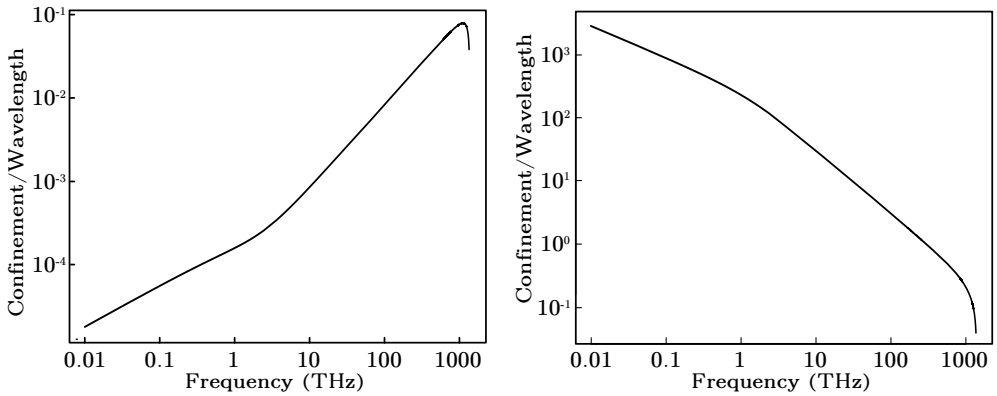

Figure 2.3: The field confinement in the z direction (normal to the surface) using the Drude parameters of Silver, (a) into the metal, and (b) into the dielectric.

for the dielectric. These can be simplified where $\epsilon'_m >> \epsilon''_m$ [27] to:

$$\delta_m = \frac{c}{\omega}\left|\frac{\epsilon'_m + \epsilon_d}{\epsilon'^2_m}\right|^{\frac{1}{2}} \tag{2.17a}$$

$$\delta_d = \frac{c}{\omega}\left|\frac{\epsilon'_m + \epsilon_d}{\epsilon^2_d}\right|^{\frac{1}{2}} \tag{2.17b}$$

It is interesting to note that the confinement can be found from the dispersion plot. In fig. 2.2(b) the confinement is stronger (more confined) as the dispersion curves further away from the lightline. Therefore the confinement is strongest at the surface plasmon frequency, as might be expected. Fig. 2.3 shows the frequency dependent confinement both into the metal and into the dielectric, again this has been shown for a wide range of frequencies, using the Drude model, with the parameters for silver being used [27]. Here the significant drop in the confinement (becoming more confined to the surface) around the surface plasmon frequency is apparent. The fields are not confined far from the SPP frequency, again it can be said that a plasmon is not in existence, merely a grazing photon like wave.

Enough information is given above to be able to draw some conclusions about the fields of SPPs and to create a basic schematic of these fields, as shown in fig. 2.4. It has been shown that the fields penetrate more into the dielectric than into the metal, are highly confined, are not propagating in the z direction and have zero group velocity at the surface plasmon frequency (the dispersion asymptotes).

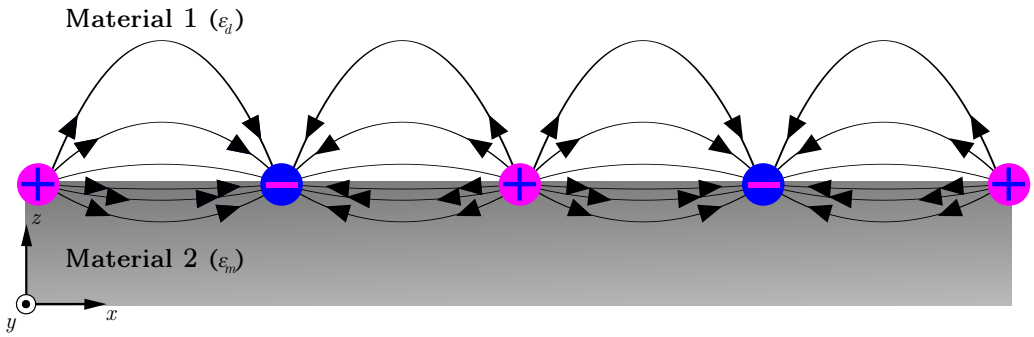

Figure 2.4: A schematic of the electric fields on the metal-dielectric interface for a surface plasmon polariton, the decay into the metal and dielectric are shown. For any moment in time the field must change direction along the surface as the surface charge wave is longitudinal.

2.1.3 Surface plasmon coupling methods

As mentioned above, there is a momentum mismatch between the in plane SPP surface wave and any free space electromagnetic wave with the correct frequency. This is shown by the dispersion relation (fig. 2.2) where the SPP mode curves away from, and importantly underneath the lightline. To compensate for this and to allow the coupling of light to the surface mode, different coupling methods have been invoked, a brief description of some of these methods follows.

In grating coupling, a metallic grating is fabricated on the interface, incident light is scattered in the grating vector direction, providing a modification to the in plane momentum of the light, $k_{scattered} = k_0 + k_g$, where k_g is the grating wavevector [28]. Optimum coupling occurs when $k_{scattered,x} = k_{spp}$, and is manifest by a dip in the reflection off of the grating (for first order modes). The first observation by Wood [20] used this method, and modifications on it have since been widely used. It is also possible to couple to SPP modes in the same way using a rough surface, although the efficiency of this is greatly reduced, and the propagation length of the SPP is also reduced [26, 28, 29]. This method is widely used in surface enhanced Ramen spectroscopy [30, 31].

Another widely used coupling method is the use of a glass prism. When total internal reflection occurs between two dielectrics there is an evanescently decaying field formed from the reflecting interface into what would be the transmitting material [32]. Placing a metal film into this field, with either a small air gap (Otto configuration [33]) or directly onto the glass (Kretschmann configuration [34]) allows for coupling to the surface plasmon. As there is no wavevector normal to the interface, all the momentum must be in the in plane direction. With this method, the SPP again manifests itself

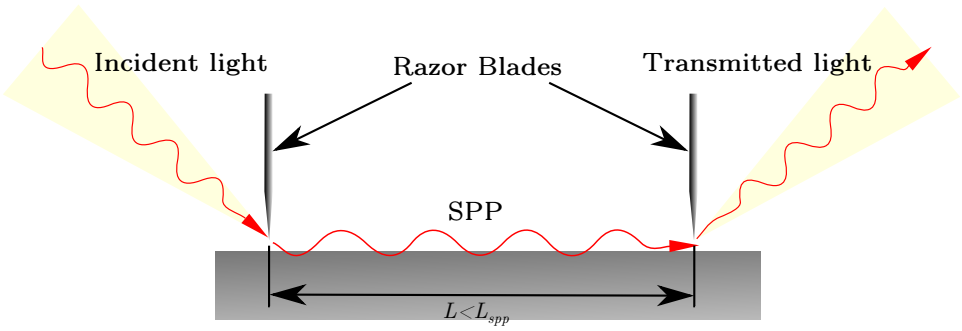

Figure 2.5: Schematic diagram of the blade coupling method, a form of scattering coupling.

as a dip in reflectance at a given frequency (for fixed angle measurements) or angle (for fixed frequency measurements). These methods are very sensitive to the dielectric constant close to the surface and are therefore often useful for observing changes in the local permittivity [16, 35].

The final coupling method discussed here and employed below is that of coupling with scattering centres, these can be formed from edges, or apertures. Blades are often used close to the surface ($\approx 1\lambda$) to form both an edge and an aperture onto which the incident light is directed. The light is scattered at the scattering centre, which will have some components with $k_{scattered} = k_{spp}$, allowing it to couple to the surface mode. This scattering can be explained by considering each point on the scatterer as having an excited dipole, the orientation of which is random, and therefore the subsequent radiation emission is random. After some distance ($< L_{spp}$) another scattering centre is placed close to the surface, as shown in fig. 2.5, here the surface wave scatters and decouples back into free space radiation. This method has the advantage that the measured radiation must have been coupled to the surface before it could enter the detector, although it is not suitable for high frequency measurements as the wavelength is too short to easily position scattering centres. Terahertz spectroscopy has previously been employed using blade coupling for phase sensitive measurements of surface plasmons polaritons [36].

2.2 Drude model

A materials permittivity depends upon the dynamics of the charge carriers it contains. For metals this is dominated by the conduction band electrons, which can be modelled as a gas of free electrons using the Drude model [37]. In this semiclassical model, the free electrons are not considered to scatter from each other but only from the lattice. These conduction band electrons are modified from free space electrons by the introduction

of an effective mass (m^*). This is otherwise a classical gas of charge carriers at some temperature (T), with a velocity distribution that has a root mean squared velocity of $v_{rms} = \sqrt{\frac{3k_BT}{m^*}}$, where k_B is the Boltzmann constant. The elastic lattice collisions do not vary this average velocity and the resulting direction of the electrons is random, this results in a random walk of electrons (solid line in fig. 2.6), with a mean free path of l_w and average rate of collisions of γ.

Applying an external electric field ($\vec{E}$) modifies the electron random walk by there being preferential accelerations between collisions such that there is a drift velocity (v_d) in the opposite direction to that of the electric field. In most conditions $v_d << v_{rms}$. For a physically real scattering length a quantum mechanical model must be considered. The electron is considered to be a wave travelling on a perfect lattice scattering from imperfections in that lattice. This yields a much longer scattering length than the classical model. Classically, an electron would scatter off of the lattice which results in scattering lengths of order the lattice constant [37]. This quantum mechanical modification is also the origin of the effective mass. An electron wave in a crystal will undergo multiple reflections from the lattice positions, similar to that of light in a multilayer dielectric stack. As the electron wavelength approaches the lattice spacing a standing wave is formed, this obviously changes the ease at which an electron can move through a crystal. The effective mass can be found by considering the band structure of a crystal by

$$\frac{1}{m^*} = \frac{1}{\hbar}\frac{d^2E}{dk^2}, \tag{2.18}$$

where k is the wavevector measured from the Brillouin zone boundary, and E is the energy of the band [38]. It can therefore be said that the greater the curvature of the bands the smaller the effective mass. The collisions from the lattice lead to a damping of the acceleration due to the applied electric field. If the electric field is considered to be time varying ($\vec{E}(t)$), the equation of motion for the electrons is a first order differential equation:

$$\frac{\partial}{\partial t}v_d(t) + \gamma v_d(t) = \frac{q}{m^*}\vec{E}(t), \tag{2.19}$$

where q is the charge of the carrier. If the applied field is sinusoidal, $\vec{E}(t) = E_0e^{-i\omega t}$, the differential equation is linear and can be solved using an integrating factor to yield

$$v_d = \frac{q}{m^*}\frac{1}{(\gamma - i\omega)}E_0. \tag{2.20}$$

From this it can be seen that there is simply a proportionality factor between v_d and

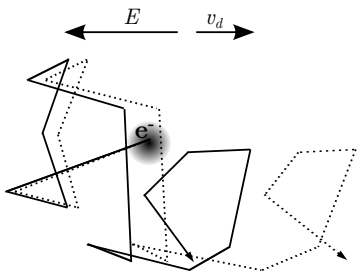

Figure 2.6: The path traced by an electron in a metal according to the Drude model. The electron undergoes many random scattering events resulting in a random walk. The solid line indicates the situation where there is no applied electric field and the dotted line the case when there is an applied electric field resulting in a drift velocity v_d.

$\vec{E}$, which is defined as the mobility

$$\mu = \frac{q}{m^*}\frac{1}{(\gamma - i\omega)}. \tag{2.21}$$

As the scattering rate increases, the time between collisions decreases and the mobility decreases, it is therefore a measure of the ease for an electron to move through the crystal. The macroscopic conduction of a metal depends not only on the mobility but also upon the carrier concentration (N), and can be defined as:

$$\sigma(\omega) = Ne\mu(\omega), \tag{2.22a}$$

where e is the charge of an electron and $q = e$,

$$\sigma(\omega) = \frac{\epsilon_0\omega_p^2}{\gamma - i\omega}, \tag{2.22b}$$

where ω_p is the plasma frequency

$$\omega_p^2 = \frac{Ne^2}{\epsilon_0 m^*}. \tag{2.23}$$

It is also known that the frequency dependent relative permittivity is related to $\sigma(\omega)$ by

$$\epsilon(\omega) = \epsilon_l + \frac{i\sigma(\omega)}{\omega\epsilon_0} \tag{2.24}$$

thus

$$\epsilon_m(\omega) = \epsilon_l - \frac{\omega_p^2}{\omega^2 + i\omega\gamma}, \tag{2.25}$$

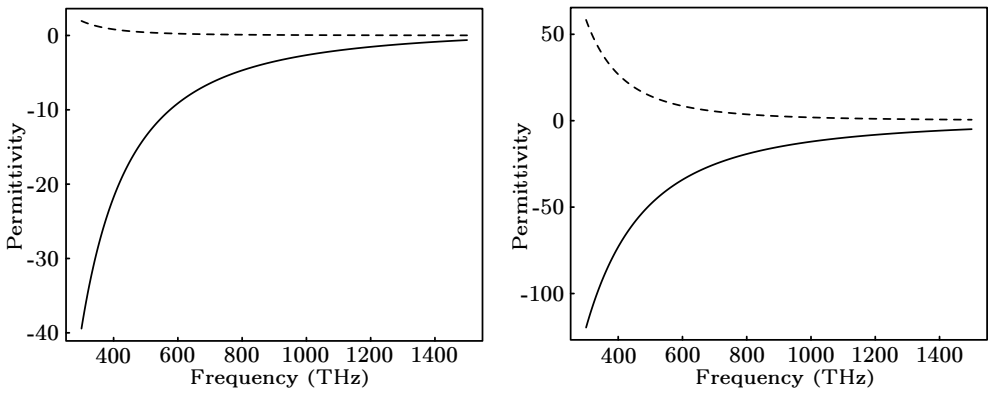

Figure 2.7: Example complex permittivity for metals in the optical regime, the solid lines represent the real part, and the dashed lines the imaginary part, for (a) silver and (b) aluminium, found using the Drude model.

where ϵ_l is the response of the ionic lattice, which is frequency independent (for metals at optical frequencies $\epsilon_l = 1$). The parameters required in the Drude permittivity equation can be found experimentally [39] or calculated from the properties of the electron gas of the metal.

It has been shown that despite the simplicity of this model it works well for some metals in the optical regime [37]. Fig. 2.7 shows the real (solid lines) and imaginary (dashed lines) Drude permittivity for silver (fig. 2.7(a)) and aluminium (fig. 2.7(b)). The requirement above that at ω_{spp}, $\epsilon'_m = -1$ where the dielectric is air, can be achieved by both of these materials in the ultraviolet. If (2.25) is set to full fill this requirement then it can be easily shown that

$$\omega_{sp} = \sqrt{\frac{\omega_p^2}{1+\epsilon_l} - \gamma^2}, \tag{2.26}$$

thus the surface plasmon frequency is easily found.

2.3 Localised surface plasmons resonances

Localised surface plasmon resonances are probably the earliest observed plasmonic effect, being used in glass to create tints and vivid colours for centuries if not millennia, although this phenomenon was not understood until the 20$^{\text{th}}$ century. In 1857 Faraday [1] conducted a detailed qualitative study on the effects that could be observed when treating metals in a certain way. He came to the conclusion that the different observed colours must be due to small particles of the metal. This was with no knowledge of

electrons or much other physics that is taken for granted today. The first quantitative explanation for these effects was put forward by Mie [40]. In his analysis, spherical particles are considered to be perfect scatterers, for which Maxwell's equations are solved, resulting in extinction spectra, where extinction = scattering + absorption. The different colours result from different extinction resonances in the optical regime. More recently, the resonance in extinction has been explained to be due to the resonant behaviour of free conduction band electrons in the metal [41], which can be interpreted as highly localised SPPs [26].

2.3.1 Quasi-static approximation

The following is a brief discussion of the origins of these resonances in the quasi-static approximation. Here it is required that the particles are much smaller than the wavelength of light incident upon them, thus for any moment in time the phase difference across the particle is negligible.

For simplicity, consider a non-magnetic (permeability $(\mu) = \mu_0$), metallic (permittivity, ϵ_m) sphere (radius, a) in a continuous non-absorbing dielectric (with permittivity ϵ_d). Applying a uniform electric field to the sphere results in it becoming polarised along the direction of the applied field. There is therefore a polarisation field, which will modify the field outside of the particle.

To determine the fields inside ($\vec{E}_1$) and outside ($\vec{E}_2$) the particle, normal electrostatics can be applied. Starting with the scalar potentials

$$\vec{E}_1 = -\vec{\nabla}\varphi_1, \tag{2.27a}$$

$$\vec{E}_2 = -\vec{\nabla}\varphi_2, \tag{2.27b}$$

the Laplace equation

$$\nabla^2\varphi = 0 \tag{2.28}$$

and the boundary conditions at the radius of the sphere ($r = a$), that the field potential is continuous

$$\varphi_1 = \varphi_2 \tag{2.29}$$

and

$$\epsilon_m \frac{\partial\varphi_1}{\partial r} = \epsilon_d \frac{\partial\varphi_2}{\partial r}. \tag{2.30}$$

One more condition must also be taken into account, that of the effect of the particle on the field a great distance away, this should be small so that the external field tends

to the incident field ($\vec{E_0} = E_0\vec{z}$) as $r \to \infty$, thus

$$\vec{E_2} = \vec{E_0} \qquad \lim r \to \infty \tag{2.31a}$$

$$\varphi_2 = -E_0\vec{z} = -E_0 r\cos\theta \tag{2.31b}$$

The Laplace equation can now be solved using Legendre polynomials, and applying the boundary conditions yields

$$\varphi_1 = -\frac{3\epsilon_d}{\epsilon_m + 2\epsilon_d}E_0 r\cos\theta, \tag{2.32a}$$

$$\varphi_2 = -E_0 r\cos\theta + a^3 E_0 \frac{\epsilon_m - \epsilon_d}{\epsilon_m + 2\epsilon_d}\frac{\cos\theta}{r^2} \tag{2.32b}$$

from which it can be seen that the field outside the particle, described by φ_2, is a superposition of the incident field and the field due to the particle, as expected. Taking the standard equation for the scalar field around an ideal dipole;

$$\varphi = \frac{\vec{p}\cdot\vec{r}}{r\pi\epsilon_d r^3} = \frac{p}{4\pi\epsilon_d}\frac{\cos\theta}{r^2} \tag{2.33}$$

it can be seen that in this special case, the dipole moment ($\vec{p}$) is

$$\vec{p} = 4\pi a^3 \frac{\epsilon_m - \epsilon_d}{\epsilon_m + 2\epsilon_d}\epsilon_d\vec{E_0} \tag{2.34}$$

where α, the polarisability is

$$\alpha = 4\pi a^3 \frac{\epsilon_m - \epsilon_d}{\epsilon_m + 2\epsilon_d}, \tag{2.35}$$

which is well known as the Clausius-Mossotti equation [42, 43]. Thus it can be seen that there is a resonance in the polarisability when $\epsilon_m = -2\epsilon_d$. Substituting this requirement into (2.25) yields

$$\omega_{LSPR} = \sqrt{\frac{\omega_p^2}{2\epsilon_d + \epsilon_l} - \gamma^2}, \tag{2.36}$$

which is strongly reminiscent of (2.26). And for a low loss metal in air simplifies to.

$$\omega_{LSPR} = \sqrt{\frac{\omega_p^2}{3}}. \tag{2.37}$$

These resonances manifest in very strong field enhancements around the particle. It has been shown that if the particle shape is modified from spheres the resonance position changes along with the distribution of enhanced fields [44–47]. This is as expected due to the dependence of the polarisability with shape [48]. It is a rough approximation that the maximum enhancement changes with the curvature [49]. Other investigated results have been that generally smaller particles have higher frequency resonances [45]. It should also be noted that when fabricated in arrays the fields due to the particles may interact with one another, disorder in these arrays can also cause unusual effects [50, 51].

In the last few decades there has been a significant increase in the understanding and application of particle plasmons that has come from new nano-scale fabrication techniques. From fabricating individual particles using electron beam lithography (EBL) [52] and probing them with dark field microscopy to very large scale regular arrays using nano-sphere lithography (NSL) [53]. This has lead to several varied applications including, surface enhanced Raman spectroscopy (SERS) [2], the detection of individual molecules [4] and surface enhanced fluorescence [5].

Chapter 3

Methods

This chapter comprises descriptions of the experimental techniques employed throughout this project. The physics behind some of the methods is discussed, with techniques and 'tricks' which have been used also included, as well as some discussions comparing these to other methods.

3.1 THz Spectroscopy

As discussed briefly earlier, benchtop sources of terahertz radiation have only recently been developed [13, 54, 55]. Previously sources were either very large (e.g. synchrotron [56]) or narrow band (e.g. free electron lasers [57] and backward wave oscillators [58]). Whereas the terahertz domain probing method utilised here is broadband with a working frequency domain range of $0.2 \rightarrow 2$ THz and fits on a bench top. It also has the advantage of measuring the full electric field profile on the detector. This therefore allows for phase sensitive measurements that should allow for in depth probing of physical phenomena, e.g. the direct measurement of the dispersion of surface plasmons using the blade coupling method discussed in chapter 2 [36].

Two subtly different spectrometers have been used in this project, a focussing spectrometer shown in fig. 3.1 and a collimated spectrometer shown in fig. 3.2. Note that in these schematics some optics have been removed from the real-world system for simplicity. Here the ray path through the focussing spectrometer will be described, as well as an example of a measurement, before the differences to the collimated kit are discussed. This is followed by a more in depth analysis of the generation and detection of terahertz radiation and the balanced diodes built for the optical light detection.

This kind of room temperature bench top terahertz experiment has only been made feasible with the advent of affordable Ti:Saphire amplified laser systems [59]. The system used here is a Coherent Legend, which uses a Coherent Evolution Elite laser

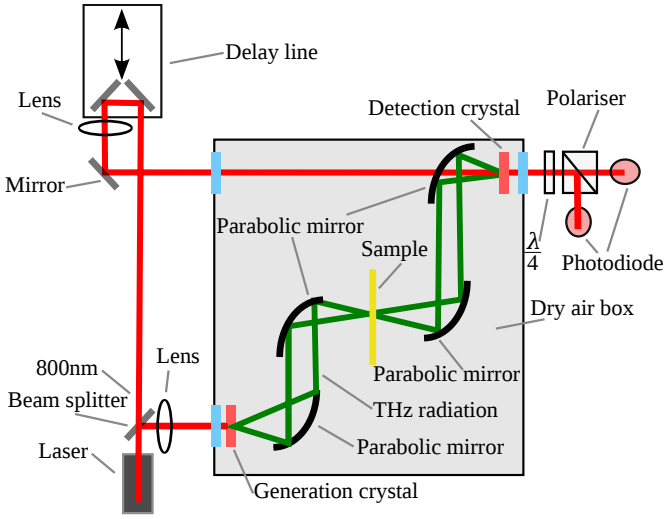

Figure 3.1: Schematic of the focusing terahertz time domain spectrometer (THz-TDS) used in this project, the optical 800nm path is shown in red with the terahertz beam path shown in green.

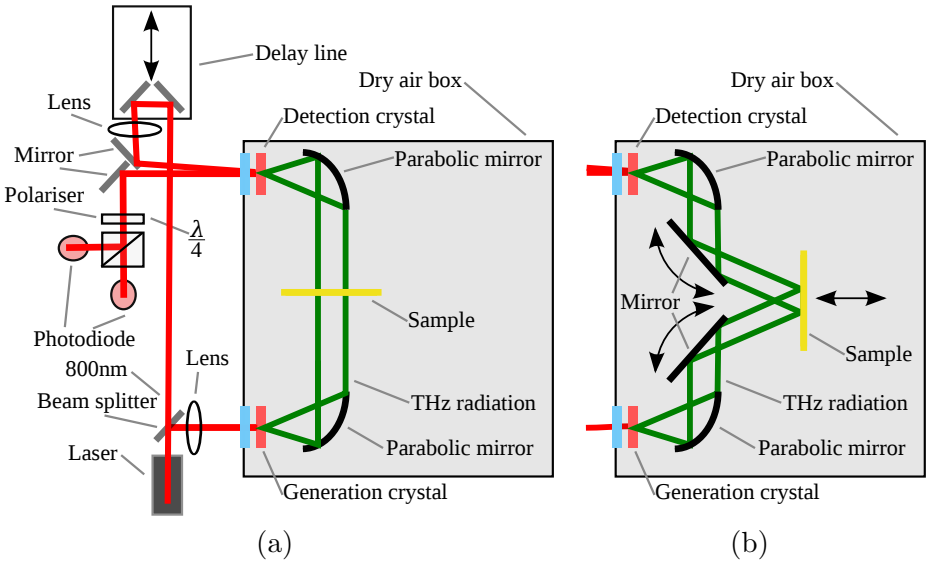

Figure 3.2: (a) Schematic of the collimated terahertz time domain spectrometer (THz-TDS) in the transmission configuration used in this project, the optical 800nm path is shown in red with the terahertz beam path shown in green. (b) Schematic of the dry air box section of the collimated THz-TDS in the reflection configuration.

as an optical pump, and a Coherent Vitese as a seed laser. Producing high energy ($\approx$ 3mJ), very short ($\approx$ 100fs), pulses of light with a central wavelength of 800nm, and a bandwidth of 11nm. Briefly, the Vitesse system is a laser diode pumped pulsed laser system, outputting 12nJ pulses that are 85fs in length, at a repetition rate of 80MHz. These 800nm pulses enter the Legend system and are stretched in time before being passed through a cooled titanium doped sapphire crystal, the temporal stretching is to avoid damage to the gain crystal. Coincident on this crystal is the green pump laser (532nm) from the Evolution system, creating a population inversion and thus allowing for stimulated emission of radiation, amplifying the seed pulse energy [59]. The cavity within the Legend is bounded by Pockel's cells, controlling the number of passes for each pulse. The pulses pass through the cavity around 20 times before being emitted. After emission the pulses are passed through a compressor resulting in the high energy ultrafast laser pulses required. The importance of these ultra fast laser pulses will become apparent below. The repetition rate of the pulses is reduced to 1050 Hz.

Considering fig. 3.1, the ultra fast laser pulse is first split along two paths, the generation path and the detection path. The generation path is first chopped by a mechanical-optical chopper with a frequency of 525Hz, half that of the repetition rate of the laser system. The chopper is phase matched to the laser frequency so that every other full pulse is allowed through. The frequency from the chopper is linked to a lock-in-amplifier for sampling the measured signal. The laser path is focused through a glass window into the the dry air box and onto a ZnTe crystal. Care must be taken to ensure that there is no generation of light from the glass window. On the ZnTe crystal the optical pulse has a spot size of a few millimetres. The energy density of this spot can be changed by moving the focus or the introduction of neutral density filters. The energy density is modified such that the ZnTe crystal is close to, but below, the point at which it burns. The box, indicated by the shaded region in figs. 3.1 and 3.2, is partially sealed and connected to an air flow that has passed through 22kg of Drierite Du-Cal desiccant using a compressed air drier 106-C from Drierite [60] creating a low humidity environment inside. This is required as even a small trace of water in the terahertz beam path will absorb a large amount of the radiation due to the rotational modes of the water molecules, which would be clearly visible in the measured spectra [61].

In the ZnTe crystal optical rectification occurs (a non-linear, frequency difference mixing process), that results in a pulse of terahertz radiation being emitted in a cone centred around the optical axis of the 800nm path [13]. This pulse is a few picoseconds in length, with frequency components in the terahertz domain. A polystyrene filter is included at this point which stops any residual 800nm radiation without affecting the terahertz greatly [62]. Removing this filter allows for the alignment of the rest of

the terahertz beam path, as both pulses follow very similar routes. Therefore when discussing alignment along the terahertz beam path, the 800nm light is always being used to check the alignment.

The cone of radiation is collimated with the use of a parabolic mirror, with a focal length of 15cm, before being focused onto the sample site by a second parabolic mirror, an equal distance away from the focus is a third parabolic which again collimates the radiation. These last two parabolic mirrors can be tilted to an angle of $\approx 30^{\circ}$ allowing for reflection, and blade coupled experiments [36]. It is very important to ensure that as a piece of paper passes through the focus the beam shape does not change, this ensures the orientation and position of the parabolic mirrors are correct. A forth (and final) parabolic is used to focus the radiation onto a second ZnTe crystal used as part of the detection optics, this mirror has a hole drilled through the optical axis. Again, the shape of the beam should not change as it passes through the focus. Thus ends the generation path.

The detection path must be the same length as the generation path, the reason for this will become apparent. The detection path is incident upon a retroreflector on an electro-mechanical delay line. From here the pulse in time relative to the generation pulse can be altered. The path passes through the back of the last parabolic mirror and is incident on the ZnTe detection crystal. There are now two pulses incident on the crystal, these should be spacially and temporally overlapped. The terahertz pulse changes slowly compared to the optical pulse which can be scanned in time over the entire range of the terahertz pulse. Inside this second crystal (the detection crystal) an electro-optical effect can occur, where the polarisation state of a transmitted optical pulse is modified by the application of an external electric field through the Pokels effect [63–66]. Over the very short period of the 800nm pulse the terahertz pulse appears to be a DC electric field. This allows for the electric field profile of the terahertz pulse to be sampled as a function of time.

High terahertz fields induce an eliptical polarisating in the 800nm pulse. A quarter waveplate is used to convert this elliptical light into linearly polarised light. The difference in the two polarisations is measured by using a beam splitting polariser and a pair of balanced photo diodes. The difference in the signal is sent to the lock-in amplifier. This measured difference in the intensity of the polarisation states is directly related to the terahertz electric field strength (see below). Thus the terahertz field can be plotted against time, an example of this is shown in fig. 3.3(a) [13, 64]. It is assumed that the background field is zero, so a 'baseline' subtraction can be made, using the flat region as a reference. A Fourier Transform can then be preformed on the time domain trace to yield a frequency domain spectrum of the complex electric field, and therefore its associated phase. Typical results can be seen in fig. 3.3(b). The precise shape of these

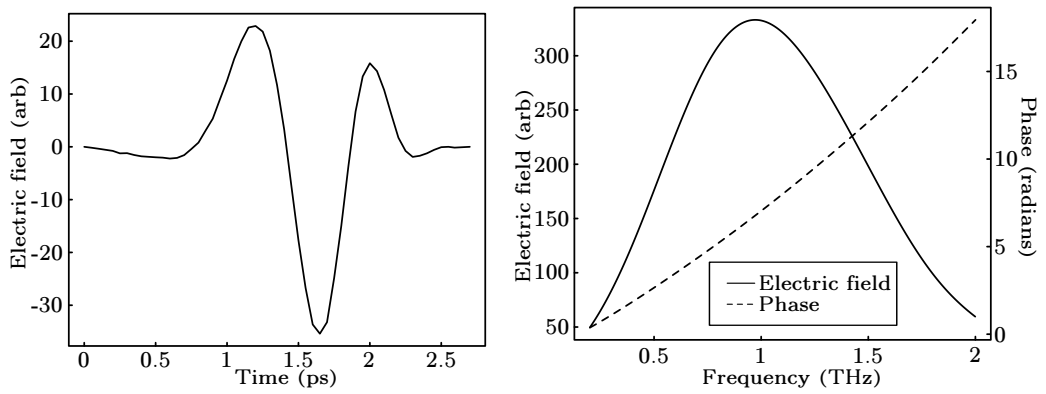

Figure 3.3: Example traces from a THz-TDS setup, (a) shows the time domain trace, whereas (b) shows the modulus of the complex frequency domain trace, also shown is the phase measured through the system.

time and frequency domain traces depends highly on the alignment of the system. For example it can be seen that if the spacial overlap between the terahertz and 800nm beams on the detection crystal is poor there is a distinct shoulder in the time domain pulse around 2.25ps in fig. 3.3(a).

The collimated THz-TDS has some small differences to the focussing kit. It only has two parabolic mirrors, focal length 5cm, as there is no focusing on the sample required. The shorter focal length, results in a narrower beam of terahertz radiation [32]. The parabolic mirrors are not rotated for reflection experiments. Extra mirrors need to be included to move the beam onto a different sample location, which can be moved backwards and forwards changing the angle of incidence, as shown in fig. 3.2(b). The other important difference is the detection path does not travel through a parabolic and through the crystal, but is reflected off of the reverse side of the crystal to the incident terahertz radiation. There is a very large change in maximum terahertz signal observed as the beam moves further from normal incidence [61].

3.1.1 Generation and detection

For the purposes of this project, phase sensitive spectroscopy is considered important and therefore time resolved pulsed terahertz generation is of interest. However it should be briefly noted that there are continuous wave generation methods such as photomixing and difference frequency mixing using two pump beams [61]. Below, the two most common pulsed broadband generation methods are discussed followed by their related detection configurations [67–72].

Photoconductive antennas are semiconductor devices onto which a pair of electrodes

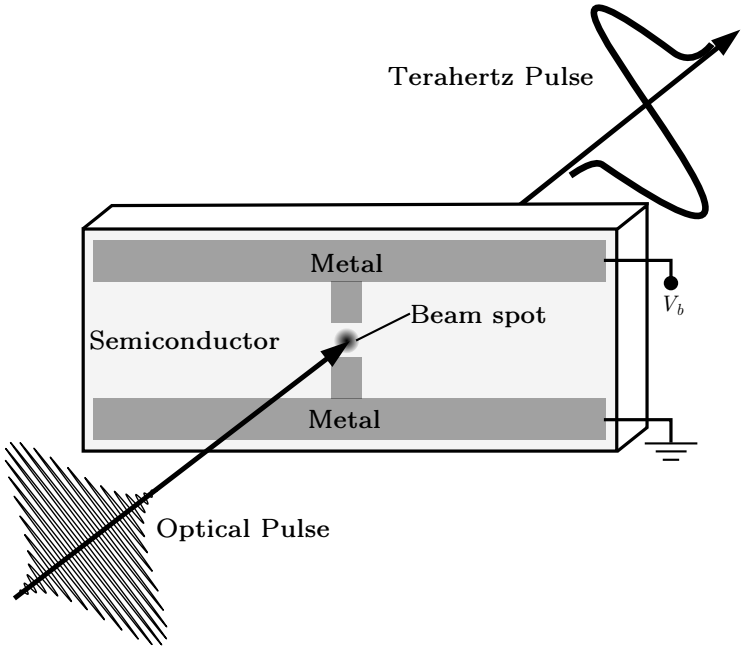

Figure 3.4: An example photoconductive device, a bias voltage is applied across the antenna gap, when the incident optical pulse excites charge carriers their resultant acceleration results in an emitted pulse of terahertz radiation.

are fabricated typicallly betwween 5 and 80 µm apart, similar to that shown in fig. 3.4 [55, 73]. A large bias voltage is applied between the electrodes (V_b), it is therefore desirable to have a large breakdown field [74]. If the bandgap of the semiconductor is lower than the photon energy (1.55eV at 800nm) of an incident pulse, the device will act as a photoconductive switch with a rise-time of the carrier population that is a function of the pulse length, and a switch-off time which is mostly determined by the carrier lifetime [55] although screening is important for narrow band gap semiconductors and at high intensities. The induced photocurrent is accelerated by the DC field, and a pulse is therefore radiated with a temporal length determined by the photoconductive switch characteristics. If the pulse length (rise-time) is ultra fast ($\approx$ 100fs) and the carrier lifetime is sub picosecond, the resultant single oscillation of emitted radiation contains Fourier components in the terahertz frequency band. The mathematics of this are covered in Lee [61], where the system is considered to be a Hertzian dipole with the Drude model being used for the carrier dynamics.

The other common broadband terahertz pulse generation, and the one utilised in this project is optical rectification, a non-linear, frequency difference mixing method [75–77]. The electrons inside a dielectric can often be accurately described by the Lorentz model, where they are considered to be simple harmonic oscillators which can

be driven by an applied external field [78]. Fig. 3.5(a), reproduced from Lee [61], shows the lattice positions in a common electro optical (EO) crystal (ZnTe). From this it can be inferred that the binding electrons between the Ze and Te atoms will experience a different potential depending on their oscillations towards either atom type. This can be modelled by considering a Taylor series of the potential energy with the form

$$U(x) = \frac{1}{2}m\omega_0 x^2 + \frac{1}{3}m\alpha x^3 \tag{3.1}$$

illustrated in fig. 3.5(b), where the cubic term represents the asymmetry of the chemical bond. From this it can be seen that the potential results in a non-linear oscillation when electrons are oscillated along this axis. To take this discrepancy in the potential into account a modified equation of motion needs to be used in the Lorentz model. This has the form

$$\frac{d^2x}{dt^2} + \gamma\frac{dx}{dt} + \omega_0^2 x + \alpha x^2 = -\frac{e}{m}E(t), \tag{3.2}$$

where the non-linear term αx^2 is much smaller than the linear term $\omega_0^2 x$ and $E(t) = E_0 e^{-i\omega t}$, a continuous wave optical beam. Using perturbation theory, which is valid as $\alpha x^2 << \omega_0^2 x$, the non-linear polarisability can be found

$$P_0^{(2)} = 2\epsilon_0\chi^{(2)}(0, \omega, -\omega)|E_0|^2 \tag{3.3}$$

where $\chi^{(2)}(0, \omega, -\omega)$ is the second order optical susceptibility, which relates to the optical rectification [61, 75, 77]. If the pulse duration is much longer than the optical period, (3.3) can be used to find the non-linear polarisation for an applied optical pulse. This process is illustrated by fig. 3.5(c). This induced polarisation has a single pulse length which is defined by the optical pulse length, therefore the resultant generated radiation has a spectral bandwidth that is related to the inverse of the optical pulse length. Therefore $\approx$ 100fs laser pulses should result in terahertz radiation generation.

It is clear from fig. 3.5(a) that the orientation of the non-linear crystal relative to the incident E field is very important. This needs to be analysed by considering the full susceptibility tensor, where

$$P_i^{(2)}(0) = \sum_{j,k} \epsilon_0\chi_{i,j,k}^{(2)}(0, \omega, -\omega)E_j(\omega)E_k^*(\omega) \tag{3.4}$$

where i, j and k are indices relating to the Cartesian components of the field and $\chi_{i,j,k}^{(2)}$ is the tensor element of the second order non-linear susceptibility for that field [61, 75, 77]. From this a contracted (3 by 6) matrix for the polarisability can be formed, with elements d_{il}, but for ZnTe, which has a crystal class of $\bar{4}3m$, only 3 terms

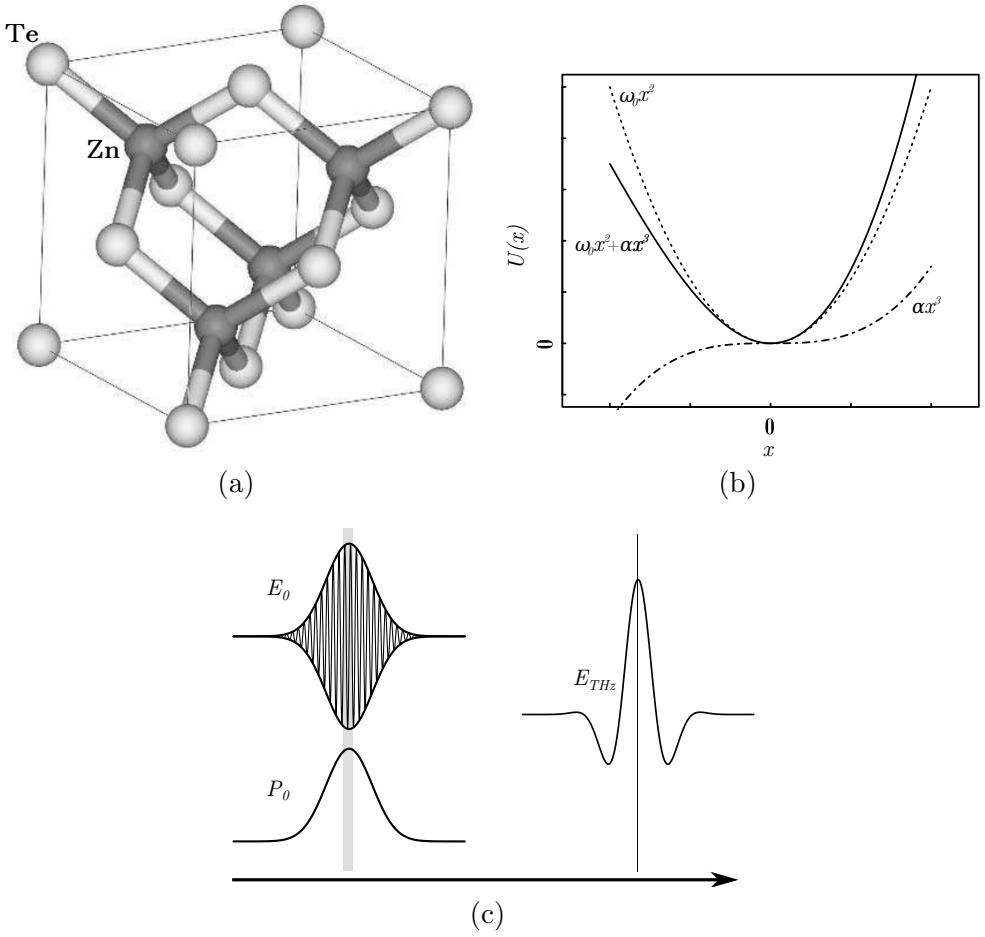

Figure 3.5: (a) The atomic structure of ZnTe [79] reproduced from [61]. (b) The non-linear potential due to the asymmetric bond between the Zn and Te atoms, the solid line is the combined potential with the dashed dotted line and dotted lines being each of the components of the Taylor series. (c) The optical excitation pulse, with the induced polarisation in a very thin non-linear crystal, and the resulting terahertz pulse.

are non-zero, only one of which is independent. From this the intensity of the terahertz generation can be shown to depend on the optical pulse's orientation related to the crystal structure, by

$$I_{\mathrm{THz}}(\theta,\phi) \propto |\vec{P}|^2 = 4\epsilon_0^2 d_{14}^2 E_0^4 \sin^2\theta(4\cos^2\theta + \sin^2\theta\sin^2(2\phi)) \tag{3.5}$$

which is maximised when $\sin^2(2\phi) = 1$ ($\phi = \frac{\pi}{4}$ or $\frac{3\pi}{4}$). Where θ is the polar angle and the azimuthal angle is ϕ. Therefore, the maximum is when the optical polarisation lies in the $\{1\,1\,0\}$ plane. But considering a beam incident on a $(1\,1\,0)$ ZnTe crystal, with some angle (θ) between its linear polarisation axis direction and the $[0\,0\,1]$ axis, there

is a maximum in the terahertz intensity at $\theta = \sin^{-1}\sqrt{\frac{2}{3}}$. Corresponding to an optical field aligned with the Zn - Te bond. It can also be shown that the generated terahertz field (E_{THz}) depends on the polarisation state of the optical pulse in relation to the lattice with $E_0 \parallel [\bar{1}\,1\,1] \rightarrow E_{\mathrm{THz}} \parallel -E_0$ and $E_0 \parallel [\bar{1}\,1\,0] \rightarrow E_{\mathrm{THz}} \perp E_0$. There are other angle restraints which are considered below.

To find the generated pulse shape from the induced polarisation of the crystal a wave equation can be formed

$$\begin{aligned} \frac{\partial^2 E_{\mathrm{THz}}(z,t)}{\partial z^2} - \frac{n_{\mathrm{THz}}^2}{c^2}\frac{\partial^2 E_{\mathrm{THz}}(z,t)}{\partial t^2} &= \frac{1}{\epsilon_0 c^2}\frac{\partial^2 P_{\mathrm{THz}}^{(2)}(x,t)}{\partial t^2} \\ &= \frac{\chi^{(2)}}{c^2}\frac{\partial^2 |E_0(z,t)|^{(2)}(x,t)}{\partial t^2}, \end{aligned} \tag{3.6}$$

where it is assumed that the incident optical pulse is linearly polarised and propagating in the z direction and n_{THz} is the refractive index of the crystal in the terahertz domain [61, 74]. Firstly consider a thin non-dispersive medium, a Gaussian polarisation induced by optical rectification due to an incident optical pulse, the resultant generated terahertz radiation is proportional to the second order time derivative of the Gaussian wave form [61]. For a 'thick' sample a sum of these thin layer generations can be used. The frequency difference between the generated radiation and that of the optical pulse is large and the refractive index is therefore unlikely to be consistent between the two (the material will be dispersive). There will therefore be some lead or lag between the generating optical pulse and the generated terahertz pulse. Ideally non-linear crystals must also be birefringent, and in an ideal situation an axis will exist where the two refractive indices match, resulting in continuous increase in the terahertz pulse power with no spreading [13, 61]. This matching condition adds an additional angle dependence. ZnTe is no birefringent but fortunately the group refractive index of ZnTe being around 2.85 at 800nm and 1.5THz [13]. The alignment of the generation crystal is best done by setting the temporal overlap on the detector to the first peak in the measured electric field (see above) and then rotating the generation crystal until this is maximised.

Both generation in non-linear crystals and photoconductive antenna result in similar terahertz pulses, but it is worthwhile considering the dependency of the peak terahertz electric field on the optical pulse fluence. Fig. 3.6 shows these relationships, based on equation from Lee [61]. As can be seen if the laser fluence is above $\approx 1.3\mathrm{mJ/cm}^2$ optical rectification has an improved generation efficiency, this is the domain in which the spectrometers used in this project are designed to operate.

The time resolved detection of terahertz radiation is obviously as important as pulse generation, but traditional detection methods such as bolometers, Golay cells

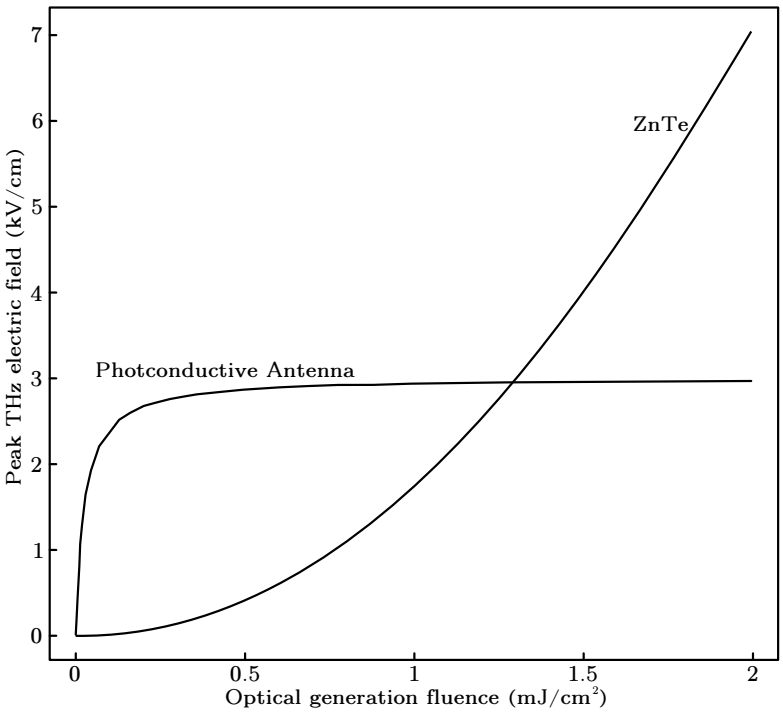

Figure 3.6: The dependence of the peak terahertz electric field on the fluence of the generating optical pulse for ZnTe (solid line), a non-linear optical rectification crystal, and a photoconductive antenna device (dotted line) with a 4 kV bias voltage.

and pyroelectric devices rely on measuring temperature changes and are therefore slow [61]. The two devices discussed briefly here are the reverse devices to the two generation methods discussed above, where the terahertz pulse can be considered as an applied DC field over the very short period of the optical probe.

In the photoconductive antenna devices, applying an external electric field and then exciting charge carriers with an optical pulse results in a real current being measured between the two electrodes on the semiconductor substrate which is proportional to the strength of the external field [55, 72]. The optical pulse can be moved through time relative to the terahertz pulse, which can therefore be profiled in time.

For the non-linear crystal detection method, electro-optical sampling, the Pockels effect is observed. Here an applied DC field (the terahertz pulse) results in an induced birefringence in the electro optical crystal resulting in a modification to the transmitted optical detection pulses polarisation. This can be quantified by

$$P_i^{(2)}(\omega) = \sum_j \epsilon_o \chi_{ij}^{(0)}(\omega) E_j(\omega), \tag{3.7}$$

where $\chi_{ij}^{(2)}(\omega) = 2\sum_k \chi_{ijk}^{(2)}(\omega, \omega, 0) E_k(0)$ is the susceptibility tensor induced by the field

[64, 75, 80]. In a lossless media, $\chi^{(2)}_{ijk}(\omega,\omega,0) = \chi^{(2)}_{ijk}(0,\omega,-\omega)$ therefore this has the same non-linear properties as generation by optical rectification and is governed by the same physical origins [64, 75, 80]. Thus this process again depends on the relationship between the crystal structure and the polarisation state of the two incident beams. Here the refractive index is important as the sampling of the terahertz pulse will change with distance through the crystal if there is a lead or lag between it and the optical pulse. To detect the change in polarisation state a $\lambda/4$ plate is used to convert the beam back into linearly polarised light. This is split into its two component polarisations using a beam splitting polariser, and the relative intensities of the two polarisation states can be measured on a pair of balanced photodiodes as discussed above. Again, this process is polarisation dependent which complicates the alignment [81]. The most effective method is to first maximise the generation as described above, and then rotating the detection crystal to a maximum and re-rotate the generation crystal. This should be repeated until no increase in the measured field can be observed.

Recently there have been some further modifications to these types of spectrometers, with the ability to measure near field terahertz effects [82] and the polarisation of the terahertz pulse without moving any component required [83]. Direct generation of terahertz surface waves has also been shown to be possible [84]. In addition to the blade coupling method used in [36], an attenuated total reflection spectroscopy system has been developed that could also be used to couple into plasmon modes [85]

3.1.2 Photodiode detectors

The need for using balanced diodes as opposed to monitoring the single polarisation intensity stems from both the very low generation efficiency (the terahertz pulses are sub-nanoJoule in energy), and the very small induced birefringence in the detection crystal. The polarisation intensity change is therefore small and would be dwarfed by any intensity fluctuations between pulses. Using balanced diodes allows this to be eliminated from the measurement, as an increased pulse intensity will provide an equal increase in signal on both diodes which will be removed electronically if the diodes are well balanced.

The measured signals are very low, and ultra fast, to enable better sampling the electronic signals can be amplified and stretched. Some work has been conducted through the course of this project, with the assistance of Tom Isaac, in the building and testing of varying designs of balanced diodes as well as SPICE modelling [86].

All of the designs discussed here employ operational amplifiers (op-amps) and high speed photodiodes. Some improvements to the signal to noise ratio can be made simply by improving the response of these components such as reducing the detectors physical

area, reducing its capacitance [87]. Op-amps can be employed for a number of different applications depending on the inputs and feedback between the output and the input [87]. Their most common use here is as amplifiers where a parallel resistor and capacitor are connected between the output and the positive (negative for an inverse amplifier) input. The other implementation involves signals being applied to both inputs as well as the feedback loop resulting in an amplified differential signal. Varying the capacitance and resistance in the feedback allows for the gain and time constant of the amplifier to be modified [87].

The simplest device that can be envisaged is two anti-parallel photodiodes, connected to a single input of an op-amp, the differential signal from the two diodes is amplified, this simple circuit is shown in fig. 3.7(a). This device suffers from the possibility of time lag between the two diodes, so the subtraction would not be of one pulse from another but, from close to one pulse to another, depending on differences in the diodes, optical path and electronics linking them. The true difference would therefore not be amplified. Also, the common-mode rejection, a feature of op-amps is not utilised. It is also worthwhile to note that here the photodiodes are unpowered, therefore acting as voltage sources as opposed to current sources, this is more effective for low intensity detection not the high intensity pulses measured here [87].

The next step is therefore to correct the above problems. This is done by splitting the diodes into two branches as shown in fig. 3.7(b), applying a bias voltage across them and having them individually amplified by an op-amp before subtraction. The output from the two op-amps goes into the two inputs of a third, acting as a differential amplifier. This circuit improves the measurement but suffers from problems. The very fast pulses that are measured can be stretched in their branches, but saturation of the third op-amp then occurs. Otherwise stretching can occur in the third op-amp which severely restricts the differential gain.

What is needed is to perform the differential operation, with amplification, followed by stretching and a subsequent amplification. This is all satisfied by the circuit shown in fig. 3.7(c). In this circuit the branches are again 'pre-amps' with biased photodiodes, with the differential operation happening at the input of the third op-amp, which is in an inverted amplification configuration. The output from this op-amp is fed into a sample and hold chip, this device takes a single voltage reading at a given frequency set by an external trigger, and outputs a continuous voltage at the measured value. This is again amplified, resulting in a significantly larger signal to noise ratio, using this circuit design a signal to noise ratio of close to 5000 : 1 can be achieved in an acquisition time of less than 2 minutes, compared to maximums of 1000 : 1 for the previous circuit. SPICE modelling was conducted up to the node before the signal and hold to allow comparison with the previous circuits and allow for the components in the feedback

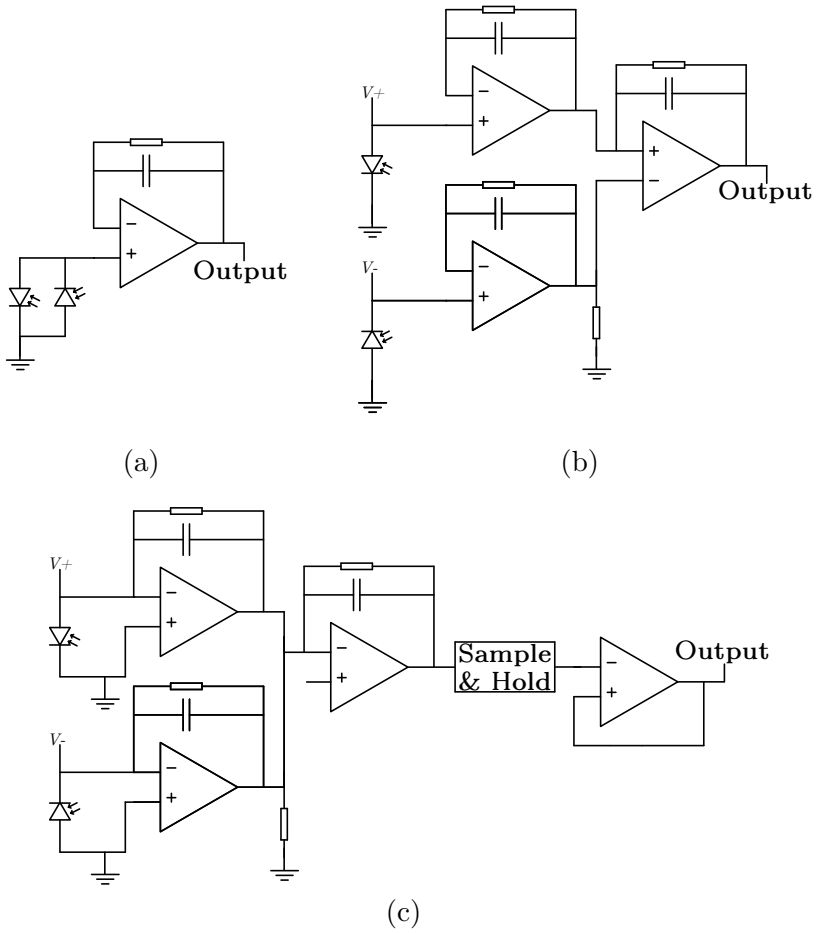

Figure 3.7: The three considered circuit diagrams for balanced photodiodes. It should be noted that these diagrams are simplified containing only the most important components. (a) The situation where the diodes are unpowered and in parallel, their direct differential is then amplified. (b) Has two 'pre-amps', one for each of the diodes, the differential operation is conducted using an op-amp. (c) The pre-amps and differential amplifier are supplemented by a sample and hold stage to conduct the stretching, this is then amplified by a fourth op-amp.

loops to be optimised.

3.2 Sample self adhesive support

For ease of experimentation it is often required to support a structure or sample on a substrate. This can easily be achieved at optical frequencies by the use of glass and evaporating metal onto the surface, as used in processes such as nanosphere lithography discussed in section 4.1. For microwave samples materials of known dielectric properties are used for printed circuit board (PCB) onto which metals can be deposited or etched, or the samples are large enough to be free standing and self supporting. At THz frequencies when working with semiconductors the material cannot be deposited easily in single crystal form and structures need to be formed from fully grown wafers (see chapter 6). These often require supporting with some self adhesive substrate. In some cases quartz can be used as an alternative to glass, but the absorption of quartz substrates is still large [54, 61]. To this end different pressure sensitive self adhesive films (SSAFs) have been briefly characterised using a focussing terahertz spectrometer. The time domain results of the transmission through the various films can be seen in fig. 3.8, from this it can be seen that the plastic thin film produced the smallest perturbation from the free space terahertz pulse. It should be noted that extraction of the refractive indices of these materials is possible from the data (see chapter 5) but due to the varying thickness the perturbation from the reference signal is more useful. The deviation from the reference is not the only concern. Another factor to be taken into account when considering these films, the resistance to chemical wet etching, where the thin plastic film proved more resilient than the thick plastic insulating tape, although it is more susceptible to the glue failing when wet.

With the final concern being the possible birefringence of the film [88]. It is known that cellulose SSAFs have a very high birefringence due to the alignment of the cellulose chains. This has been shown to be of little consequence for thin plastic film at THz frequencies by the observation of the peak THz transmission whilst rotating the film in the beam.

3.3 Optical spectra

Optical spectra have been used in this project for the characterisation of optical particle plasmon arrays in chapter 4. These techniques measure the response of the sample to incident radiation, over a range of different frequencies. There are three different effects when light is incident on a sample, reflection (R), transmission (T), and absorption (α),

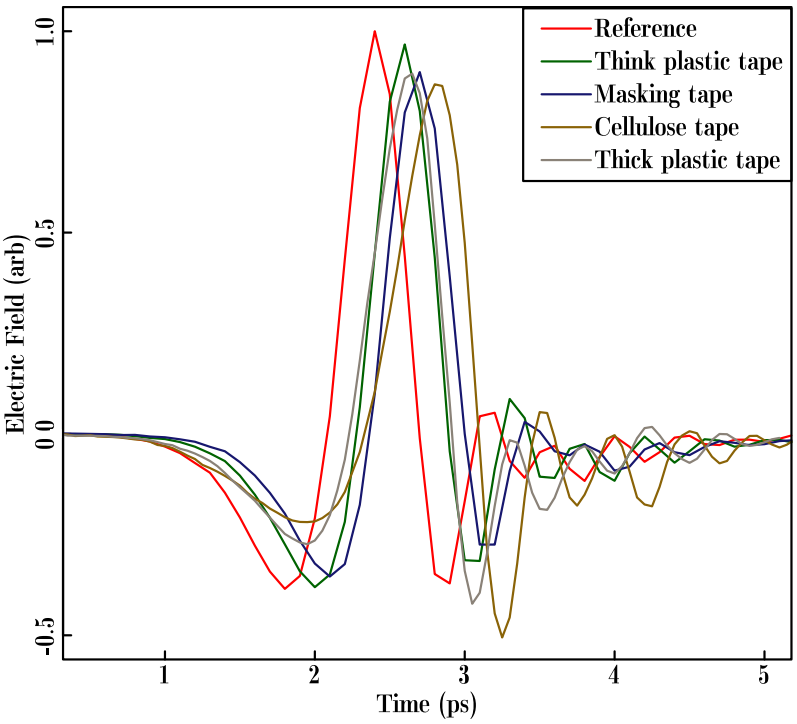

Figure 3.8: The time domain transmission through 4 different self adhesive pressure sensitive films, shown with a free space transmission through the focussing THz spectrometer.

which are linked by

$$R + T + \alpha = I, \tag{3.8}$$

where I is the intensity of the incident light [78]. Illuminating the sample with a white light source and then collecting with an optical microscope objective all the light that is emitted into either the hemisphere above (reflection) or the hemisphere below (transmission) to be directly measured from which the absorption can be found [51]. In this project the absorption was found by a collegue Dmitry Polyushkin using a tightly focused spot on the sample before the collected light was split into its component frequencies using a diffraction grating. A CCD was then used to measure the intensities in both reflection and transmission.

3.4 Finite Element Method Modelling

Finite element method (FEM) modelling, a numerical modelling technique, has been used extensively throughout this project. Here a brief introduction is provided. The software package used is Ansys HFSS versions 10 - 13 [89].

Analytical solutions for surface waves have been greatly utilised, but can be very

complicated, and impossible to solve for certain systems, such as asymmetric systems and those with hard to define boundary conditions. In these cases FEM can be used. Firstly a system must be defined, here that is done by drawing 3D objects in a design package and defining their permittivity and permeability. For free space systems the system is surrounded by an 'air box' on the faces of which boundary conditions can be defined.

The modelled system is split into many small elements (tetrahedra, 3D shapes with 4 triangular sides), inside which Maxwell's equations are solved using the boundary conditions provided by all the surrounding elements, this is done using a matrix method [90]. This method allows for a complete analysis of the electromagnetic properties of an arbitrarily complex composite system, limited only by the available computing power.

3.4.1 Boundaries

A number of different boundary conditions can be applied, these apply restrictions on the electric and/or magnetic fields at those surfaces. The following is a brief description of the most common. Master and slave boundaries are the most utilised boundary type in this project, and are always used in pairs, with each master having an associated slave. It is a condition of the system that the field profile on the master must be identical to the field profile on the corresponding slave, they can therefore be used to create an effectively infinitely long structure. By using sets of these boundary pairs infinite periodic arrays can be modelled by only solving the fields for a single unit cell.

Perfect E, and perfect H boundaries constrain the electric or magnetic fields, respectively, to be orthogonal to the plane of the boundary. This can be useful for creating symmetry boundaries, as the constraint is the same as for a perfect electric or magnetic mirror. Therefore symmetric samples can be modelled by drawing only half of the system.

The above described boundaries are most useful on the sides of the air box, but for above and below the sample, it is normally required for the system to be open to free space, so these boundaries must not interact with the system (absorb all incident radiation). This can be achieved by using "radiation" boundaries or perfectly matched layers (PMLs). Radiation boundaries only offer no reflections for radiation that is at normal incidence to the surface, whereas a PML works at a range of angles. They introduce a new object, matched to the refractive index of the model at the boundary with a graded refractive index increasing as you move further from the boundary, therefore acting as a perfect anti-reflection coating. These boundaries should be used when considering samples where diffraction is expected or off-normal excitation is required.

3.4.2 Incident wave solutions

So far there has been no discussion of the excitation mechanics for these models. There are two main types of solutions used in this project, driven and eigenmode. The excitations discussed here are used purely for driven models, where an incident field is applied and then the results observed, with eigenmode solutions being discussed below. The solution software used offers different options for excitation waves, the simplest of which is a plane wave, which is defined by a wavevector ($\vec{k}$) and polarisation ($\vec{E}$). These waves are viewed as coming from infinity until being incident upon the model. Similarly Gaussian beams can be defined, where the beam waist and location are added to the initial parameters. Although this is more realistic the beam waist is often larger than a single unit cell and therefore real sized samples need to be modelled, this is often infeasible due to the computational power required. When the unit cell is much smaller than the beam waist, the incident light can be well approximated to a plane wave.

The other excitation method employed in this project is that of Floquet port analysis, which can only be used for planar-periodic structures [91]. For this method, the boundary conditions on the ends of the air box need to be changed from their PMLs or radiation boundaries to Floquet boundaries, with the software solving the model for Floquet modes. The set up requires the number, and type of modes to be evaluated to be defined, these should include the zeroth order mode and any diffracted order into which power will leak, for both polarisation states. For highly diffracting models the full analysis is often not possible due to the computational requirements, but where it can be used this solution method can add understanding, as the transmission and reflection of the different diffracted orders can be observed [91].

3.4.3 Eigenmode solutions

The other method utilised in this project to solve FEM modelling systems is eigenmode analysis. Here a unit cell of an infinite structure is drawn and fields are attempted to be fitted inside the system, to find the eigenmodes of the unit cell of the structure. The largest drawback to this method is for free space samples: the containing air box will also have associated eigenmodes which cannot be distinguished from sample modes by the solver. A human operator can compare the field plots for the modes and distinguish them, although this is complicated by the possibility of hybrid modes between those of the air box and those of the sample.

A phase delay can be forced upon the modes between a pair of master slave boundaries, this can be related to the wavenumber (k) in the direction of the normal of the

boundary surface by

$$\omega = \frac{d\phi}{dt} = \frac{2\pi c_w}{\lambda} \Longrightarrow \frac{\Delta\phi}{L} = \Delta k, \tag{3.9}$$

where ω is the angular frequency of the mode, ϕ is the phase, L is the path length (the unit cell size), and c_w is the wave speed. It is therefore possible to find the dispersion directly from a model, which can be directly compared to the measured dispersion found in phase sensitive measurements, where L is the path length between the two couplers and the relative phase is found using a reference sample.

3.4.4 Element meshing

The size and shape of elements used in FEM greatly effects the end results of the model. Consider a metal dielectric interface. The fields incident from the dielectric side will decay exponential into the metal. If the metal is represented by only a single element the exponential decay cannot be represented, as a single element cannot express changing fields. There are in fact three important factors for the number of elements required in any given region, feature size, wavelength (taking refractive index into account), and field gradients. The first two can be accurately satisfied by initial mesh parameters, using a user defined frequency to preform a wavelength based initial meshing operation.

The field gradient effect is a greater problem as it requires a solved model to find where the system needs extra elements to solve the model. This can be circumvented by using adaptive passes. The model is first solved for a single user defined frequency using the initial mesh conditions. A simple refinement to the mesh is then conducted, where more elements are added with a weighting to add more to areas of high fields. This is repeated, with the solutions being numerically compared, once this comparison is below a user defined fraction the system is considered converged and no more passes are required. The model is then solved for all the required frequencies.

3.4.5 Uses

FEM modelling of this type can be used to find the eigenmodes of a system as described above, or the transmission, reflection and absorption. Additionally the fields (either time averaged or at a single point in the phase cycle) can be evaluated at any place in the model. Allowing for field enhancements to be found in regions surrounding structures.

Chapter 4

Nanoparticle plasmonic generation of terahertz radiation

In addition to the common applications of particle plasmons discussed briefly above there has recently been many novel applications developed utilising the subwavelength confinement of light. These include data storage [92], therapies for cancer [93] and the generation of deep-UV/soft X-rays by high-harmonic generation [94]. Most applications exploit the spatial confinement of fields in the vicinity of plasmonic nanostructures. This chapter develops a description of a phenomenon which relies on both the fields inside and outside the material.

When ultra short pulses are incident upon nanostructured metals there is a photoemission of electrons observed, even when the photon energy is below the work function of the metal. This effect depends upon the field strength inside the metal and has been studied in planer metal films [95], islandised metal films [96] and metal gratings [97, 98]. These studies suggest that the photoemission depends on the plasmon modes of the metal surfaces.

This burst of high energy photoelectrons may be accompanied by the emission of terahertz radiation. Emission from accelerated charges is a well known phenomenon [99]. Emissions have been observed following the illumination by femtosecond laser pulses of rough planer metal sheets [100, 101], metallic gratings [102, 103] and islandised metal films [104].

It is proposed that the plasmon modes induce two effects. Firstly, the enhanced field inside the metal boosts photoelectron emission. Secondly, the very high external field gradients, due to the confinement, accelerates the electrons through the ponderemotive force [105] resulting in high energy photoelectrons [106], a schematic of this is shown in fig. 4.1. Briefly, a ponderemotive force is a non-linear force that depends on the

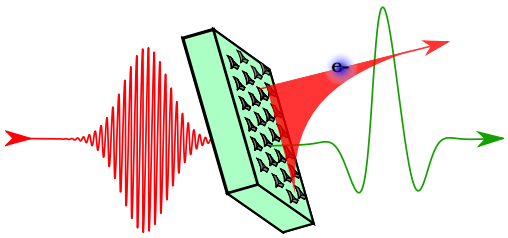

Figure 4.1: A schematic of the proposed generation method.

gradient of the electric field squared, expressed by

$$\vec{F}_p = -\frac{e^2}{4m\omega^2}\nabla\vec{E}^2 \tag{4.1}$$

where e is the charge of the accelerated particle, m is its mass, ω is the angular frequency of the field and $\vec{E}$ is the electric field. A counter proposition to explain the emission of terahertz radiation is an optical rectification effect proposed in [100, 101, 104, 107]. The photoexcitation description appears more consistent than optical rectification to the power dependencies measured in [102, 103, 108]. This is discussed in greater depth below.

In this chapter, experimental data of nanoparticle arrays is considered with numerical modelling, and a proposed basic model for the generation process is developed. The experimental results provide evidence for generation from nanoparticles previously predicted by Gao et al. [109]. The following data was collected with the assistance of Dmitry Polyushkin, with the proposed modelling being developed with collegues Dmitry Polyushkin, Euan Hendry and Bill Barnes, and sample fabrication by Dmitry Polyushkin, the author is indebted to them.

4.1 Samples

Two different sample types have been investigated to enhance the understanding of the observed phenomenon. The first are islandised films, similar to those investigated by Ramakrishnan and Planken [104]. The fabrication method employed for these films is the deposition of very thin metallic layers by thermal evaporation. Here a substrate (glass) is suspended above a 'boat' into which the metal to be deposited is placed. The chamber is evacuated to $< 10^{-5}$ mbar and an electric current passed through the boat heating it via Joule heating, this results in the evaporation of the metal. The metal subsequently condenses on the surface of the sample. A thickness monitor placed alongside the sample measures the change in vibrational resonance of a quartz crystal as material is deposited. This is used to provide an indicator to the mass-thickness,

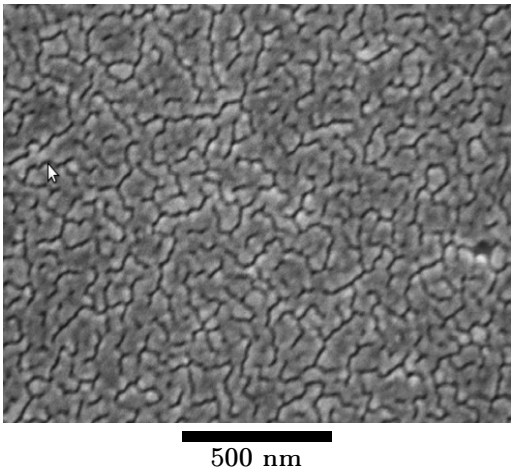

Figure 4.2: A scanning electron microscope image of an islandised film, with a mass-thickness of 12 nm, the narrow channels the film are clearly illustrated.

the thickness of an equivalent continuous film, and the deposition rate of the metal.

For films deposited in this way, below ≈ 10 nm, with a deposition rate of ≈ 0.1 nm/s, the metal does not fully wet the surface, and metal islands are formed [110, 111]. Fig. 4.2 shows a scanning electron microscope (SEM) image for an islandised film made in this way, with a mass-thickness of 12 nm. The discontinuous character of the film is clearly illustrated.

The second type of sample, arrays of nanoscale triangles, requires a more involved fabrication method, nanosphere lithography (NSL) [53]. Briefly, clean substrates are submerged in ultrapure deionised water (fig. 4.3(a)), before a suspension of polystyrene colloidal nanospheres are added to the surface. These self-assemble into a close packed, hexagonal, monolayer array, as shown in fig. 4.3(b). The water evaporates leaving the array deposited on the substrate (fig. 4.3(c)). This can be used as a lithography mask for metal evaporation (fig. 4.3(d)). Finally the nanospheres can be dissolved leaving a hexagonal array of triangular shaped nanoparticles, as shown in fig. 4.3(e). An SEM image for a typical array of these particle is shown in fig. 4.4, the domain size for a regular array of triangles fabricated in this way is ≈ 25 mm^2.

A range of these samples have been used, with different metal deposition thicknesss and two different nanosphere diameters (780 nm and 390 nm). To characterise the various samples, optical extinction spectra were taken as described in section 3.3. For the NSL samples, care must be taken to ensure sampling of monodomain regions. These spectra can be seen in fig. 4.5(a) for islandised films, and 4.5(b) and 4.5(c) for NSL samples. From these it can be seen that islandised films have very broad extinction peaks, showing no well defined plasmonic resonance. Whereas, the samples fabricated

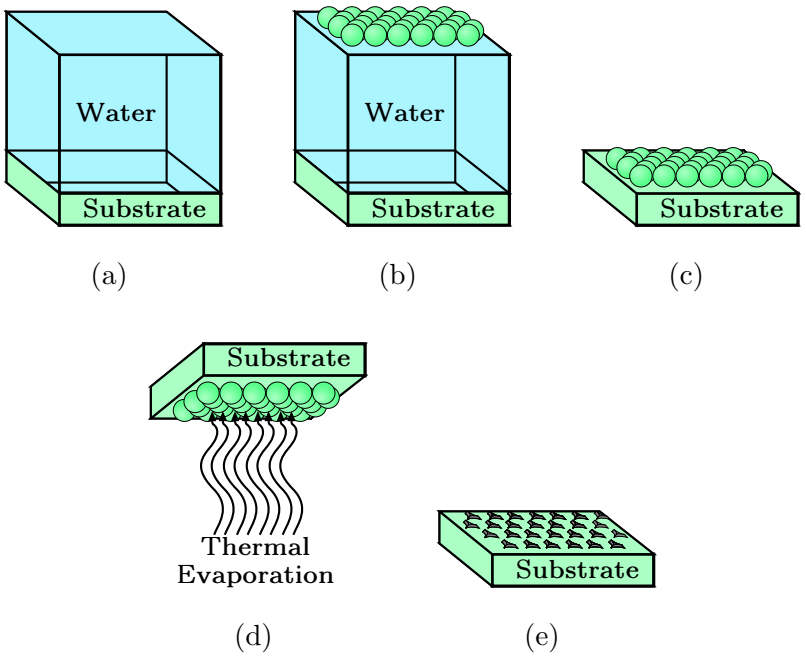

Figure 4.3: Nanosphere lithography method for creating nanoscale triangles, polystyrene spheres are suspended on ultrapure water above a substrate (a) and (b). (c) the water evaporates resulting in a self assembled hexagonal monolayer of spheres on the substrate, onto which metal is evaporated, and the spheres subsequently dissolved (d) and (e).

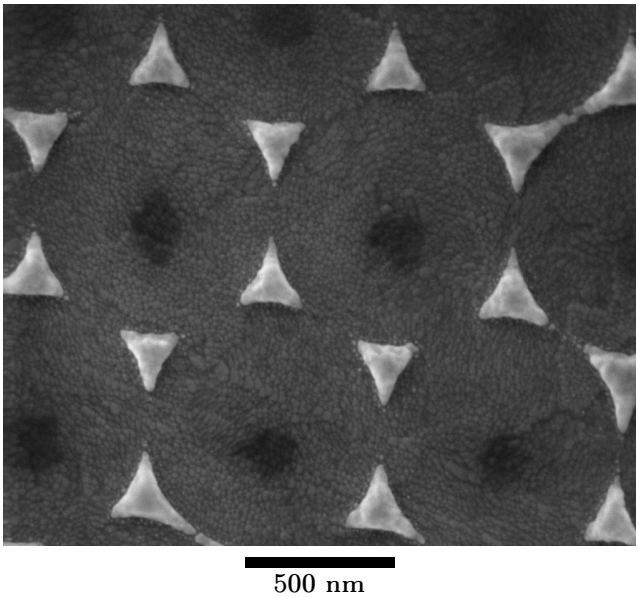

Figure 4.4: A scanning electron microscope image of an array of triangles fabricated using 780 nm diameter spheres using nanosphere lithography with a deposited metal depth of 50 nm.

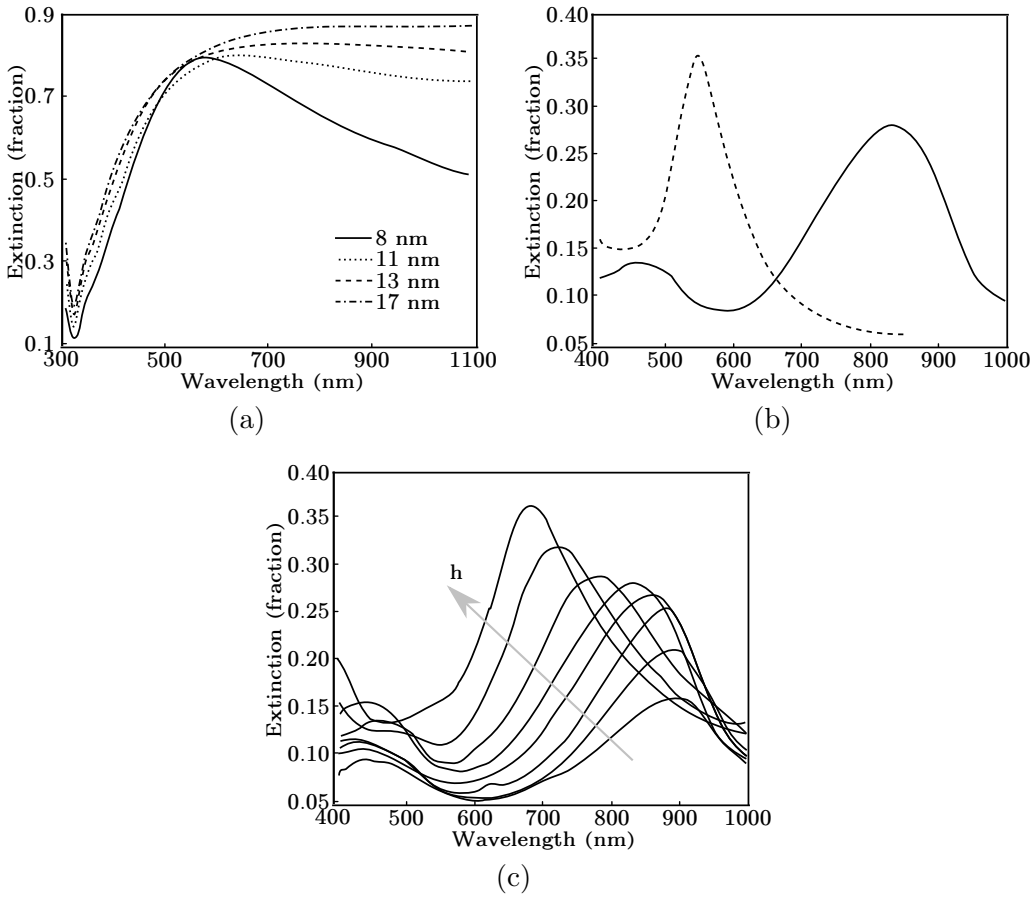

Figure 4.5: Optical extinction spectra for, (a) islandised films with different mass-thicknesss, (b) NSL fabricated samples with two different sphere diameters, 780 nm and 390 nm, and (c) NSL fabricated samples, using 780 nm diameter spheres, with a range of different thickness (h) triangles, $h = 20,\ 30,\ 40,\ 50,\ 60,\ 70,\ 100$ and 150 nm, the arrow indicates the increasing thickness for the spectra.

using NSL shown in figures 4.5(b) and 4.5(c) show very clear resonances. For 780 nm diameter spheres as the amount of deposited silver changes (particle thickness), the peak of the plasmonic resonance rasters across the optical wavelength of the laser (800 nm). The importance of this will become clear below. In the case of the arrays fabricated using NSL the peak in the extinction spectra corresponds to the dipolar particle plasmon resonance of the particles [45].

4.2 Experimental set up

The sample to be investigated is mounted to replace the ZnTe crystal in the focussing terahertz spectrometer described in section 3.1. The mounting allows for movement in

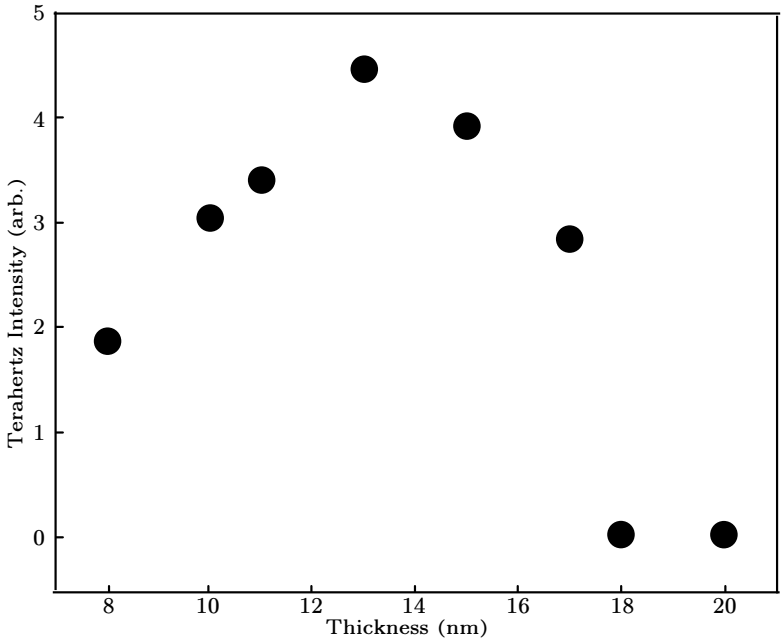

Figure 4.6: The peak terahertz intensity measured from islandised films with different mass-thickness.

the x, y, z, directions and changes in both the azimuthal and inclination angles. The generating 800 nm pulses are focussed down to ≈ 1 mm, providing energy densities up to 9 mJ/cm^2, corresponding to a peak power intensity of 90 GW/cm^2. Any generated terahertz radiation is collected, collimated and sampled in the normal way explained above.

4.3 Islandised films

The islandised films are illuminated by the ultrafast laser system at an angle of $\approx 40°$, and terahertz emission is observed. The peak terahertz intensity for a range of different mass-thickness's of silver is shown in fig. 4.6. There is a clearly observable peak at $\approx$ 13nm. This peak generation occurs when the islands are large enough to join together, i.e. are above the percolation threshold, this can be confirmed by conducting resistance measurements across the samples.

The higher mass-thickness samples ($>$ 11 nm for Ag) show no clear peak in extinction, indicating that there is no plasmonic resonance. As the peak terahertz generation occurs for samples with greater mass-thickness this might be considered evidence that this is not a plasmonic effect. But just because there is no clear extinction resonance does not mean that there are no plasmonic resonances [112]. The percolating films are full of narrow channels between the islands. These channels can support very high field

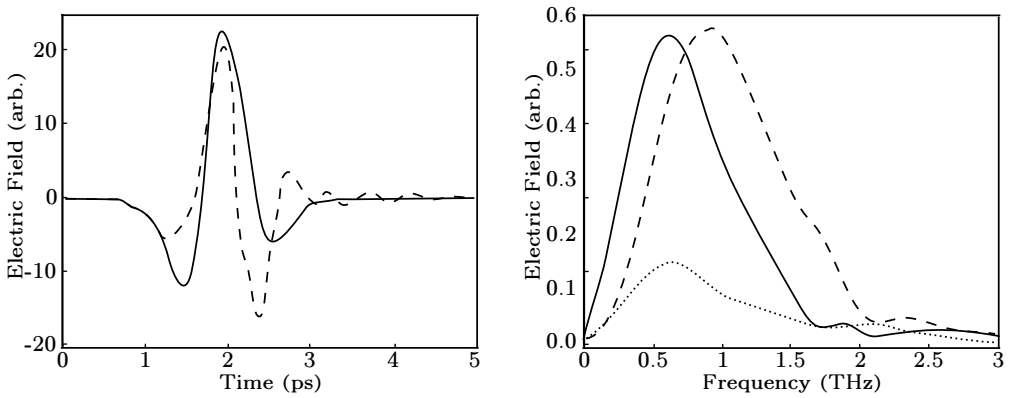

(a) (b)

Figure 4.7: (a) The time domain generated terahertz transmission from a 1 mm ⟨1 1 0⟩ ZnTe crystal (dashed line), and an array of triangular particles fabricated from nanosphere lithography using 780 nm (solid line) diameter spheres. (b) The frequency domain measurements of the generated terahertz signal, also shown (as the dotted line) is an array of triangles fabricated using and 390 nm diameter spheres.

enhancements [113], it is believed that these are responsible for the terahertz generation. Due to the difficulties of modelling these films, and making systematic changes to the structure, it is not feasible to conduct further analysis.

4.4 Nanosphere lithography arrays

To initially test the hypothesis that the terahertz transmission is related to the plasmon resonance of the samples, it is sensible to compare two similar samples, one where the 800 nm laser wavelength is close to the resonance and one where it is significantly different. This is easily realised by using two different sphere diameters, 780 nm and 390 nm, the extinction spectra for arrays fabricated using these two sphere diameters are shown in fig. 4.5(b).

The time and frequency domain measurements for these two samples are shown in fig. 4.7, the 780nm sphere fabricated sample is shown as the solid lines and the 390nm sphere fabricated sample as the dotted ones. For comparison the dashed line shows the time and frequency domain traces for the 'normal' 1 mm ⟨1 1 0⟩ ZnTe crystal, scaled down by a factor of 100. The greater terahertz signal generated for the arrays where the plasmon resonance is close to the laser frequency (solid line) clearly indicates the important role of the plasmonic resonance.

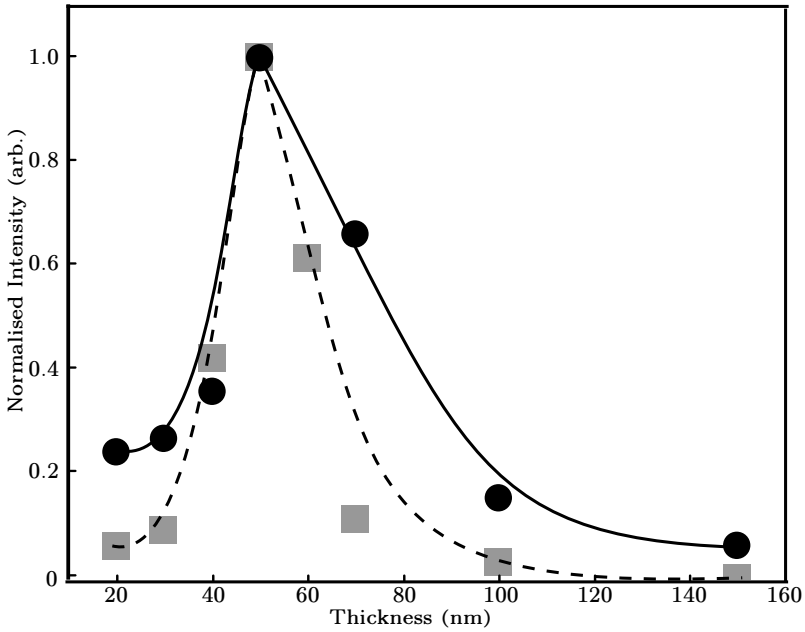

Figure 4.8: Dependence of the peak generated terahertz intensity on the thickness of particles at normal incidence (solid line, filled circles) and an inclination angle (angle of incidence) of 40° (dashed line, filled squares). The lines are shown to guide the eye. Both datasets are normalised to their respective peaks and the normal incidence measurements are around a factor of 10 smaller. The arrays was fabricated using 780 nm diameter spheres.

4.4.1 Thickness dependency

4.4.1.1 Experimental results

To further explore the relationship between plasmon resonances and generated terahertz radiation it is useful to have a range of samples where the peak in the plasmon resonance has different frequencies close to the laser wavelength. As shown above, this is achievable by varying the thickness of the particles [114]. Arrays have been fabricated using thickness's from 20 to 150 nm, giving resonant peaks in the range 650 nm to 900 nm, with the thickest particles having the shortest wavelength resonance. The closest match to the laser wavelength is particles with a height of ≈ 60 nm.

The thickness dependence on the peak terahertz intensity is shown in fig. 4.8, for both normal incidence (solid line, filled circles) and an inclination angle of 40° (dashed line, filled squares), normalised by their respective maxima. In both cases there is a very clear peak for 50 nm thick particles, close to the optimised resonance position for 60 nm thick particles, implying the resonant behaviour enhances the generation process.

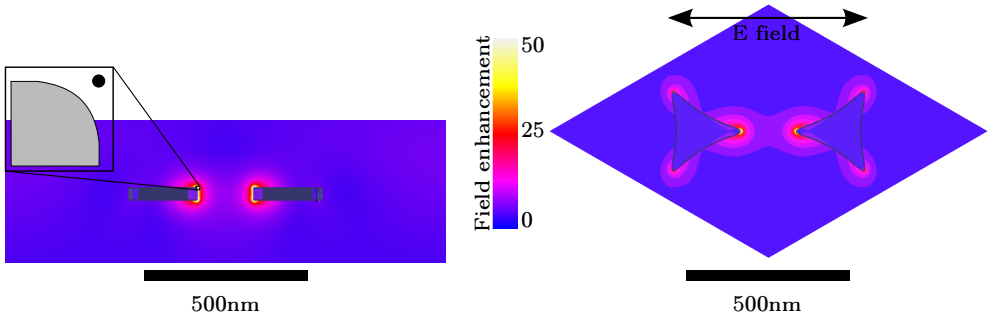

(a) (b)

Figure 4.9: Characteristic field enhancement distributions for 40 nm thick curved particles in a rhombic unit cell calculated using finite element modelling, illuminated with a wavelength of 800 nm. (a) In cross-section, where the inset shows the probe position for the maximum field enhancement plots. (b) Looking in plan of the particles.

4.4.1.2 Numerical modelling

To gain insight into the physical origins of the terahertz emission numerical modelling has been conducted [115, 116]. The Floquet port method described in section 3.4 is used with a rhombic unit cell containing two particles as shown in fig. 4.9. In this way an infinite hexagonal array can be modelled. The silver was modelled using a frequency dependent permittivity for silver [117], the incident radiation is polarised along the long axis of the particle pair as shown in fig. 4.9(b). To fully model the system several factors must be considered, the sloped sides of the particles, the curved sides and rounded points of the triangles, the rounded top and bottom edges of the particles and the substrate, these are explained in more depth below. Given the software package used, and the available computational power, it is not feasible to model all of these simultaneously, but their effects on the plasmon resonance position and local fields can be considered individually. The realistic features are added using measurements taken from SEM images. Fig. 4.10 shows the dipolar resonance in the reflection spectra for different combinations of the above different modifications. The grey lines show straight pointed triangles shown in fig. 4.11(a), with upright sides being the solid line and sloped sides being dashed, indicated in fig. 4.11(b). The introduction of sloped edges shifts the plasmon resonance to shorter wavelengths. This agrees with the brief discussion in section 2.3, that shorter particles have shorter wavelength resonances. For the other realistic modifications, it is not trivial to make predictions about their affect on the plasmonic resonance.

The introduction of a more realistic triangle shape as shown in fig. 4.11(c), reduces the "lightning effect" where fields are concentrated at sharp edges [49]. The reflection

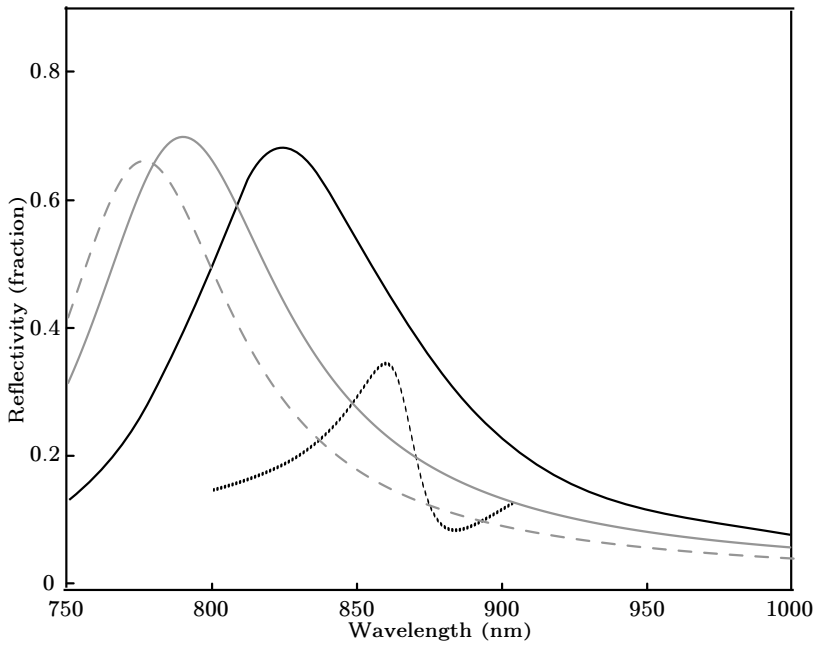

Figure 4.10: The dipolar plasmon resonance shown in the reflection spectra for different realistic modifications, modelled for triangles made from spheres with a diameter of 780 nm. The grey lines show sharp triangles, with the black lines being curved sided and ended triangles. The solid lines represent the normal triangles with non-sloped sides and no other modifications. The grey dashed line shows the situation for sloped sides, and the black dotted line shows the final modification, the inclusion of a glass substrate.

response due to the plasmon resonance for this particle shape is shown in fig. 4.10 as the black solid line, where it can be seen that this induces a shift to longer wavelength of the plasmon resonance compared to the straight sided triangle.

Analysing the field enhancements close to the particles shows that the strength is strongly influenced by the pointed edge between the top triangle and the curved side of the particle. This can be significantly reduced by introducing a curved edge, here a radius of curvature of 3nm is used. This modification is not shown in fig. 4.10 as the variation is indistinguishable from the solid black line. A larger curvature, as appears on the SEM images, creates a 3D model that cannot be drawn by the software package.

The other important factor is the glass substrate, the inclusion of this with the rounded particle (fig. 4.11(c)) creates a very computationally heavy model with the inclusion of many Floquet modes required to get a reliable solution. Despite this it has been solved for a single thickness where the calculated reflected spectra is shown in fig. 4.10 by the black dotted line, showing a shift to longer wavelengths of the plasmon resonance compared to when there is no substrate.

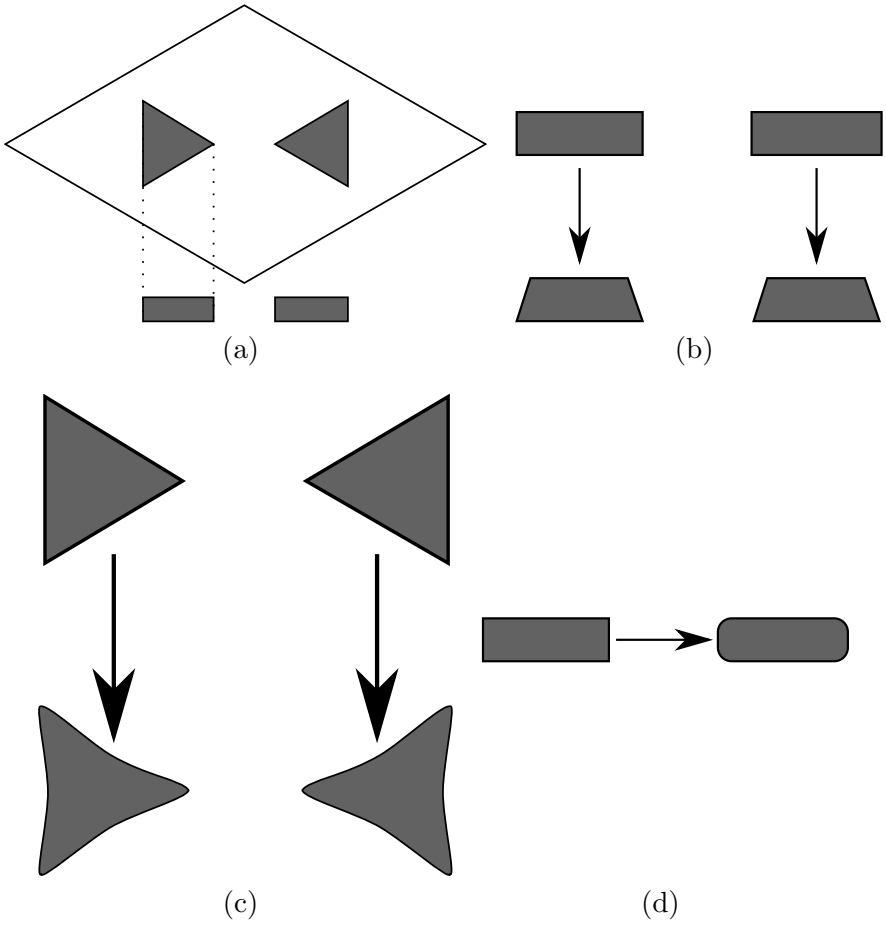

Figure 4.11: The realistic modifications made to the model. (a) The starting point with straight pointed triangles, (b) The difference between the straight sided and sloped particles, (c) The modification to the straight triangles to make the sides and points curved, and (d) showing the modification to the top (and bottom) edges to include a small amount of curvature.

Due to the computational difficulty of substrate models, and the difficulty of including sloped sides on curved particles, the approach chosen is the model with curved sides (fig. 4.11(c)) with rounded edges (fig. 4.11(d)). This method incorporates the most realistic modifications and therefore the field profiles are closest to those in the experiment. Varying the particle thickness again rasters the peak in the dipole resonance across what would be the laser wavelength (800 nm) as shown in fig. 4.12(a).

If the generated terahertz radiation is related to the plasmon resonance it is expected that as the peak of the resonance crosses over the laser wavelength the local field enhancements should show a similar trend to that seen in fig. 4.8. It is not trivial to decide on how to analyse the field enhancements, which can be calculated by normalising to the incident field strength. It seems reasonable to integrate over a volume

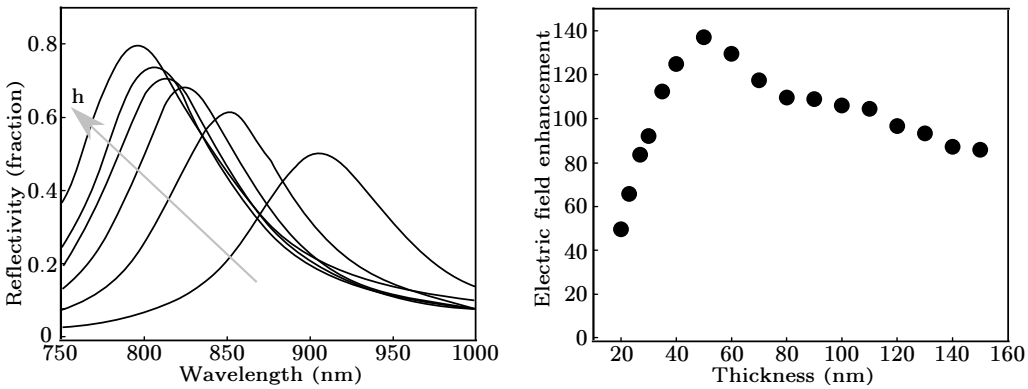

Figure 4.12: Results of numerical modelling for curved triangular particles with rounded edges, (a) reflection spectra for different thicknesses, $h = 20,\ 30,\ 40,\ 50,\ 60$, and 90 nm, the arrow shows the direction of increasing thickness and (b) the dependence of the peak field enhancements at 800 nm on the thickness of particles at normal incidence.

or area around the particles, as some measure of the average field enhancement. Although it is unclear as to the most appropriate volume or area to use. It may also be appropriate to consider the fields inside the particles.

There are several inherent disadvantages to these integration approaches. Consider a method where a plane is selected so that the normal to the surface is in the z direction cutting through the middle of the particles (fig. 4.9). As the particle thickness changes, the distance of the plane from the regions of highest field, shown in fig. 4.9 to be around the corners of the top and bottom surfaces, changes. This alters their influence on the field strength at the plane and therefore the integral result. A similar failing applies for volume integration methods, changing the particle thickness changes the amount of metal inside the integrated volume, this modifies the field enhancement values in the region. It is therefore necessary to use some method that circumvents these difficulties. This can be done by considering the maximum field enhancement at a point close to the particles that is only greatly effected by the high fields at one location. The point used is at the centre of the high fields at the 'point' of one of the triangles as shown in the inset of fig. 4.9.

The modelling indicates in fig. 4.12(b) that the optimum particle height in terms of field enhancement is when the plasmon resonance is close to the excitation wavelength. As predicted the trend shows a peak similar to that of the generated terahertz intensity (fig. 4.8). In both cases the peak is for a thinner particle (50 nm for numerical modelling, 4.12(b)) than the plasmon resonance peaks would imply (where the closest peak resonance to the excitation wavelength is for particles with a height of 60 nm, for

numerical modelling, 4.12(a)). This supports the idea that the generation method is plasmon mediated.

From the modelling, the local fields can be seen to be inhomogeneous, with the high field enhancements concentrated at the vertices of the particles, along the direction of the illumination polarisation. This field distribution exhibits a spacial centre of symmetry, the importance of which in terahertz emission is discussed later.

4.4.2 Optical intensity dependency

Shown above is evidence that the plasmon field is involved in the generated terahertz radiation from nanostructured arrays, however its precise roll is still not clear. In an attempt to investigate this, the dependence of the peak generated intensity on the intensity of the incident 800 nm laser pulse has been measured. The dependence is illustrated in fig. 4.13. Here the dependency of the fluence of the generated terahertz radiation on the intensity of the incident 800 nm pulse is shown for both a normal ZnTe $\langle 1\,1\,0 \rangle$ crystal (circles and dashed line) and an array of triangles fabricated using NSL, with a sphere diameter of 780 nm and a particle thickness of 50 nm (squares and solid lines). The lines are fitted order dependencies for different regions of the data. For normal optical rectification it is known that the power dependency of generation will be 2^{nd} order [13], the measurement for ZnTe supports this. The presented measurements for the NSL array display three distinct regions. For low intensities $< 5\text{GW/cm}^2$ the generated intensity shows an 5^{th} order dependency on the incident optical intensity, dropping to $< 2^{\text{nd}}$ order for intensities in the range ≈ 7 GW/cm^2 to ≈ 20 GW/cm^2. Above this the order drops further due to ablation of the sample. Below ≈ 7 GW/cm^2 the order dependency is clearly very different to optical rectification which has a second order power dependence.

Ultrafast photo emission has been observed to have a similar intensity dependency to optical rectification [96]. The photocurrent exhibited by a flat silver surface excited in the Kretschmann geometry, as discussed in section 2.1.3, exhibits an intensity dependency which is $\approx 3^{\text{rd}}$ order for intensities < 4 GW/cm^2 to $\approx 1.5^{\text{th}}$ order for intensities > 8 GW/cm^2 [118], suggesting a link between photoemission and the generated terahertz. This is also supported by Welsh et al. [102], where the order parameter, the exponent of the power dependence, for generation is measured to vary from 5.0 to 3.5 on increasing the intensity of photoexcitation of a one dimensional diffraction grating.

4.4.2.1 Simple model

In an attempt to aid understanding of the measured incident intensity/generated intensity dependency, a simple model has been developed. It is expected that the radiated

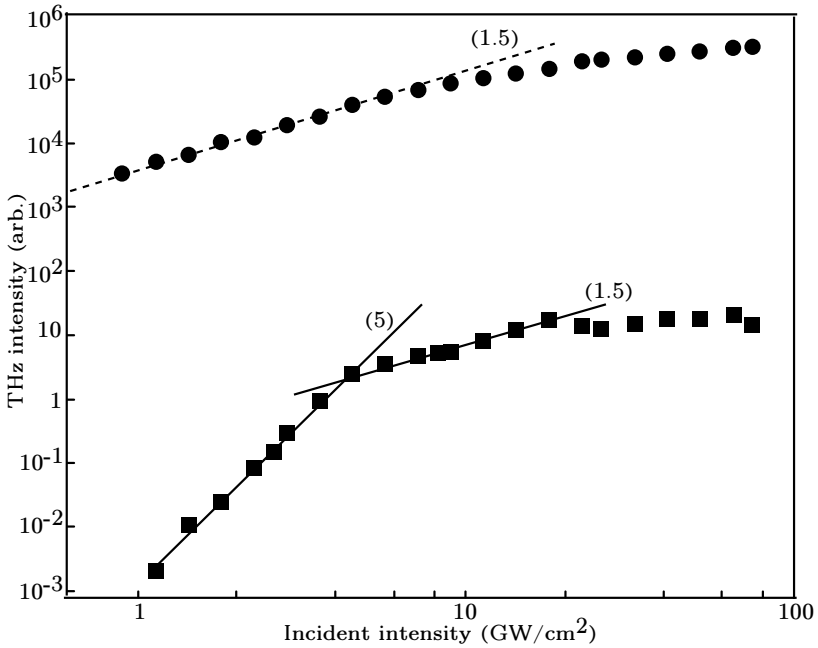

Figure 4.13: Dependence of generated terahertz fluence as a function of the intensity of the optical pulse incident onto the sample. ZnTe is shown as the circles and dashed line, with the squares and solid lines representing measurements of a NSL fabricated array, using spheres of diameter 780 nm and with a particle thickness of 50 nm.

terahertz field will be proportional to the product of the number (N) of emitted photoelectrons and their acceleration (a), assuming that the generated terahertz field is directly proportional to the photocurrent, then

$$E_{THz} \approx N(I_{opt}) \times a(I_{opt}) \tag{4.2}$$

where I_{opt} is the intensity of the incident optical pulse. The main concern in this simple analysis is the order dependence, which for the first term in eqn. 4.2 can be expressed as

$$N(I_{opt}) \approx I_{opt}^{n_1} \tag{4.3}$$

where n_1 is the order parameter, the exponent of the power dependence, of the multi-photon excitation, the number of 800 nm (1.55 eV) photons required to overcome the work function of the material (A). The work function is the energy required to remove an electron from the surface, for silver, $A = 4.3$eV, but has been shown to vary with sample morphology [119, 120]. There are known to be two different regimes for n_1, which can be quantified by whether the Keldysh parameter (γ) is above or below one

[121]. This is defined as

$$\gamma = \frac{\omega(mA)^{\frac{1}{2}}}{eE_{sp}} \tag{4.4}$$

where ω is the angular frequency of the incident pulse, m is the electron mass, e is the electron charge and E_{sp} is the evanescent electric field strength associated with the plasmon. E_{sp} can be written as a function of the incident field (E_0),

$$E_{sp} = \eta E_0 \tag{4.5}$$

where η is the electric-field enhancement factor. The two regimes are dominated either by multiphoton ionisation ($\gamma >> 1$), where $n_1 = 3$, as three photons are required to provide the energy above the work function. Or tunnelling ionisation ($\gamma << 1$), where $n_1 = 1$, high fields of the order 1 V/nm are required for this. Considering the incident optical intensity to be

$$I_{opt} = \frac{c\epsilon_0 E_0^2}{2}, \tag{4.6}$$

and using (4.5) the intensity at $\gamma = 1$ can be found

$$I_{opt}^{mpe} = \frac{mAc\epsilon_0\omega^2}{2e^2\eta^2}. \tag{4.7}$$

It can therefore be said that as the incident intensity increases from $I_{opt} < I_{opt}^{mpe}$ to $I_{opt} > I_{opt}^{mpe}$ the order parameter should vary from $n_1 = 3$ to $n_1 = 1$, with a transition in the region $I_{opt} = I_{opt}^{mpe}$.

The second term of (4.2) is also a function of the incident intensity and can be expressed in the form

$$a(I_{opt}) \approx I_{opt}^{n_2}, \tag{4.8}$$

where a second order parameter (n_2) is used. This order parameter can be estimated by considering the ponderomotive force arising from the strong field confinements around the particles (shown in fig. 4.9), these are evanescently decaying, with a decay length α. It is clear from fig. 4.9 that a full analysis of the ponderomotive forces is not trivial and therefore the system is simplified such that the plasmonic field is considered uniform in the plane of the substrate. The ponderomotive potential then takes the form [103]

$$U_{pon}(z) = U_0 \exp\left(\frac{-2z}{\alpha}\right), \tag{4.9a}$$

where

$$U_0 = \frac{e^2 E_{sp}^2}{4m\omega^2}, \tag{4.9b}$$

thus

$$U_{pon}(z) = \frac{e^2 E_{sp}^2}{4m\omega^2} \exp\left(\frac{-2z}{\alpha}\right). \tag{4.9c}$$

In addition the analysis is simplified further by ignoring the change in the incident intensity across the pulse. This potential gives rise to a force and therefore an acceleration of photoelectrons, this ponderomotive force, (4.1), can also be written in the form

$$F_{pon} = \frac{-dU}{dz} = \frac{2U_0 \exp(\frac{-2z}{\alpha})}{\alpha}. \tag{4.10}$$

From which two regimes for the acceleration of photoelectrons can be seen. One, with low E_{sp}, with the ponderomotive force unsaturated, resulting in a uniform acceleration over the pulse duration ($\approx$ 100fs), of the form

$$a_0 = \frac{e^2 E_{sp}^2}{2m^2\omega^2}, \tag{4.11}$$

over distances $a_0\tau^2/2 << \alpha$ where τ is the decay time. Using this with (4.5) and (4.6) a maximum intensity for this regime can be found

$$I_{opt}^{pon} = \frac{m^2 c\epsilon_0 \omega^2 \alpha^2}{\tau^2 e^2 \eta^2} = I_{opt}^{mpe} \frac{2m\alpha^2}{A\tau^2}. \tag{4.12}$$

Above this intensity is a region of non-uniform acceleration of the photoelectrons. Thus (4.12) is the transition intensity from $n_2 = 1$ to $n_2 = 0$.

From (4.2), it can be inferred that the total order parameter is

$$n_3 = n_1 + n_2 \tag{4.13}$$

for the electric field strength, it should be noted that the order parameter for intensity will be double this, as the generated intensity is proportional to the square of the electric field

$$\begin{aligned} n_4 &= 2n_3 \\ &= 2(n_1 + n_2). \end{aligned} \tag{4.14}$$

From the modelling presented above the decay length (α) and field enhancement factor (η) can be estimated to be 20 nm and 50, respectively, these are consistent with those found in the literature [116, 122]. Leading to two transition intensities

$$I_{opt}^{mpe} \approx 8 \text{ GW/cm}^2 \tag{4.15a}$$

and

$$I_{opt}^{pon} \approx 1 \text{ GW/cm}^2. \tag{4.15b}$$

As there are two transition intensities there will be three different regimes of order parameter. The lowest intensity regime ($I_{opt} < 1$ GW/cm^2), has both an unsaturated ponderomotive force ($n_2 = 1$) and photoemission by the multiphoton emission process ($n_1 = 3$), therefore $n_4 = 8$. For higher intensities (1 GW/cm^2 $< I_{opt} <$ 8 GW/cm^2) a second regime exists, where the ponderomotive force is partially saturated ($n_2 < 1$), although there is still multiphoton photoemission ($n_1 = 3$), therefore $6 < n_4 < 8$. In the third regime, with high intensities, $I_{opt} > 8$ GW/cm^2, this simple model predicts $n_4 = 2$, as the ponderomotive force is saturated ($n_2 = 0$) and photoemission is dominated by tunnelling ionisation ($n_1 = 1$).

It should be remembered that this is a greatly simplified model, and that there will be some influence on the electron trajectories from local surface roughness [106], and any modifications to the work function [120].

The lowest intensity regime ($n_4 = 8$), is not measured in fig. 4.13, this can be explained, as in the low intensity regime low-noise data cannot be obtained. This unsaturated ponderomotive force, multiphoton ionisation regime is therefore not available using the apparatus. The other two regimes are within the intensity range of low-noise date for the spectrometer, and can be identified in fig. 4.13, with the transition intensity of ≈ 7 GW/cm^2, close to that predicted by the simple model, ≈ 8 GW/cm^2. This strongly implies that the photoemission of electrons and their subsequent acceleration due to the ultrafast laser pulse are responsible for the observed terahertz generation.

4.4.3 Angle dependence

So far the discussion of generated terahertz radiation has been primarily around individual particles, and not the effect of the array (although this was included in the numerical modelling). The measured far field terahertz radiation will be a sum of the terahertz generation from each particle. It is apparent from fig. 4.4 that as the array is has rotational symmetry around the centre of where the spheres were arranged, any fields generated in the plane of the substrate will therefore be cancelled. The substrate creates an antisymmetric system in the z direction, although, as there is no phase retardation across the sample at normal incidence no terahertz radiation is expected. A qualitative understanding of any angle dependence on the terahertz generation can be gained by first considering that as the polar angle (θ) increases, so the out of plane component of the ponderomotive current capable of contributing to the far field terahertz signal will change with $\sin(\theta)$. A second effect will also be apparent, as θ increases as does the cross sectional area of the generating optical beam, reducing the effective

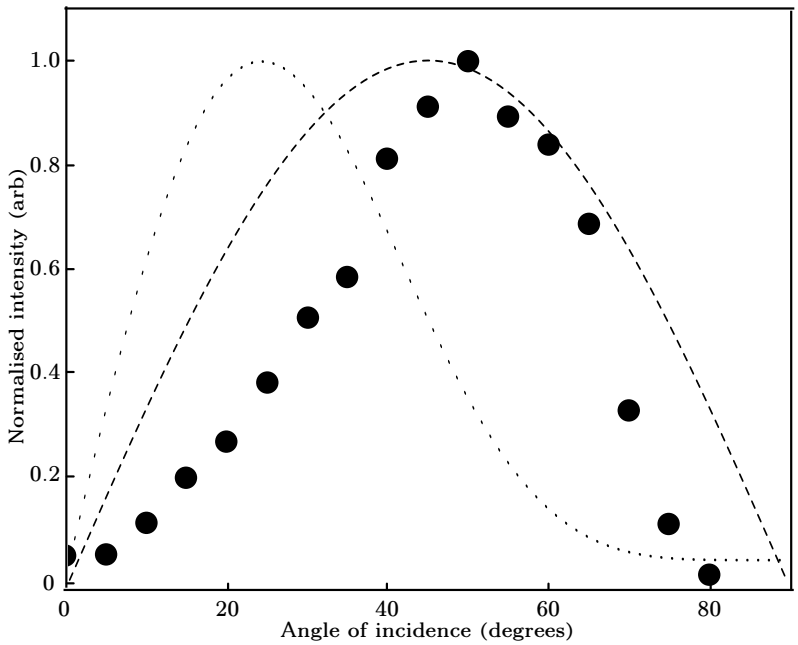

Figure 4.14: Measured angle dependence of the generated terahertz intensity, from an array of 50 nm thick triangles fabricated using NSL with spheres of diameter 780 nm. Also shown are two predictions from (4.16) where $n_4 = 1$ (the dashed line) and $n_4 = 5$ (the doted line).

intensity, this scales by $\cos^{n_4}(\theta)$, giving an overall intensity dependence of

$$\cos^{n_4}(\theta) \times \sin(\theta). \tag{4.16}$$

Fig. 4.14 shows the measured angle dependence of the generated terahertz intensity, from an array of 50 nm thick triangles fabricated using NSL with spheres of diameter 780 nm, a clear peak away from normal is observed, as predicted by (4.16). Also shown are two predictions from (4.16) where $n_4 = 1$ (the dashed line) and $n_4 = 5$ (the doted line). The difference can be accounted for as (4.16) takes very few physical effects into account. It is important to note that the angle dependence is not due to a shift in the plasmon resonance, which is shown to be minimal by rough modelling. The experimental angle dependence shows an unexpected signal at normal incidence ($\theta = 0$), this can be explained by inhomogeneities in the arrays, and/or the finite size of the excitation beam allowing some generation fields to be antisymmetric in the sample plane.

4.5 Conclusions and future proposals

Terahertz radiation has been measured from arrays of nanoscale particles, with an efficiency per unit volume approximately 200 times greater than that of ZnTe. A simple model for the generation has been developed, supporting the proposition that the generation depends upon the plasmon modes of the system both exciting and accelerating electrons. The model developed is more consistent with the measured power dependency than the optical rectification explanation proposed by others in the literature. It is feasible that the overall efficiency of generation could be increased using a 3D structure, with generation throughout. At the time of writing some low temperature (10 K) measurements of islandised films indicate that the emission of terahertz radiation may be slightly larger than that for ZnTe with an ≈ 100 fold increase in the detected signal.

An interesting future research area is that of arrays which are not centrosymmetric, inducing some generation from the in-plane plasmon fields, which would no longer cancel in the far field. This would again add support to the plasmonic fields of these nanostructured surfaces being the main contributor to the process of generating terahertz radiation. As the proposed effect depends on the emission and subsequent acceleration of electrons changing the surrounding medium should alter the detected signal. It has therefore been proposed to conduct generation experiments at varying pressures. These further experiments will allow the roles of electron emission and optical rectification to be ascertained.

Chapter 5

Terahertz plasmonic materials

In chapter 2 optical plasmons were discussed, it was shown that metals are required to support surface plasmons at these frequencies. Also previously in this thesis the far reaching applications of plasmonics was touched upon including new areas of interest such as the generation of terahertz radiation discussed in chapter 4. At optical frequencies it is known that some plasmonic materials support very strong and sharp surface plasmon modes whilst others produce weak broad modes. Here the material properties in the Drude model are used to differentiate between 'good' (sharp modes) and 'poor' (broad modes) plasmonic metals. It is thought that the understanding and practical uses of surface and particle plasmons might be extended by study in the terahertz regime.

To fully exploit the terahertz frequency regime the knowledge gained from considering which materials support surface plasmons at optical frequencies is extended into the terahertz regime. This will allow for comparisons between materials with similar parameters. The Drude parameters are measured for three different materials, and comparisons made. To support the conclusions, finite difference time domain (FDTD) modelling has been conducted using different Drude parameters. As semiconductors are found to support terahertz surface plasmons, the changeable carrier concentrations may also be exploited. Therefore, low temperature measurements of the Drude parameters are also discussed with some initial findings for the photoexcitation dynamics of InSb.

5.1 Drude parameters of optical plasmonic metals

The Drude permittivity is derived and used to find the surface plasmon frequency in chapter 2, (2.26) where it was shown to depend on ω_p is the plasma frequency, ϵ_l is the response of the ionic lattice, which is frequency independent (for metals at optical

frequencies $\epsilon_l = 1$) and γ is the scattering rate. The condition that this relationship comes from, $\epsilon_m + \epsilon_d = 0$, appears to not be satisfied for any real material where there will be an imaginary part of the metal permittivity. It can be shown from (2.12a) and (2.12b), the real and imaginary parts of the complex dispersion that a similar condition can be formed, $\epsilon'_m = -\epsilon_d - \epsilon''_m$. For most materials the simplified condition is a sufficient approximation.

Consider the two optical plasmonic metals, silver with $\omega_p = 1.2 \times 10^{16}$ rad/s, and $\gamma = 9.11 \times 10^{13}$ rad/s and aluminium with $\omega_p = 2.3 \times 10^{16}$ rad/s, and $\gamma = 9.11 \times 10^{14}$ rad/s [27, 38, 123]. These have surface plasmon frequencies of $\omega_{sp} = 8.48 \times 10^{15}$ rad/s and 16.2×10^{15} rad/s, respectively. Their corresponding imaginary parts of the permittivity are $\epsilon''_m = 0.021$ for silver and 0.112 for aluminium. From this it can be seen that despite their similar ω_p the dielectric loss tangent (ϵ''_m/ϵ'_m) is higher for aluminium than silver. Aluminium results in much broader surface plasmon resonances than silver and is considered a 'poorer' plasmonic metal than silver [124]. ϵ''_m depends only on γ therefore it can be said that a smaller γ is desired, the surface plasmon will be scattered less. It is clear that just minimising γ is not the only requirement for a good plasmonic material at the frequency range considered, but some balancing between γ and ω_p to produce the lowest loss, and ω_{sp} in the correct frequency regime must be conducted. Therefore, the parameters required for comparing the suitability of materials for plasmonic experiments are the surface plasmon frequency and the scattering rate.

5.2 Drude model and semiconductors

Terahertz frequencies are two orders of magnitude lower than optical frequencies. If the plasma frequency (ω_p) and scattering rate (γ) are scaled by a similar amount, it can be envisaged that the surface plasmon frequency (2.26) may also scale similarly. From this and

$$\gamma = \frac{e}{m^* \mu}, \tag{5.1}$$

where e is the carrier charge, m^* is the effective mass and μ is the mobility [38] it can be seen that the scaling might be achievable by changing the carrier concentration. Materials of this nature exist, semiconductors, but does the Drude model still work for semiconductors?

Fig. 5.1 shows schematic representations for the band structures of metals, semiconductors and insulators, where the shaded regions are filled electron states. This illustrates the differences between them. There are no filled electron states in the conduction band of semiconductors, with the Fermi level falling in the band gap. If the

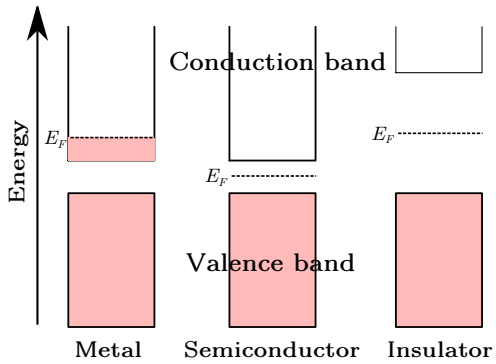

Figure 5.1: Schematic of idealised conduction and valence electron bands for metals, semiconductors and insulators. The Fermi level is indicated by E_F, up to which the electron states are filled.

band gap is narrow, electrons within k_BT of the conduction band will be excited from the valence band, resulting in a temperature dependent carrier concentration [38]. If the band gap is large then there will be no conduction band electrons and the material will be an insulator.

Semiconductors cover a very broad range of materials, with room temperature conductivities from 10^4 to 10^{-7} S/m [38]. These have varying band gaps, band energy dispersions, and Fermi levels. Recall from 2.2 that changing the band structure alters the effective mass of the material. It is not sufficient to just consider the carrier concentrations of the materials as equations (2.23) and (5.1) also depend upon the effective mass.

As discussed in section 2.2 the conduction band electrons are the important charge carriers in the Drude model. For metals, interband transitions (transitions where electrons move between bands) can occur for frequencies around the plasma frequency, this manifests in a contribution to ϵ_m'' [125]. For semiconductors, frequencies around the plasma frequency do not have the energy for these transitions, *intra*band transitions (where electrons change to different states within the same band) are therefore of more importance. It should be noted that for these intraband transitions to conserve momentum and energy, scattering from a phonon or impurity is required [125]. Conduction band electrons are therefore still important as there are many available energy levels.

Another difference between semiconductors and metals is the non-unity ϵ_l. For semiconductors below the optical phonon frequencies this is the permittivity associated with the polarisability of the ionic lattice and is therefore close to the static permittivity without free carriers. From the above the Drude model should apply to semiconductors, with the proviso that there are no phonon modes within the frequency range considered [38].

Semiconductors are unusual in that their carrier concentration and therefore permittivity can change. As previously mentioned, temperature will alter the carrier concentration, it can also be modified by photoexcitation and doping [125]. To photoexcite an electron it needs to absorb a photon with an energy above the band gap of the semiconductor, exciting it from the valence band to the conduction band, this is normally done using an optical pump pulse. Doping adds a small concentration of impurities (a different element) into the crystal, which leads to an increase in the number of free electrons or holes available in the semiconductor. Increasing the carrier density increases the scattering rate. This is due to two different scattering mechanisms, electron-defect scattering which is mostly important for doped semiconductors, and electron-hole scattering which is mostly important for photoexcited semiconductors. The former is in part due to the increase in the dopant ion cores within the semiconductor which act as scattering centres. It should be noted that for a more complete analysis polarons should be discussed, but the semiconductor of most interest, InSb, has a very low Fröhlich coupling constant of 0.014, they can therefore be ignored [38]. This means that there is little interaction between photons and optical phonons.

5.3 Terahertz plasmonic materials

Previous work on terahertz plasmonics using semiconductors includes investigations of gratings [126–128], planar surfaces [36], slits [129–131], and particles [132]. These have mostly used doped silicon (Si) or undoped indium antimonide (InSb), the material parameters of these are discussed below. It was thought an interesting investigation to compare the merits of these and other similar materials. To conduct this investigation it is required to have some method for measuring the Drude parameters for semiconductors.

5.3.1 Measuring the Drude parameters

The transmission through a slab of material, as shown in fig. 5.2, can be analytically evaluated by considering the Fresnel coefficients

$$t_{a,b} = \frac{2n_a \cos\theta_a}{n_a \cos\theta_a + n_b \cos\theta_b}, \tag{5.2a}$$

$$r_{a,b} = \frac{n_a \cos\theta_a - n_b \cos\theta_b}{n_a \cos\theta_a + n_b \cos\theta_b}, \tag{5.2b}$$

for the two interfaces shown in fig. 5.2 ($a = 1$, $b = 2$, and $a = 2$, $b = 3$). Where n, and θ are the refractive index and the angle from normal incidence in their associated

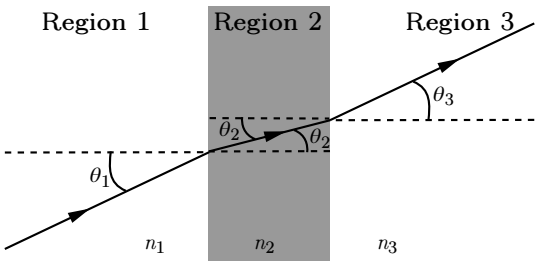

Figure 5.2: Schematic of the transmission through a slab of material with refractive index n_2.

material, respectively. The Fresnel coefficients for s-polarised light are used here, a similar analysis can be conducted for p-polarised radiation [78]. The contributions to the transmission from each interface are summed up using a phase shift [78]

$$\beta = 2d\frac{\omega}{c}n_2 \cos\theta_2, \tag{5.3}$$

where d is the thickness of the slab, ω is the angular frequency of the incident radiation, c is the speed of light, n_2 is the refractive index of the slab and θ_2 is the angle of incidence inside the slab from Snell's law [78]. This yields a transmission coefficient of

$$t = \frac{t_{1,2}t_{2,3}e^{((1/2)i\beta)}}{1 + r_{1,2}r_{2,3}e^{(i\beta)}}. \tag{5.4}$$

A similar approach can be used to find the reflection coeficient

$$r = \frac{r_{1,2} + r_{2,3}(t_{1,2}t_{2,1} - r_{1,2}r_{2,1})e^{i\beta}}{1 - r_{2,1}r_{2,3}e^{i\beta}}. \tag{5.5}$$

If the thickness and the complex transmission or reflection coefficient is known these can be solved iteratively to find the complex refractive index for the slab.

The THz-TDS systems discussed above in 3.1 measure the full electric field profile of the terahertz pulse. If the reflection or transmission from a sample is normalised against a perfect mirror or free space measurement, respectively, the three layer Fresnel coefficients can be found.

From the previous terahertz plasmonics work in the literature doped silicon and undoped InSb have been used. It was thought appropriate to therefore analyse these materials. Initial trials trying to observe the transmission through an InSb wafer (450 µm thick) showed no measurable transmission. Efforts were therefore made to conduct reflection experiments using the collimated set up with an InSb wafer with one side coated in 100 nm of silver to act as the reference. To maintain a reliable measurement

of the phase of the reflection coefficient the reference needed to be less than ≈ 5 µm from the position of the sample. Using an optically flat silicon wafer to rest the sample on improved the repeatability but a shift in time for repeats of the reference around the temporal resolution of the scan (0.05 ps, ≈ 15 µm) were still observed. A wafer was then thinned down to ≈ 130 µm thickness using a nitric acid wet etch, this process is discussed in greater depth in chapter 6. Transmission was observed through the sample using the focusing spectrometer. The two silicon samples were both observed to have a measurable transmission without any thinning required.

It is desired to find the Drude parameters from the Drude permittivity

$$\epsilon_m(\omega) = \epsilon_l - \frac{\omega_p^2}{\omega^2 + i\omega\gamma}, \tag{2.25}$$

for the measured materials. There are two fitting methods that can be used. The refractive indices can be found iteratively from (5.4) and the Drude permittivity square rooted and fitted to this. The alternative being using the refractive indices from the Drude permittivity to form a complex transmission spectrum and this fitted to the measured transmission. The difficulty with using the first method is when the thickness (d) is not well known both the measured refractive indices and the calculated refractive indices have some movement as (5.4) depends on d. The minimisation algorithms used are very unstable in situations where this occurs as the solution surface in the parameter space becomes very rough, local minima are therefore found more often than the true solution to the system if it will converge at all. It was therefore decided to use the second method where the squared difference between the calculated transmission spectra and the known spectrum of coefficients is minimised using a Davidon-Fletcher-Powell optimisation algorithm [133], fitting ω_p, γ, and d.

5.3.2 Results

Two differently n-doped silicon samples were available for testing with room temperature resistivities of $2 < \rho < 4$ Ωcm for sample a and $\rho = 1$ Ωcm for sample b. The thicknesses of the samples are $d = 200$ µm and 300 µm, for sample a and sample b respectively. Fig. 5.3 shows the measured (unfilled circles for sample a and unfilled diamonds for sample b) and fitted (solid lines for sample a and dashed lines for sample b) real and imaginary parts of the transmission at room temperature through the two silicon samples. It can be seen that the fits to these are good. This is in part due to the high transmission through the samples. The Drude parameters from fitting are found to be $\omega_p = 2.08 \pm 0.15$ THz, $\gamma = 3.06 \pm 0.4$ THz and $\omega_p = 12.4 \pm 0.19$ THz, $\gamma = 11.1 \pm 0.7$ THz respectively. The larger scattering rate is expected for the more

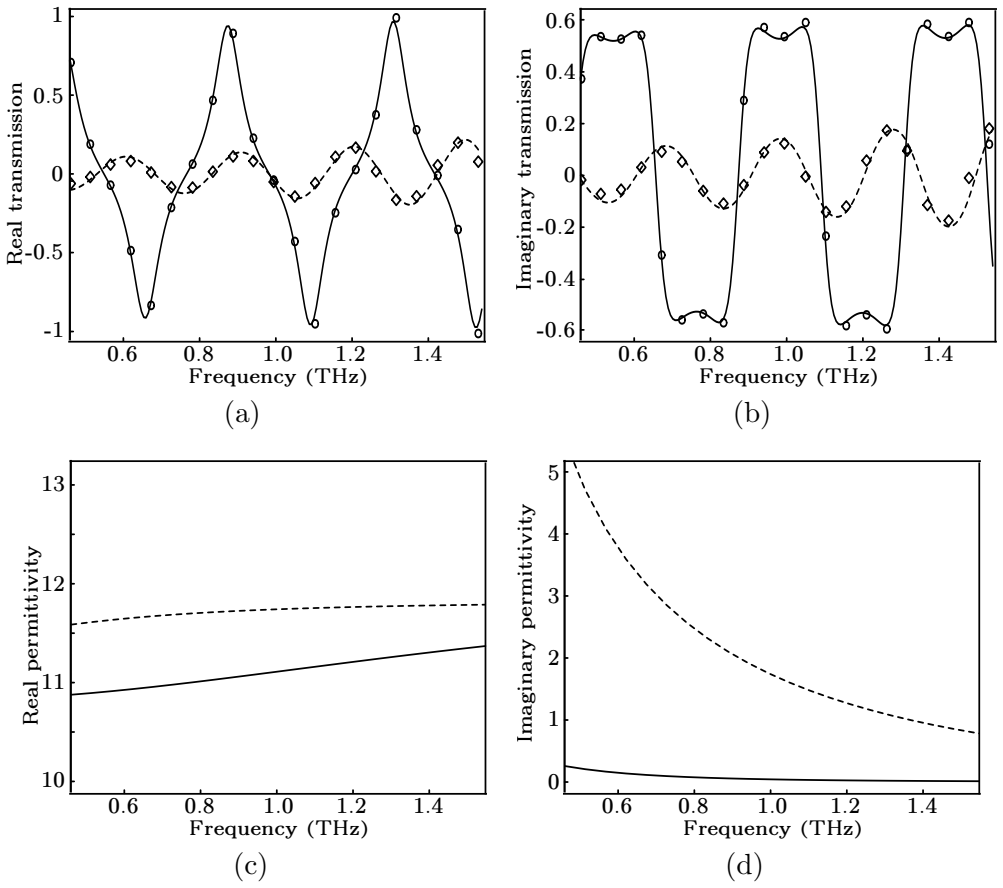

Figure 5.3: (a) Real and (b) imaginary parts of the transmission of the two silicon samples in the frequency domain. Also shown is the (c) real and (d) imaginary parts of the permittivity found from the fitting parameters. The experimental results are show as symbols and the lines are the fits. Sample a is shown as the circles and solid lines and sample b as the diamonds and dashed lines.

doped sample as doping adds scattering centres to the crystal. Applying (2.26) produces imaginary frequencies for both materials. They therefore do not support surface plasmons. This conclusion is supported by extrapolating the permittivity shown in figs. 5.3(c) for the real part and 5.3(d) for the imaginary part using the Drude model to cover a very large frequency range. If this is done then it can be seen that ϵ' is always positive. A simple condition can be formed to show which materials this occurs for, consider (2.26), if

$$\gamma^2 > \frac{\omega_p^2}{1+\epsilon_l}, \tag{5.6}$$

then the surface plasmon frequency is purely imaginary and does not support a surface plasmon resonance.

The measured time domain trace and the real and imaginary parts of the transmission coefficient for InSb are shown in fig. 5.4. In the frequency domain, the symbols are the measured data and solid lines are the fitted model. The oscillation that can be seen between 1.4 THz and 1.6 THz is due to the Fourier transform of a discontinuous noise signal with a length of 20 ps, this transmission looks similar to that measured in [134]. The earliest oscillations (between 1.5 THz and 1.7 THz) being due to noise is supported by finite difference time domain (FDTD) modelling. FDTD modelling was conducted using the Meep software package [135]. Briefly, this method works by splitting the model into a grid of space and time and solving Maxwell's equations as they evolve with time [135]. A simple 2D model was created with symmetry boundaries on the side and PMLs (similar to that described in section 3.4) on the ends. An incident plane wave pulse was used with a similar temporal shape to the terahertz pulses produced by the spectrometer. The model contained a single 130 μm thick slab of InSb using Drude parameters from [36]. A Gaussian noise distribution was added to the transmitted modelled time domain pulse. Analysing this in the same way as the experimental data results in similar oscillations before the Drude like increase of transmission. The fitting code will not converge on a solution that includes these oscillations. The fitted parameters to the measured transmission are $\omega_p = 45.87 \pm 0.01 \times 10^{12}$ rad/s, $\gamma = 0.692 \pm 0.008 \times 10^{12}$ rad/s, and $d = 125 \pm 0.5$ μm where $\epsilon_l = 15.56$ was set in the model. These agree well with previous non-direct measurements where the Drude parameters were fitted from transmission through slits in InSb mediated by surface plasmons measured by Isaac et al. [129]. From this it can be shown that $\omega_{sp} = 11.2 \times 10^{12}$ rad/s. The permittivity found from these fitted parameters is shown in fig. 5.4(d). The inset shows that the real part of the permittivity crosses -1 at ≈ 1.78 THz which is in the range of interest.

5.3.2.1 Temperature dependence

The carrier concentration can be decreased by cooling the sample. This effect on the Drude parameters is discussed here. This has been investigated by using a continuous flow Helium cryostat, allowing temperature control of the InSb sample between 6 K and room temperature (RT). The windows of the cryostat are quartz, minimising absorption of the terahertz radiation. Despite this, the higher frequency components are absorbed by the windows. The absorption is probably due to water impurities. Higher temperature (close to RT) measurements cannot therefore be conducted as the cut off of transmission increases in frequency with temperature.

Complex transmission spectra have been measured for InSb at different temperatures, 10K, 50K, 100K, 150K and room temperature. In the frequency domain these have been normalised against a straight through measurement of the cryostat. Where

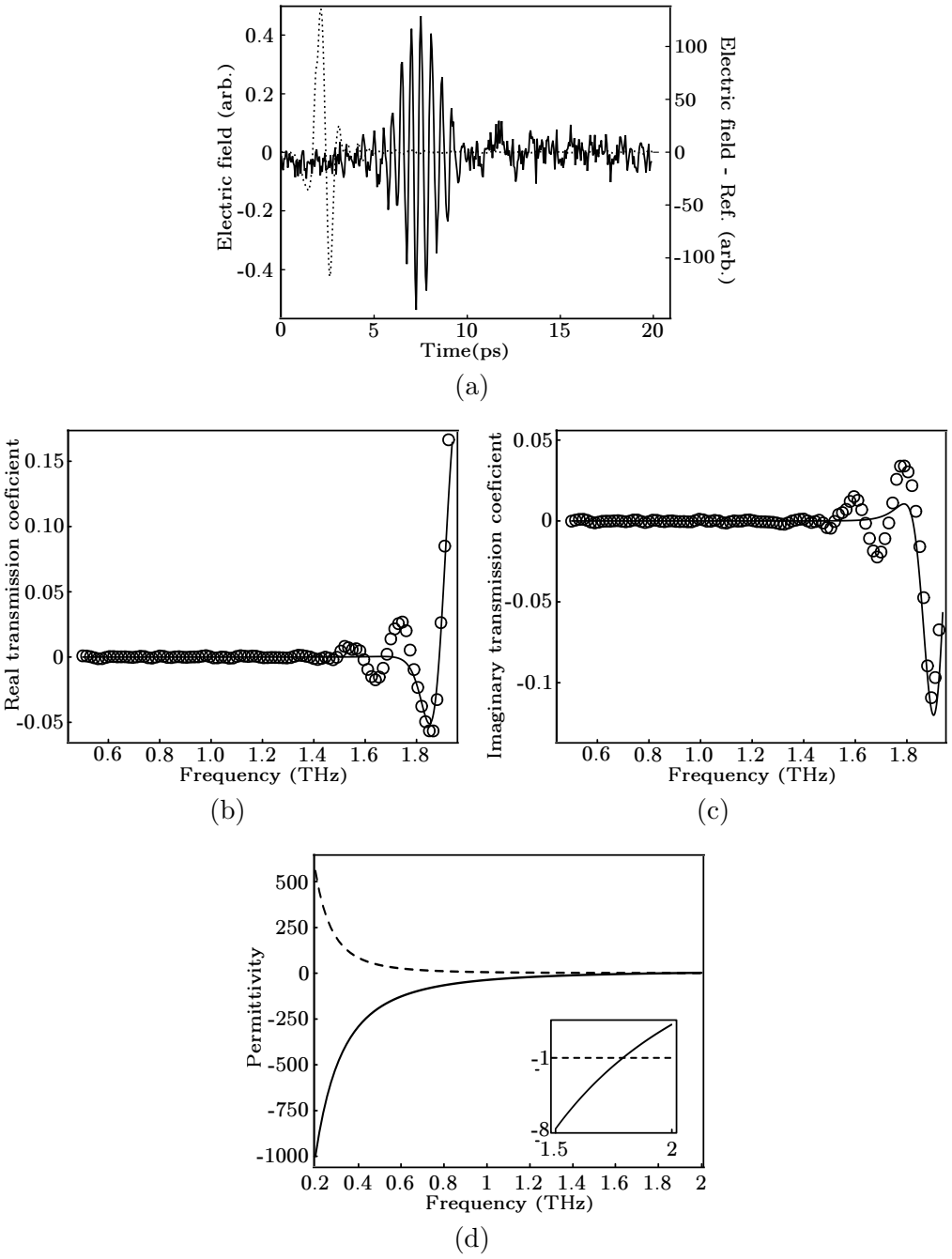

Figure 5.4: (a) Time domain and (b) real and (c) imaginary parts of the Fourier transformed frequency domain of the transmission through InSb sample at room temperature. The time domain results are only experimental. In the frequency domain the experimental results are represented as a symbol for every 75^{th} data point and the lines are the fits. (d) Shows the permittivity from the fitted Drude parameters, the solid line is the real part and the dashed imaginary. The inset shows where the real permittivity crosses -1 (shown as the dashed straight line).

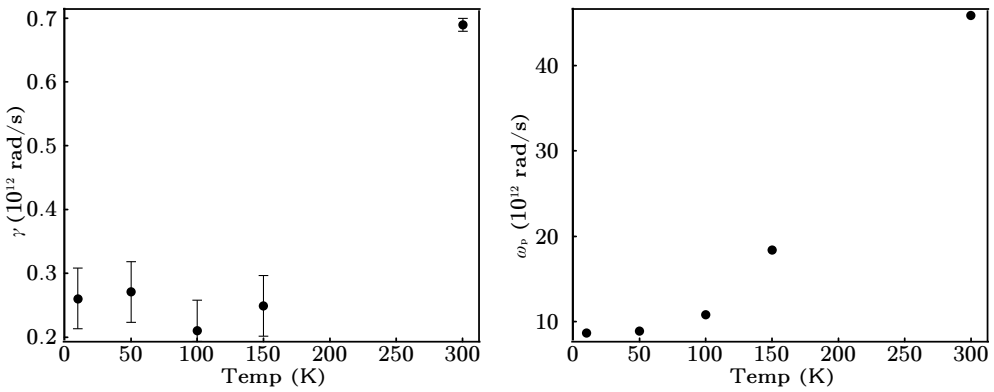

Figure 5.5: The extracted (a) scattering rate and (b) plasma frequency from the InSb sample at various temperatures.

the cryostat is raised ≈ 1 cm above the normal position allowing the terahertz beam to pass under the sample but through the cryostat. These normalised spectra have again been fitted to allow ω_p and γ to be extracted using the method described above, these results are shown in fig. 5.5. As the temperature decreases the number of filled states in the conduction band decreases. As there are fewer free carriers there is a reduced interaction with the terahertz radiation, the transmission increases. This is supported by the measurements, with a decreasing plasma frequency. The scattering at low temperature is below the room temperature measurement. This effect is expected as impurity scattering does not vary with temperature but should not be very large as the InSb is an undoped intrinsic semiconductor although the saturation at low temperatures of ω_p indicates the system is not completely undoped. The doping is possibly due to the etching process. Other contributions to the scattering increase with temperature [38]. The scattering in InSb is dominated by electron phonon scattering. The temperature dependence of these scattering events is controlled by the Debye temperature. For InSb this is 200 K [136]. Below the Debye temperature some phonon modes of the crystal cannot be supported, their contribution to the scattering therefore reduces. These results are discussed further in the next section, where the low temperature measurements are shown compared to other semiconductors, their lower plasma frequency (and therefore lower surface plasmon frequency) can be seen. Due to the absorption of the terahertz signal at high temperatures there is a gap in the temperature results between room temperature and the temperature at which no measurable signal can be observed.

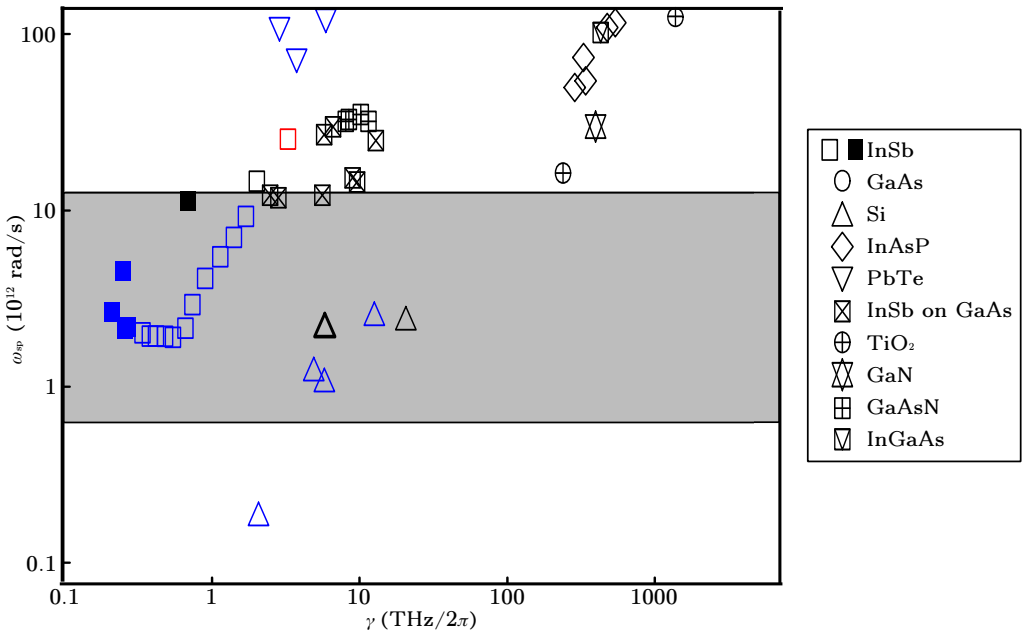

Figure 5.6: A log log plot of the surface plasmon frequency (ω_{sp}) plotted against the scattering rate (γ) for different semiconductors found in the literature (open shapes) and measured in this paper (filled shapes). The black data points represent room temperature measurements, red ones are above room temperature and blue below. It is discussed in the text that ω_{sp} needs to be in the range of typical terahertz time domain spectrometers (0.2 $\rightarrow$ 2 THz, the shaded region) with γ as low as possible. It can therefore be said that InSb is the best candidate for terahertz plasmonic experiments. The bold silicon result is used below for modelling.

5.3.3 Comparison between semiconductors

There has been significant previous work on measuring the material parameters of semiconductors using various techniques including spectroscopic ellipsometry [137], and reflection THz-TDS [138]. Fig. 5.6 shows (unfilled shapes) the surface plasmon frequency against the scattering rate for a range of different semiconductors, some having their carrier concentrations modified by doping [139], photoexcitation [140], heat treatment [141] or cooling [142]. These values have been calculated from measurements found in the literature; red symbols indicate above room temperature measurements and blue symbols those below room temperature. The shaded area is the region over which a typical terahertz time domain spectrometer operates (0.2 $\rightarrow$ 2 THz).

The low temperature silicon results are taken from [143] with n-doped room temperature results from [144] and [145]. The resistivities for these samples were all in the range $\rho = 0.1$ Ωcm. This shows that suitably doped silicon can be used for terahertz plasmonics, unlike the two doped silicon samples measured in this project. GaAs also

has some data points in the shaded region of interest, with different doped samples shown from [146], [138], and [139].

Dixon and Riedl [141] provide measurements for PbTe where the carrier concentration is either changed by doping or heat treatment. Despite its low γ, the ω_{sp} is too high for terahertz plasmonics, although this material does look promising for work at higher frequencies. The two TiO_2 measurements are photoexcited and taken from [140], whereas the single GaN in the range of the graph is from [147].

For more complicated semiconductors the ratio of the constituent elements can be altered such as the ratio of As to P in InAsP or As to N in InAsN, which were both measured in [148] or As to N in GaAsN measured in [137]. These three semiconductors all have ω_{sp} out of the spectrometer range.

InSb grown on GaAs was measured by Yang et al. [149] and indicates that this material might be suitable, with some data points falling on the edge of the region of interest. But the most obvious candidate shown on fig. 5.6 is InSb. Three sets of measurements are shown, the first [150] from 1964 and later results from 1996 [142]. These two results agree with each other. As the sample is cooled the scattering rate decreases with the surface plasmon frequency. The room temperature measurement from [150] produces a surface plasmon frequency that is outside the range of the spectrometer. This doesn't agree with the reports from the literature where terahertz plasmonics are conducted with slits in InSb [129]. Those and similar measurements produced surface plasmon frequencies in range of 1.8 THz [36, 129].

The third set of experimental InSb results presented are those measured in this project. At high temperatures these results do not agree with those from Howells and Schlie [142], this is likely due to improvements in crystal growth. The InSb results from [142] show that as the temperature increases the surface plasmon frequency is relatively stable before increasing, this can be seen from 2.26 as when $\frac{\omega_p^2}{1+\epsilon_l} >> \gamma^2$, ω_p dominates over γ. This behaviour is not reproduced with the measurements presented here, although the lowest temperature values do appear to agree. This is due to the relatively temperature independent gamma for all the low temperature measurements presented here. In this temperature range the only influence on the surface plasmon frequency is therefore the plasma frequency. InSb having a much lower scattering rate than the other semiconductors can in part be explained by InSb being an intrinsic semiconductor and therefore not having any dopant ion cores off which the electrons can scatter, as with the doped semiconductors [79]. A second contribution to the low scattering rate of InSb compared to other semiconductors is that the band gap is small (0.17 eV) resulting in a small effective mass for the electrons. Larger effective masses produce higher scattering rates as the there is therefore a larger density of states.

It should be noted that there are a great many measurements of Drude parameters

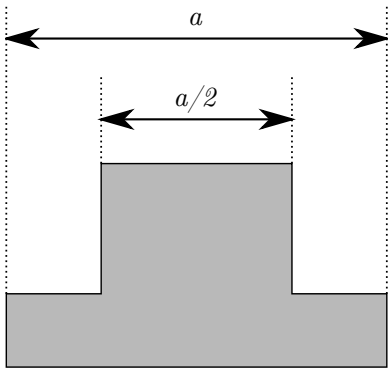

Figure 5.7: Schematic of the grating profile used for the finite difference time domain modelling.

for various semiconductors that yield an imaginary ω_{sp}. This includes differently doped samples from the references above, including doped silicon in [143], and GaAs in [139]. Also semiconductors such as AlGaAs [151], BiSb [152] and InN [153] could not be found in the literature with a real ω_{sp}. These semiconductors may not be capable of supporting surface plasmons in the terahertz frequency range.

5.3.3.1 Modelling of gratings with different semiconductors

To emphasize the important differences between different semiconductors with respects to plasmonics applications modelling using two different sets of Drude parameters has been conducted. In section 2.1.3 coupling to surface plasmons using gratings is briefly discussed. From there it can be inferred that the position of the observed surface plasmon resonance depends on the diffraction edge of the grating and the material parameters [27, 154]. The shape and position of the resonance depends not only on these but also on the profile of the grating [155, 156]. The effect of these have been studied in depth at optical frequencies [156] and recently at terahertz frequencies [126–128]. From this previous work it can be seen that to the first order the coupling efficiency depends upon the depth of the grating.

FDTD modelling has been conducted for square monogratings with a mark to space ratio of 50% as shown in fig. 5.7. The model was set up as described above, with a thicker substrate and the grating on the incident surface. This modelling has been conducted for two materials with various depths showing how the coupling efficiency changes. Fig. 5.8 shows the surface plasmon resonance and diffraction edge for InSb (fig. 5.8(a)) and doped silicon (fig. 5.8(b)). The oscillations are due to conducting a Fourier transform of a finite length time domain measurement. The permittivities are found using the Drude parameters found above for InSb at room temperature and

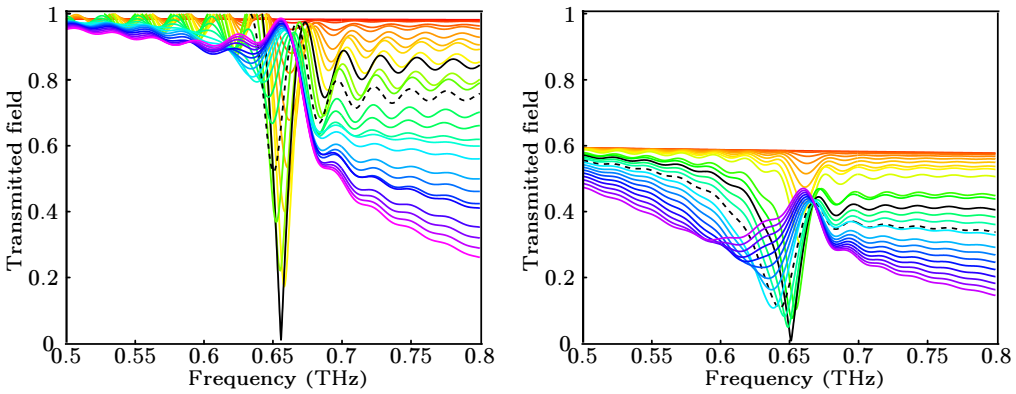

Figure 5.8: Finite difference time domain results for a monograting with a mark to space ratio of 50%. The depth of the grating is varied showing the changing coupling efficiency. The two panels are (a) InSb using the Drude parameters found above, and (b) silicon using Drude parameters from [145], indicated in fig. 5.6 by the bold symbol. The depth is shown by the changing colour, following the visible spectrum, from 0 μm deep to 75 μm deep for violet. The black solid lines are the optimally coupled modes, and the black dashed lines are the modes where the grating is 9 μm deeper than the optimally coupled depth.

for silicon from [145]. The silicon parameters used are $\omega_p = 21 \times 10^{12}$ rad/s and $\gamma = 4.5 \times 10^{12}$ rad/s these are shown on fig. 5.6 by the bold data point. Unlike the two silicon samples measured here, silicone with these parameters would support surface plasmons. The changing depth is shown by the changing colour, following the visible spectrum, from 0 μm deep for red to 75 μm deep for violet.

These figures show optimal coupling with the two solid black lines this occurs at 27 μm and 39 μm for InSb and silicon respectively. The wavelength at the surface plasmon resonance is 457.59 μm for InSb and 460 μm for silicon. These values are within the region expected by scaling the length scales from optical plasmon work [156]. It can be seen that despite the similar surface plasma frequency of these two materials, the silicon resonances are clearly broader in this model. This is most obvious for the deeper gratings which are over coupled as the under coupled and optimally coupled modes are tight to the diffraction edge, narrowing them. The two black dashed lines in fig. 5.8 are both 9 μm deeper than the optimally coupled depths. These two highlight the difference in width of the resonances for the two materials. The silicon resonances broaden more for the same change in depth of the grating, this is expected due to the higher scattering rate. The higher absorption of the silicon is also apparent by the reduced reflection from the sample.

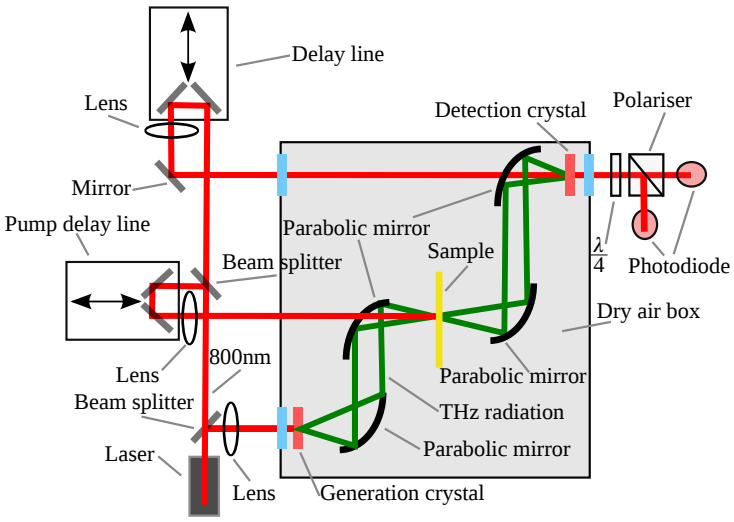

Figure 5.9: Schematic of the focusing terahertz spectrometer with a third path, allowing the sample to be optically pumped.

5.3.4 Photoexcitation of InSb

In chapter 6 it is proposed that high Q resonances of InSb devices could be highly sensitive to photoexcitation, providing very large photomodulations. Such devices could have practical applications [157]. It is therefore necessary to probe the photoexcitation dynamics of InSb to establish possible modulation and recovery rates.

To allow for photoexcitation of the sample a second beamsplitter is added to the system with a second delay line. This is shown in fig. 5.9, where it can be seen that the new optical path results in a pulse coincident on the sample with the terahertz pulse. The delay line allows the pump pulse to hit the sample at different times relative to the terahertz pulse, thus allowing the decay to be measured. The system used here is limited to a temporal range of 150 ps due to space limitations around the delay line.

As measured above, as the temperature decreases so will the carrier concentration, reducing the plasma frequency and increasing the transmission. On photoexcitation the carrier number will increase and the transmission drop. Fig. 5.10 shows a time domain transmission measurement of InSb at 10 K with no photoexcitation (solid line) and illuminated by a 400 nm pulse (dashed line). The expected qualitative reduction in transmission is observed. The small peak around 7 ps is due to some leakage of the terahertz around the outside of the cryostat, later experiments eliminate this. The effect of photoexcitation appears the same as heating the sample. There is a noticeable drop in signal.

Excluding fig. 5.10 all the measurements presented here use 800 nm (1.55 eV) excitation pulses. As the band gap of InSb is 0.17 eV [38, 158] each photon has a large

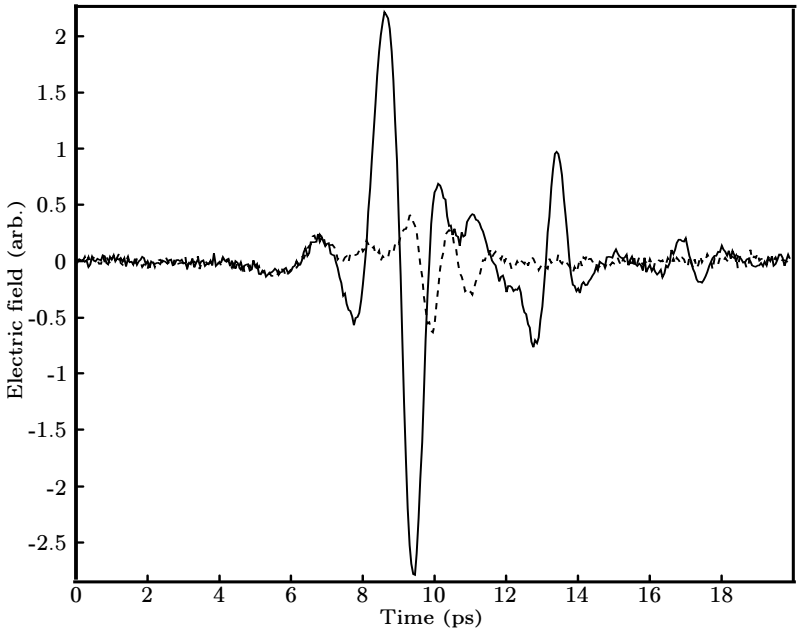

Figure 5.10: Time domain transmission measurement of InSb at 10 K with no photoexcitation (solid line) and illuminated by a 400 nm pulse (dashed line).

enough energy to overcome the band gap. For photoexcitation four pump powers have been used, *i* 0.56 mW/cm^2, *ii* 5.1 mW/cm^2, *iii* 16 mW/cm^2, and *iv* 611 mW/cm^2. The sample is again mounted inside the cryostat (reducing the pump powers by around 10%).

Fig. 5.11 shows two fluences, 5.11(a) *iii* and 5.11(b) *iv* at varying temperatures. Fig. 5.11(a) indicates that there is no consistent temperature dependence, although differences between them can be seen. The decay times are too long to fit to over the temporal range used here, although they do seem shorter than those reported for n-type InSb at 2 K using much longer excitation pulses [159]. This work in the literature reported two decay times, a 'short' decay of $\approx$ 60ns attributed to band to band decay and a 'long' one of 3.8 µs attributed to band to acceptor decay [159]. The decays observed here appear much shorter. There is a clear dependence of decay dynamics on both temperature and carrier density. The interplay between these two dependences can lead to some very complex dynamics, as discussed below. Fig. 5.11(b) appears more unusual. With the pump pulse blocked all three temperatures are consistently negative as at $t = 0$ in 5.11(a).

Each trace in fig. 5.11(b) is formed by averaging three separate measurements, fig. 5.12 shows the 3 averages separated out for the 100 K measurement. The solid line shows the first trace at the start of which the pump is uncovered. Between each trace the delay stage returns to its starting position and pauses for 1 min. The time constant

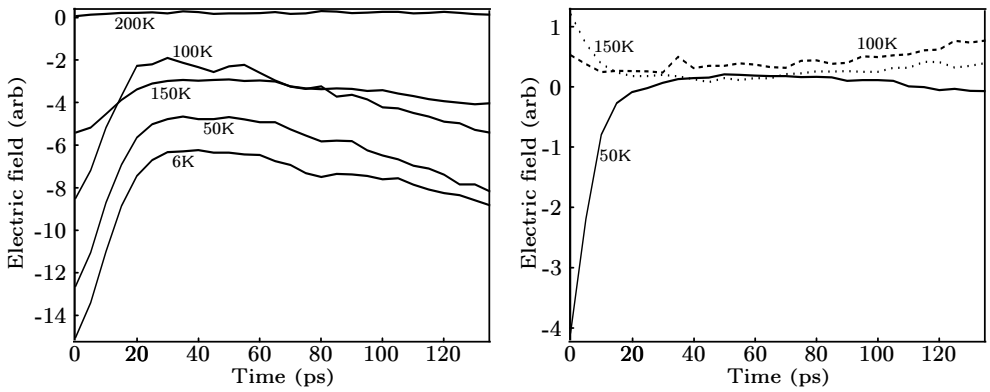

Figure 5.11: Decay of the induced reduction in the terahertz transmission with time from an optical photoexcitation pulse. Each sub figure shows various temperatures (indicated in the figure) for a single fluence. The fluences are described in the text where (a) shows *iii*, and (b) shows *iv*.

of the lock in amplifier was 3 s, with a 9.5 s delay between each data point reading along the delay line. For the first (dotted line) and second (dashed line) repeats there is a clear peak from an apparently stable signal with exponential time constants of 7.2 ps and 7.8 ps respectively. It is thought that this effect is not an artefact of the experiment as blocking the pump beam results in a return to the original signal.

To try and understand this unusual behaviour, consider fig. 5.13(a), where the filled electron states are shown for the valence and conduction bands, on excitation the largest change in carriers is from the valence band into the conduction band. These decay to the bottom of the conduction band as discussed below and are relatively stable. Some time later, fig. 5.13(b), a second excitation pulse hits. Most interactions are now with conduction band electrons, exciting them into higher energy states which decay before recombining with holes on longer timescales. This shows a very long delay time. It is unlikely that the radiative recombination time of a free electron-hole pair in InSb exceeds the 2ms repetition time of the pump pulse. It is therefore suggested that these quasi-steady state photoexcitation effects are likely due to sample heating as the fluence is very high [159, 160].

Fig. 5.14 shows two temperatures 50 K (fig. 5.14(a)) and 150 K (fig. 5.14(b)) for some different fluences. From these figures it can be seen that the dependence on density is complex; at low temperature (50K) decay rates appear to be longer at for high densities, while this is reversed at higher temperatures (150K). This complex behaviour is likely due to competing temperature dependent effects. For example, the faster recombination rates observed for higher densities in the high temperature

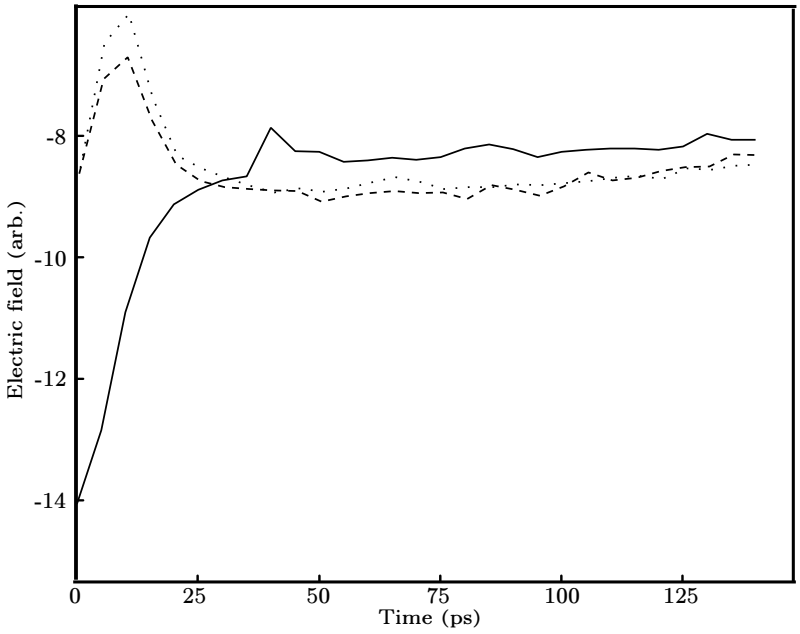

Figure 5.12: Three consecutive measurements of the photoexcitation decay using pump fluence *iv* at a temperature of 100 K. The first measurement is the solid line with the first repeat being the dotted line and the second the dashed one.

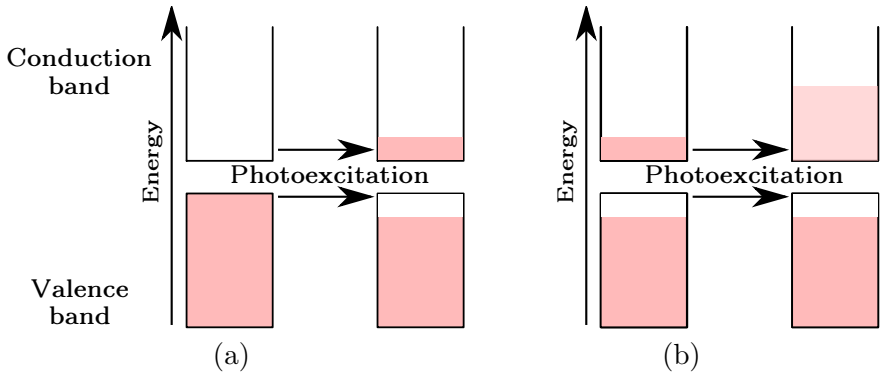

Figure 5.13: Schematic of the conduction and valence bands showing filled electron states as the system is photoexcited. (a) When the system starts without being photoexcited, and (b) where the system has already been photoexcited.

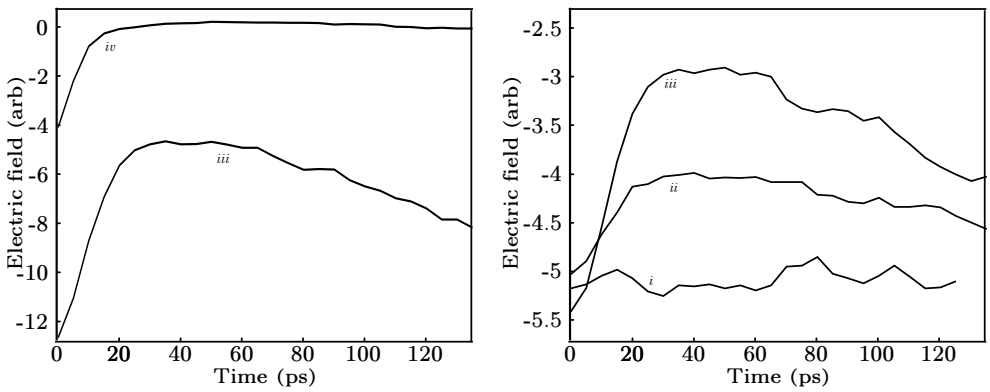

Figure 5.14: Decay of the induced reduction in the terahertz transmission with time from an optical photoexcitation pulse. Each sub figure shows various fluences (indicated in each figure) for a single temperature. The temperatures are (a) 50K, and (b) 150K.

regime are likely due to non-geminate recombination of electron-hole pairs. At low temperatures, it is possible that the finite thermal conductivity of the sample plays an important role, giving rise to steady state heating effects. The decay cannot be reliably fitted to an exponential.

One notable observation from this data is the long rise time. O'Neil et al. [161] shows slow rise times explained as an efficient thermal repopulation, similarly slow rise times of ≈ 7 ps are observed in Gupta et al. [162]. In fig. 5.15 a Gaussian is fitted to the graph with a full width half maximum of 27 ps this is ≈ 270 times greater than the optical pulse duration. A Gaussian was chosen as to produce an estimate of the rise time, no physical conclusions should be taken from this. This is likely due to the decay of very highly energetic electrons decaying to the more stable bottom of the conduction band after excitation. As the electrons decay they lose energy which can be to valence band electrons exciting them into the conduction band. This is known as impact excitation and is illustrated in fig. 5.16. The time scale over which impact ionisation is expected to occur is similar to that observed [160]. Impact ionisation has been previously observed in InSb [163]. Switching times for photomodulated devices will be limited by this slow rise time. The apparent slow decay time of the photoexcited state will also limit the switching times of any photomodulators based on InSb. From the measurements presented here, it appears that fast (GHz) photomodulation of crystaline InSb is not possible. The long timescales associated with photomodulation are certainly a drawback of this material.

It is clear from these measurements that the carrier dynamics of InSb can not be

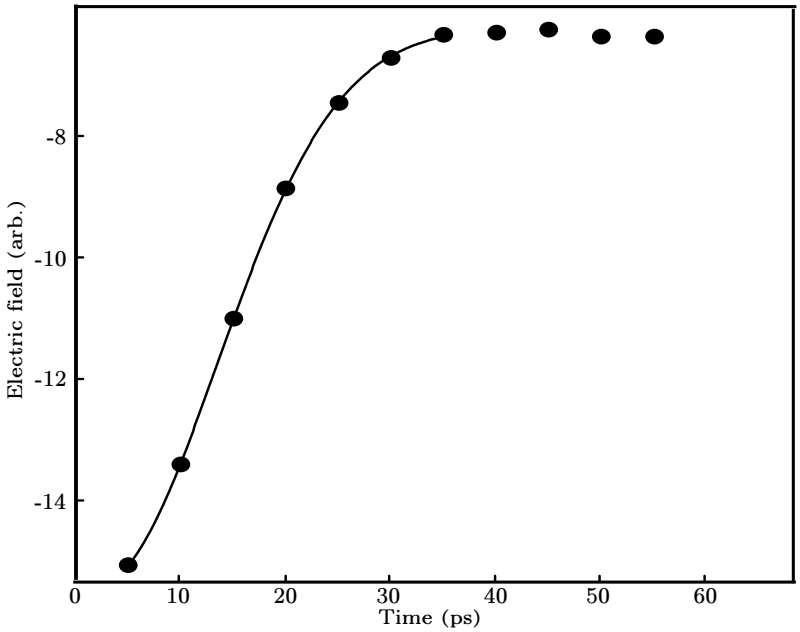

Figure 5.15: The first part of the decay trace measured at 10 K with pump fluence *iii* (symbols are the measured values). The rise time can be seen with a fitted Gaussian function (solid line) with a full width half maxima of 27 ps.

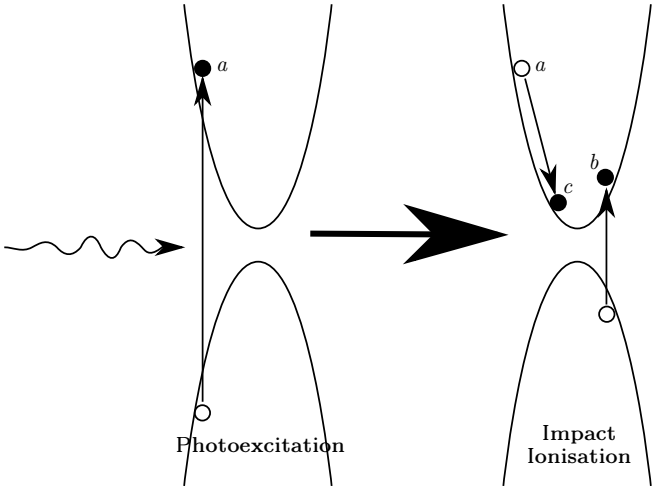

Figure 5.16: Schematic showing impact ionisation. Here energy from the photoexcited electron a is transfered to electron b as it decays to c, providing energy for b to be excited to d.

easily characterised with the experiment used here. There are two feasible improvements that would extend the characterisation capabilities. Increasing the delay line length and using picked pulse experiments (i.e. there would no longer be a pulse train but single pulses).

5.4 Conclusions

This chapter includes a detailed analysis of plasmonic materials using the Drude model. The Drude parameters of InSb have been found using transmission THz-TDS at a range of temperatures. Results have been gathered for the carrier dynamics of InSb on photoexcitation. These dynamics were significantly more complicated than initially expected. They show that the decay time is of the order 200 ps although for very high fluences it appears much longer which is probably due to heating of the sample. Analysis of previous work and that presented here suggests undoped InSb is the most suitable terahertz plasmonic material this is supported both in comparison to optical plasmonic materials and FDTD modelling of gratings. It is especially worth noting the large number of semiconductors with similar parameters to those shown in fig. 5.6 that do not support surface plasmons and the room temperature InSb result from the literature with a surface plasmon frequency outside the range of the spectrometer.

Chapter 6

Terahertz particle plasmons

Raether [26] discusses the evolution from normal surface plasmons to localised surface plasmon resonances (LSPRs) as roughness increases, this has also been extended to deep zero order monogratings and particle plasmons [164, 165]. LSPRs are a generalised form of particle plasmons. These phenomena have been heavily studied at optical frequencies as described in 2.3 including work on increasing the sensitivity of chemical detectors. It is the view of the author that terahertz particle plasmon resonances have some distinct advantages over their optical equivalents.

It is know that the strength of the localised field is proportional to the curvature of the particle relative to the wavelength [49], this is limited thermodynamically for the very small ($\approx$ 50 nm) metallic particles required for optical particle plasmon systems. Due to the size increase for terahertz particle plasmons (from $\approx$ 50nm to $\approx$ 100 µm) this limitation is greatly reduced and should allow for very sharp particles to be fabricated. As discussed by Lee [61] there is a wide range of chemicals which have very high and characteristic absorptions in the terahertz domain. It should also be possible to photomodulate the resonances; changing the sample response by altering the permittivity via photoexcitation.

An interesting aspect of electrodynamics arises when the movement of electrons in a material induced by a field is similar to the distance over which the field changes [166]. For terahertz particle plasmons it should be possible to construct devices where this non-locality situation is achievable. In this regime the common concept of a frequency dependent permittivity which is derived assuming locality breaks down and an additional wavevector (k) dependent term is required.

To initially show that terahertz particle plasmons can be supported finite element method (FEM) modelling has been conducted. This is an incident plane wave driven model of an infinite array as discussed in chapter 3. The unit cell is a pair of subwavelength rods on a substrate (pillars) of InSb (using a permittivity that assumes locality)

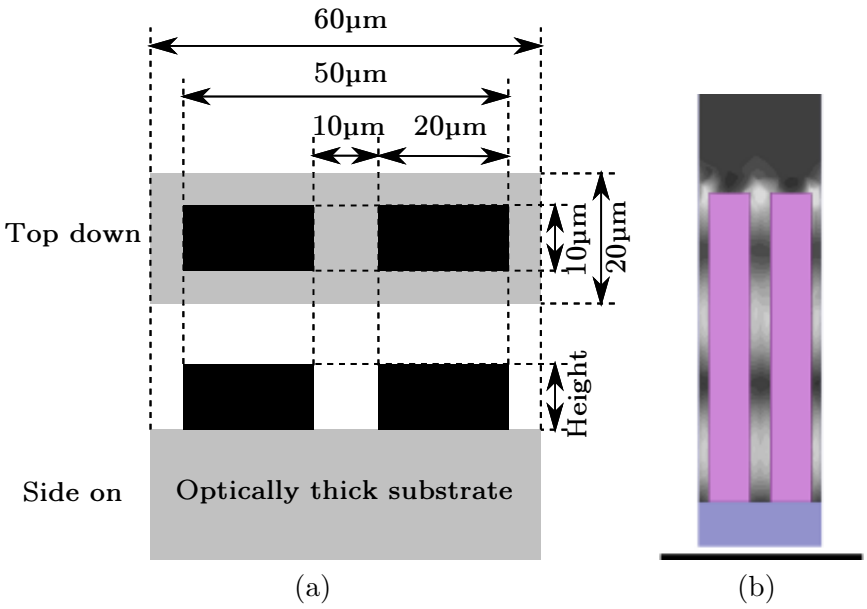

Figure 6.1: (a) The schematic of the unit cell for the connected structure used in finite element method modelling, where the substrate and protrusions are made of InSb. (b) Time averaged electric field profiles on a plane cut down the long axis of the connected particle array when $h = 150$ µm, high fields are shown in white and low fields in black, the scale bar is 100 µm.

as shown in figure 6.1(a). The dimensions of the rods in the model are length 20 µm, and width 10 µm, with a separation between the particles of 10 µm. The array has a long axis pitch of 60 µm and short axis pitch of 20 µm. The particle heights are varied between 10 µm and 150 µm. The reflection spectra found using an incident plane wave at normal incidence polarised along the direction of the long axis is shown in figure 6.2(a). Whereas figure 6.2(b) shows the reflection spectra of an identical array of rods with height 10 µm with no substrate therefore showing the particle plasmon mode. These spectra indicate that for the connected structure there are one or two resonances (depending on the depth) in the range 1.35 THz and 1.75 THz.

Considering the case where the height of particles is 150 µm the time averaged electric fields in the plane of the long axis have been plotted and shown in figure 6.1(b). The localised field profile can be seen clearly showing that there exists a localised plasmon mode similar to that reported by Tan et al and Hooper and Sambles [164, 167]. Both the connected and disconnected arrays support localised surface plasmon modes but depending on the fabrication method the connected structures might be easier to fabricate than free standing particles although free standing particles should still be aimed for.

In chapter 3 the terahertz spectrometers used in this project are described. There

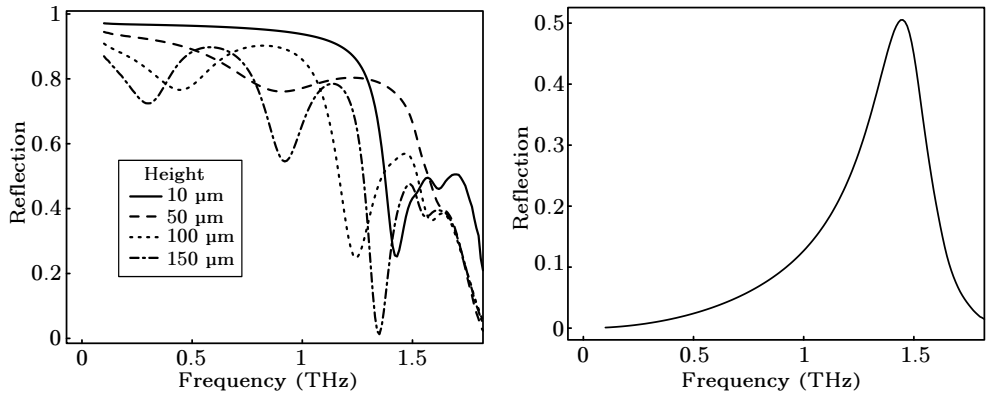

Figure 6.2: Reflection spectra for InSb rods (a) connected by an InSb substrate with varying particle heights, $h = 10\ \mu\text{m}, 50\ \mu\text{m}, 100\ \mu\text{m}$ and 150 µm, and (b) disconnected square rods ($h = 10\ \mu\text{m}$). The dimensions of the rods modelled are length 20 µm, and width 10 µm, with a separation between the particles of 10 µm. The array has a long axis pitch of 60 µm and short axis pitch of 20 µm.

it can be seen that the systems are complicated by configuring them into the reflection mode that would be required for the connected structures. The angle range of the focussing spectrometer is also restricted to $30 \pm 5°$. For the collimated spectrometer larger samples are needed, from 1 cm^2 for the focusing kit in reflection to 6 cm^2 for the collimated spectrometer. Modelling is also complicated for reflection systems as the boundary conditions at the incident interface need to be modified to not reflect the off normal radiation. It is therefore advantageous to attempt to fabricate free standing particles. The measured spectra are also simpler for free standing transmission type experiments as there is no quantisation along the depth of the particles. This is demonstrated in figs. 6.2 and 6.1(b).

At optical frequencies triangles have been shown to have large enhanced fields and produce high Q resonances [46, 47]. They have also been shown when in pairs ('bow ties') to produce large regions of high fields [168]. These attributes are desirable for three of the four proposed areas of interest here, sharpness, sensing and high photo-modulation (as high Q resonances should allow for larger modulations). The fourth interesting aspect, non-locality, is not restricted by the use of triangular particles. As discussed in chapter 5 InSb is the most suitable material for terahertz plasmonics. The investigation will therefore be mostly concerned with triangular InSb particles.

In this chapter there is a discussion of the fabrication methods that have been developed throughout this project. This is followed by an in depth exploration using finite element method (FEM) modelling using an incident plane wave driven model as

discussed in chapter 3. The permittivity used is found from the Drude parameters from [129], the permittivity is therefore local and all modelling presented here assumes this.

6.1 Fabrication

6.1.1 Chemical wet etch

Mesa (a transistor type) fabrication has been conducted for a number of years using wet etch methods (chemically dissolving the substrate). If these structures could be made deeper they would resemble the pillar type plasmons modelled above and be a suitable first test of terahertz particle plasmons.

A mix of two chemicals is normally used, the first an oxidising agent and the second which dissolves the oxide. A resist is coated onto the surface of the material to be etched and a pattern made in the resist protecting some areas of the material from etching. The initial test of this method involved spinning 500 nm of Poly(methyl methacrylate) (PMMA) which acts as a positive electron beam resist, resists are discussed in more detail in 6.1.3. This layer was patterned using an FEI dual beam focused ion beam and electron beam system (FEI Nova 600) to have an array of triangular spots left behind after developing. This was then submerged in a nitric acid/lactic acid mix with a ratio of 1:10. Based on the etch rates in the literature the sample was removed after 12 hours and any remaining resist stripped [169].

The results were unexpected with groves running over the surface, these were mostly orientated in a similar direction but not parallel to each other indicating that this isn't preferential etching of a crystal plane. It is expected for wet etching that there will be some undercutting of the resist [169], although for the size of the pattern used here this should have still left sizeable plateaus underneath the resist. An additional concern with wet etching is below surface damage for deep etches. Fig. 6.3 shows scanning electron microscope (SEM) images taken on broken edges of InSb wafers at 35° where the scale bars are 100 µm. Fig. 6.3(a) shows the unetched wafer where small areas of stress damage can be seen, and fig. 6.3(b) shows the etched sample, where the etchant was only incident on the top surface of the sample. Damage from the etchant can be seen over 200 µm under the surface of the sample. Therefore, it was decided that this method was unlikely to yield a uniform sample with tall, well formed particles with a permittivity close to that of InSb.

For the sample required in chapter 5 further tests of wet etching were conducted. Different solutions were trialled varying the ratio between lactic and nitric acids on InSb with no mask deposited. The results suggested a saturation of the material etched and after a short duration ($\approx$ 5 min) the InSb surface can be seen to tarnish. This occurs

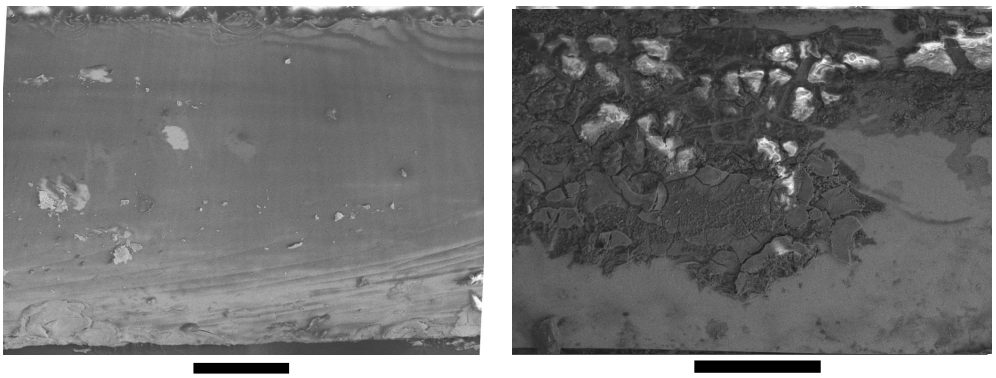

(a) (b)

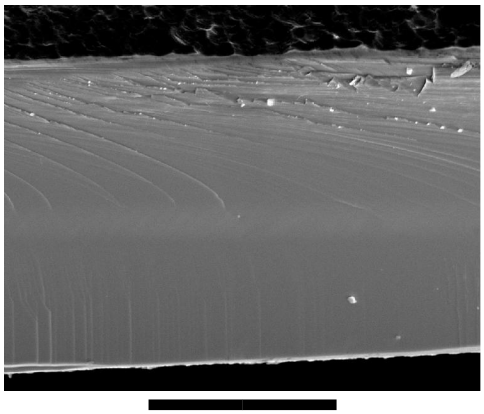

(c)

Figure 6.3: Snapped side of InSb wafers at 35° where the scale bars are 100 µm. (a) An unetched wafer, some stress damage from breaking the sample can be seen, (b) a sample etched using a lactic and nitric acid mix, where the etchant was only incident on the top surface, damage can be seen over 200 µm under the surface of the sample, and (c) the material has been etched by ≈ 250 µm in nitric acid no damage other than that due to the stress on breaking the sample can be seen.

even in 100% Lactic acid. Submersion in nitric acid removes this tarnish.

Prolonged submersion in nitric acid with no lactic present etches the wafer at a rate of ≈ 20 µm/min, much faster than previously reported methods. It is thought that a rapid etch rate such as this would not provide the time for deep damage of the sample, this is supported by fig. 6.3(c), another SEM image of the side of a wafer broken after etching this time showing no deep damage.

This method is not a panacea, fig. 6.4 shows optical microscope and SEM images of the surface of an InSb wafer after etching. The roughness appears to be curved with length scales of ≈ 1 µm in depth and ≈ 10 µm across the surface. During the etching, bubbles form on the sufrace of the sample, it is thought that these cause the shape of

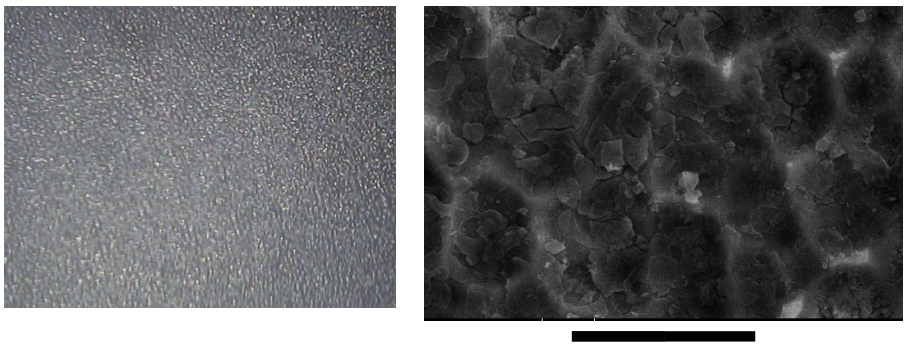

(a) (b)

Figure 6.4: The surface of an InSb wafer after etching in nitric acid, (a) an optical microscope image and (b) an SEM image, where the scale bar is 20 µm.

the roughness. Efforts were made with 'dipping' the sample in and out of the acid but no difference was observed. To reduce the roughness the sample was suspended above a bath of nitric acid in a partially sealed container. Nitrogen was then bubbled through the acid to create a high nitric acid atmosphere inside the flask. The idea was that as the contact of nitric acid with the sample would be reduced to droplets the bubbles could not form. Nitrogen was bubbled through the acid for 3 h, condensation formed on the sides of the container for most of this time, although no difference in sample thickness was measured.

As this etching method seemed to produce fast results it was thought worthwhile attempting to create pillars using only nitric acid. Fig. 6.5 is an optical microscope image of the best attempt to create triangles using this etching method. Samples with both photoresist and chromium maskers were tested, these masks are discussed below. Fig. 6.5 used a chromium mask. The curved triangles are due to a curved mask being used. The etch is ≈ 1.5 µm deep, not enough to conduct the measurements required here. Attempts to make deeper samples failed, a different approach was therefore taken.

6.1.2 Focused ion beam

Focused ion beam (FIB) etching works by ablation of the surface of a material by bombardment of ions which have been accelerated and focussed using a series of electomagnets. The system available at Exeter (FEI Nova 600) uses a Gallium source which can be used to make feature sizes of ≈ 10 nm, this is significantly smaller than the feature sizes required at terahertz frequencies. This system also comprises an electron beam which allows imaging of the sample. The two beam paths are 55° from each other with a mechanical stage being used to present the sample at normal incidence to each beam path. There were several methods proposed and tested using the FIB. The first

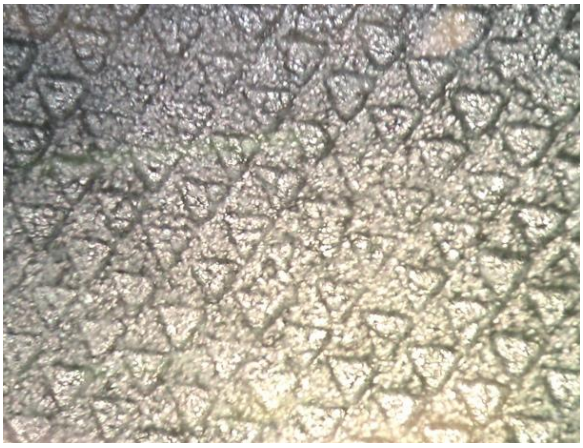

Figure 6.5: The surface of an InSb wafer after etching in nitric acid with a chromium mask of curved triangles being deposited before etching. This is an optical microscope image, the base to point length of each triangle is around 100 μm.

tests exploited the variable angle of incidence of the FIB, using two angled slots cut parallel to each other, with straight cuts being made at either end, creating a triangular prism shaped particle free from the substrate, the cuts are shown in fig. 6.6(a). These could be cut in a regular array before being stuck to a piece of self adhesive supporting film and removing the substrate, leaving the triangular prism InSb particles behind. This proved to be too time consuming taking more than 50h of etching time for each particle.

The next method attempted was designed to greatly reduce the etching time. An InSb wafer was first cleaved leaving an angled edge, into this a line of slots perpendicular to the edge were cut and then another cut etched along each of these 'teeth' to create free particles. In fig. 6.6(b) three remaining particles can be seen along with the remains of the wafer, the rough edge shows where each of the teeth were cut before their removal from the substrate. This method leaves a pile of unordered particles (similar to that shown in fig. 6.6(c)) on a glass substrate which then needed to be aligned in an ordered array.

6.1.2.1 Post etching positioning

The small particles fabricated above needed to be positioned into a regular array. This was achieved using a hydraulic micro positioner similar to that discussed in 6.1.3, the tip of which must be very sharp. A stretched pipette was found to be the best as it offered more strength than stretched plastic, and was less susceptible to sticking to the particles than a metal needle. The sticking was still a problem, this and the very small size of the particles fabricated resulted in the positioning being a very difficult task.

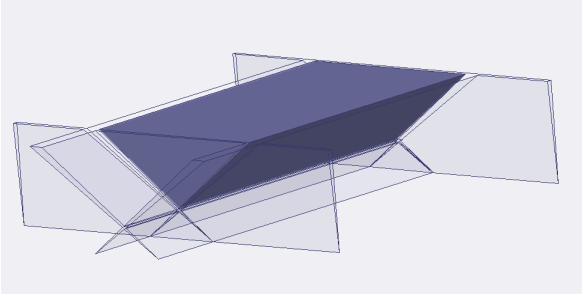

(a)

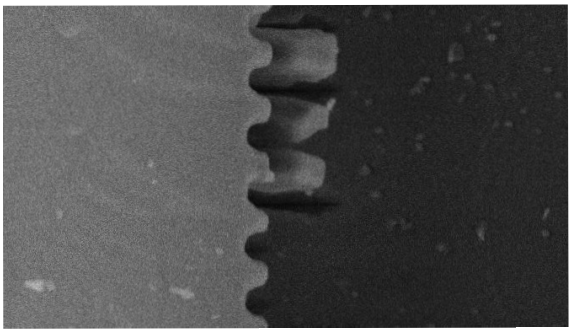

(b)

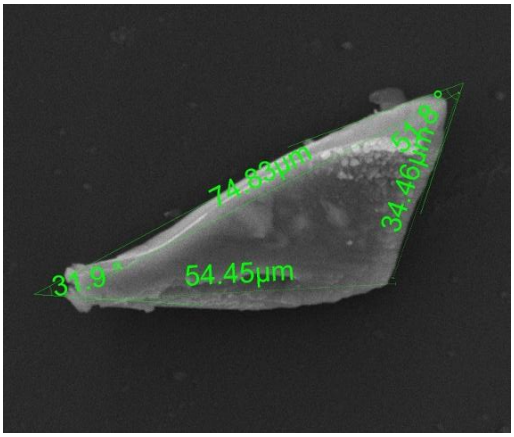

(c)

Figure 6.6: (a) Schematic view showing the four cuts required to cut a triangular prism particle using a FIB on a flat InSb substrate, the cuts are tapered slightly similar to the shape of the FIB. (b) Three remaining particles on the side of an InSb wafer after teeth have been etched into the edge of the angled side of the wafer before another cut is made to remove the particles from the substrate. (c) An SEM image of a single particle cut from the side of the wafer.

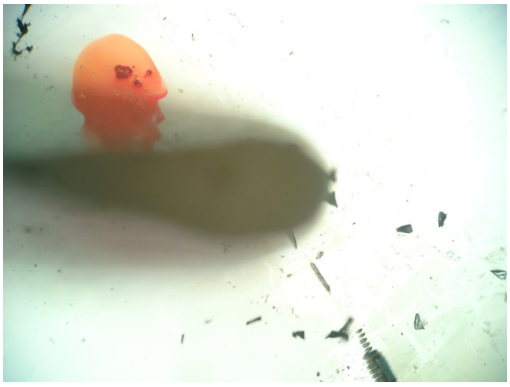

Figure 6.7: An optical microscope image showing the positioning of the triangular shaped particles cut using the FIB. The red mark is a positioning point. The cuts into the substrate in the bottom right are where the particles were made.

Fig. 6.7 is an optical microscope image of a stretched pipette out of focus shown with the particles to be positioned. The red mark is an indicator to show where the particles on the substrate are located and the regular line of marks are where the FIB has cut into the substrate.

6.1.2.2 Results

Fig. 6.8(a) shows the best result using the method described above, using the FIB to create particles and then positioning them. They are attached to a self adhesive film as a support structure and surrounded by a 2 mm metal aperture. A similar aperture also mounted on support film was used as a transmission reference. The transmission through this sample can be seen in fig. 6.8(b), there is a 10% dip in the transmission spectra around 0.65 THz which is possibly attributed to the LSPR of the triangles. Due to the very poor periodicity, and similarity between the particles in the array it is very difficult to model, and impossible on the computers available for the project. It therefore cannot be stated with any degree of certainty that this dip is due to the particle plasmons resonances, although, it is consistent with inhomogeneous broadening of a resonance due to irregularities in the array [170].

This process has several drawbacks, the inconsistency between both the particle shapes and their subsequent position are the most apparent. This coupled with the time involved in making a single sample both in terms of etching time and positioning time render the process impractical.

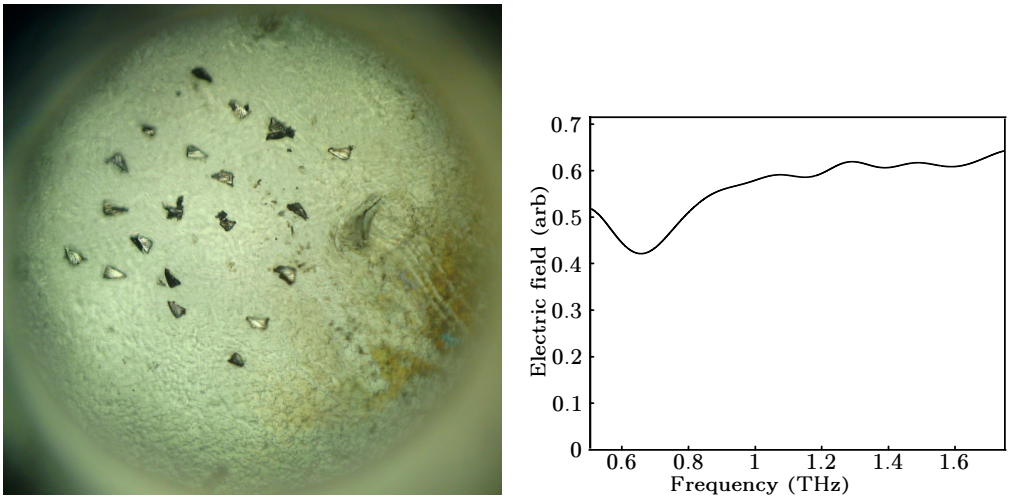

(a) (b)

Figure 6.8: (a) A SEM image of the array of triangles cut using a FIB and positioned using a micropositioner. The outer ring is a metallic aperture. (b) The normalised transmission intensity measured through the InSb particles.

6.1.3 Reactive ion etching and chromium masks

Reactive ion etching (RIE) is a fabrication process for removing exposed areas of a given material. The sample to be etched is placed into a vacuum chamber, a plasma is formed by the injection of some gas into a large electric field within this chamber. This bombards the sample with high energy ions. The injected gas mix is tuned to the material to be etched so that the sample is chemically etched and not simply sputtered. For InSb this process has again been used for etching mesa structures [171, 172]. These processes are too slow to be utilised for the deep etching process needed to fabricate arrays for InSb particle plasmons. Recently faster deep etching processes for InSb have been developed [173] these processes are similar to those developed for other semiconductors [174, 175]. This process again requires a mask.

Due to the high etch rate even for materials not matched to the gases used, a hard mask is required. This is normally satisfied by using a chromium mask around 50 nm thick. In most circumstances to create a chromium mask a photolithography mask is applied on top of a chromium layer on the substrate. The substrate is then submerged into a wet etchant designed for chromium (e.g. perchloric acid and ceric ammonium nitrate), the remaining photoresist is then removed.

Photolithography is a process for producing a pattern in a polymer layer on a surface. There are three resist types that have be used at some point in this project, positive, negative and image reversal. On illumination with light of the correct energy

(resist specific) a chemical change occurs. When submerged in a developer the exposed area either dissolves (positive resist) or the exposed area remains with the surroundings dissolving (negative resist). For image reversal resists either effect is possible depending on the processes applied after exposure, a starting positive resist can be changed to a negative and vice versa. Electron beam lithography is similar but electrons are used for patterning as opposed to light.

The results of the chemical wet etch of chromium was repeatable and conducted with InSb and silicon wafers in parallel. For the silicon substrates the triangles were well formed, with a near perfect success rate. The chromium deposited onto the InSb substrates, without exception, failed to etch. Etch times used for the silicon were ≈ 5 s, for InSb etch times of between 5 s and 36 h were attempted. For InSb, including the longest etch times, the chromium layer was left unchanged. It is thought that there is some bonding effect between the layers which is unusually strong. The back of the InSb wafer discoloured for the long etching times.

Dielectric barrier layers were subsequently attempted. A thin ($\approx$ 15 nm) layer of MgF was evaporated onto an InSb substrate, unfortunately this layer was too rough for the subsequent mask deposition method to work. A $\approx$ 500 nm layer of PMMA was spun down onto silicon and InSb substrates, the chromium mask process was then conducted. The etchant for the chromium damaged the PMMA boundary layer, destroying large areas of the mask.

Again using a PMMA protection layer. A photoresist is deposited by spinning on top of the dried PMMA, this layer was ≈ 1 µm thick. A photolithography process puts an array of triangular holes in the photoresist. The resist layer is again exposed before a thick ($\approx$ 500 nm) chromium layer is deposited. The second exposure is so the photoresist can be removed by development without damaging the PMMA layer. This development process should remove the chromium from around the triangles. This development-lift off stage is somewhat problematic. Fig. 6.9 shows two optical microscope images from two regions of the same sample, a few mm apart. In one, the triangles can be seen as coloured areas, this is the PMMA layer with the surrounding photoresist. The other image shows no lift off. This is obviously very different lift off results for regions of the same sample that are close together.

It was found that very short initial development results in curling of the chromium layer from the edges of some triangles as shown in fig. 6.10. It was observed in developer under a microscope that often when this curling reaches another triangle it rips the triangle from the surface as it continues to roll up.

Apparatus as shown in fig. 6.11 was used so that a stretched glass pipette with an ≈ 10 µm point (fig. 6.10) could be pushed around the surface using a hydraulic micropositioner (fig. 6.11(b)). This was used to break the curls before a subsequent

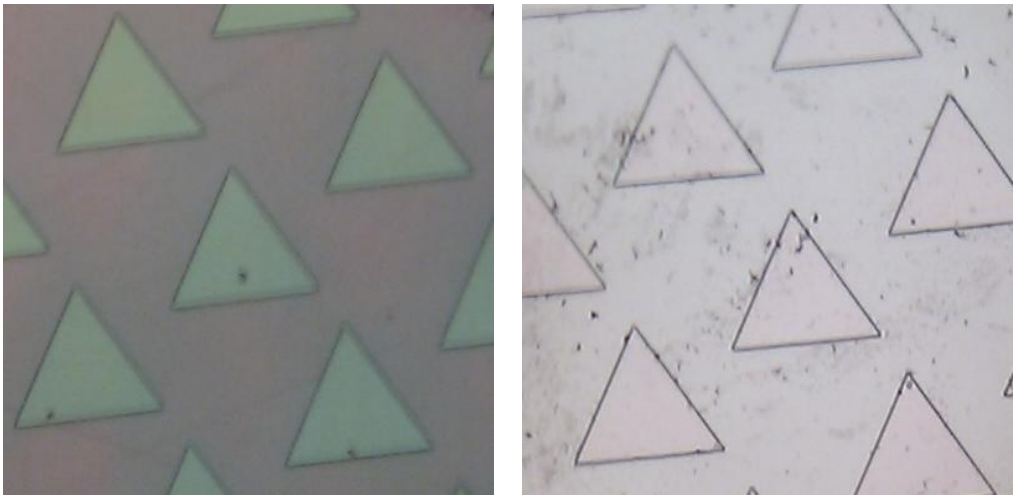

(a) (b)

Figure 6.9: Two regions of the same sample after the lift off procedure. Remaining on the surface should be chromium triangles on a PMMA protective layer on an InSb substrate. The difference between the regions is very visible. The base to point length of the triangles is 100 µm.

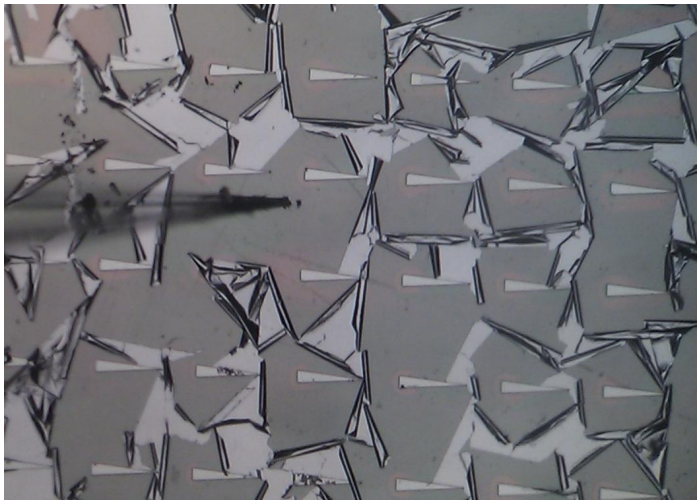

Figure 6.10: Curling of the chromium layer on the photo resist is observed originating at the edges of some triangles. The point of the stretched pipette is also shown.

development. This scraping, cleaning in deionised water, and development can be repeated until a clean array of triangles is produced as seen in fig. 6.12.

It was thought that this array of chromium particles on PMMA on an InSb substrate could then be RIEed to create pillars of InSb capped with PMMA and chromium. This cap could then be removed with submersion in acetone. The resulting arrays could be used as LSPR arrays as discussed above. With future developments of RIE technologies it should be possible to stick the pillars to a self adhesive supporting film and subsequently etch to remove the back ≈ 400 µm of InSb wafer leaving well formed isolated InSb particles in a regular array. Alternatively it might be possible to stick a substrate that is transparent at terahertz frequencies to the particles and remove the InSb substrate leaving the particles behind.

Unfortunately the etch recipe tried at Cardiff University using an inductive coupled plasma caused a burning effect on the PMMA layer, fig. 6.13(a) shows a photograph of the damaged surface. Efforts were made to remove the PMMA from around the mask, leaving it under the chromium mask by using an oxygen plasma. This was successful but even at the lowest temperature that can be used for a realistic etch rate (100 °C) the PMMA underneath the chromium melted and spread, again burning. This can be seen in 6.13(b), again a photograph of an InSb wafer after etching.

A new sample was produced with only chromium on InSb by using the above photolithography process but with no PMMA layer. Here the etch was somewhat successful. Fig. 6.14 shows the resulting pillars. They are only 3.4 µm high, 10 times thinner than desired. This is due to the selectivity of the chromium being significantly lower for this etch recipe than expected [176]. These could not be removed from the surface by adhesion and separation.

6.2 Modelling results

During this project FEM modelling has been conducted in parallel to the different sample fabrication methods. Some more general modelling has also been conducted. The following is a summary of the interesting results. This modelling uses the methods described in chapter 3 to (unless otherwise stated) model infinite arrays for particle plasmons in transmission at terahertz frequencies. The permittivity used is found from the Drude model with parameters taken from [129], $\omega_{sp} = 46$ THz$/2\pi$ and $\gamma = 0.63$ THz$/2\pi$, it therefore makes the assumption of locality.

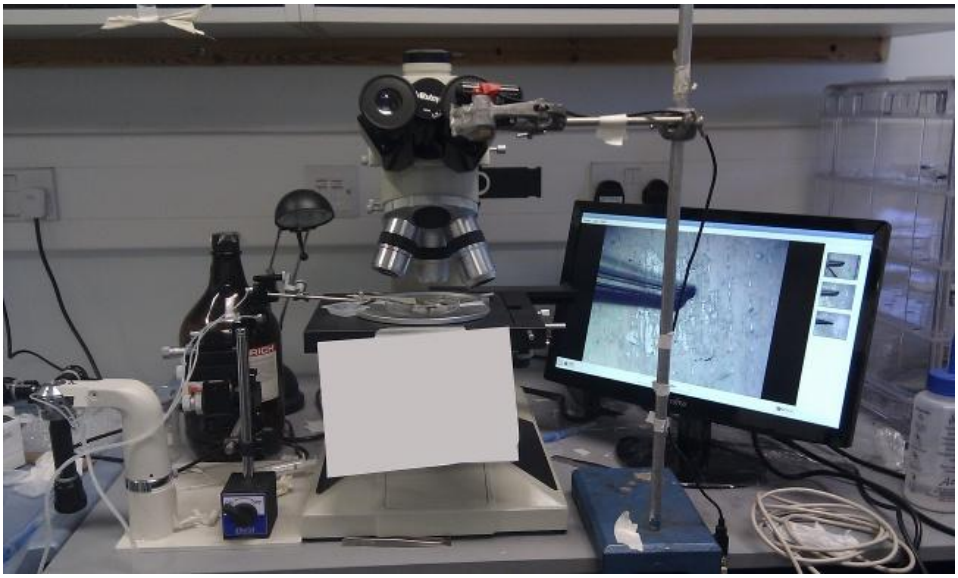

(a)

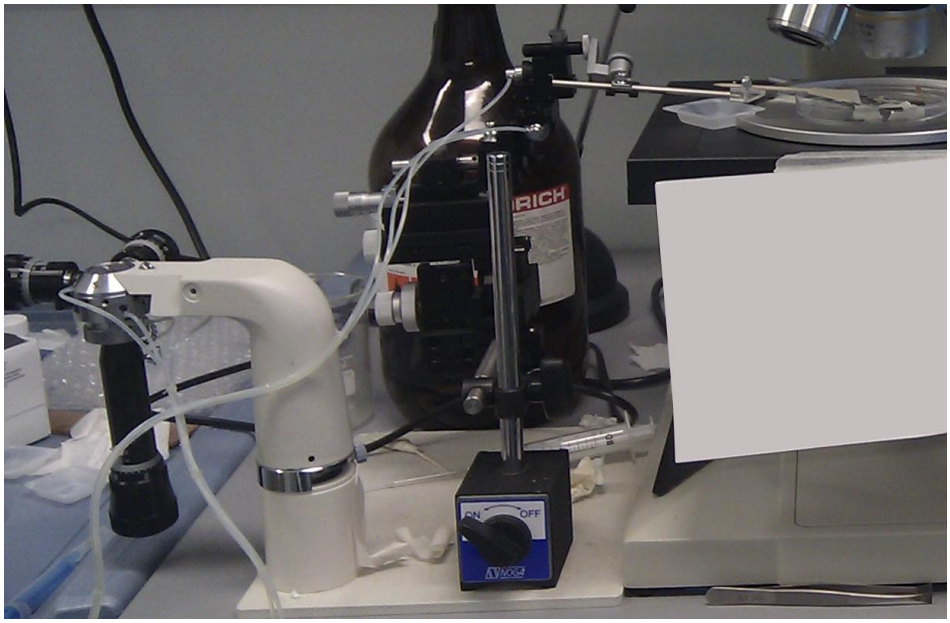

(b)

Figure 6.11: The optical microscope setup used for scraping the chromium mask to clean it. (a) An overview of the microscope, with the camera used shown. (b) The hydraulic micropositioner that was utilised.

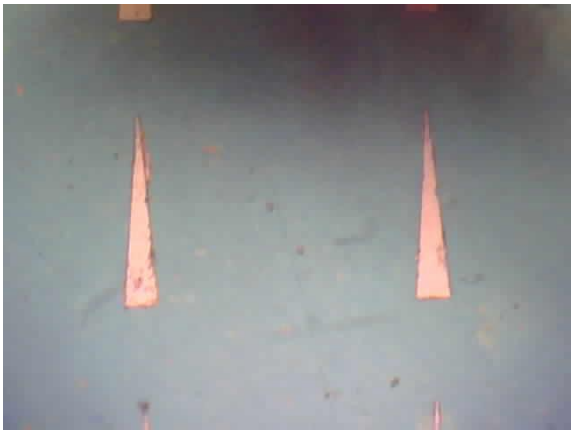

Figure 6.12: Part of a cleaned array of chromium triangles on a PMMA protective layer on an InSb substrate.

(a) (b)

Figure 6.13: Photographs of two InSb wafers with PMMA and chromium masks on top. Both show burning from the RIE process. (a) shows the case with the surrounding PMMA and (b) where the surrounding PMMA was first removed.

6.2.1 Particle pairs

At optical frequencies the increased field enhancement between particles has been the subject of much interest [177–180]. The capacity to investigate this is limited at optical frequencies compared to terahertz frequencies due to the small distances between particles relative to the wavelength before it becomes difficult to define whether the particles are combined or separated. In light of this, modelling has been conducted where the electric field strength directly between a pair of InSb particles was found for a range of frequencies in the terahertz regime where the polarisation of the radiation is in the direction of the vector joining the centre of each particle. Reducing the distance between the particles increases the field enhancement as can be seen in fig. 6.15. This figure shows the field enhancement spectra for different separation distances for spherical (6.15(a)) and triangular (6.15(b)) particles. The particle pairs are modelled as a single pair in free space (i.e. not an infinite array), the spheres have a diameter

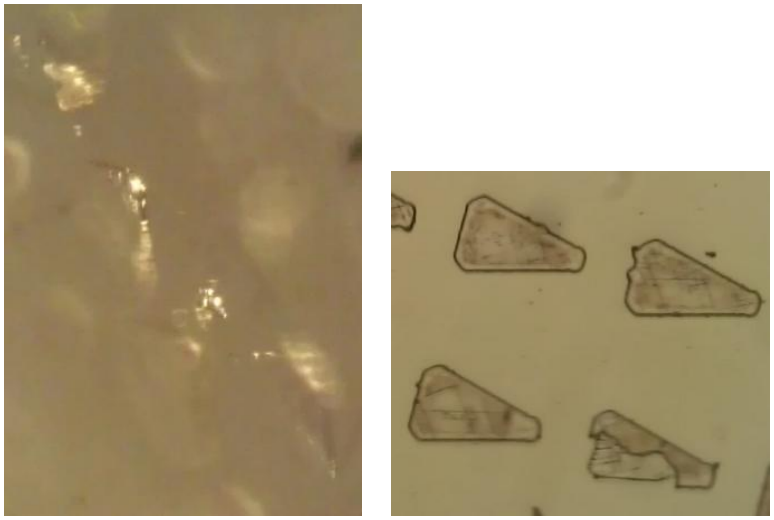

(a) (b)

Figure 6.14: Optical microscope images of etched InSb pillars. (a) Side on at an angle of $\approx 75^{\circ}$ and (b) top down.

of 30 µm and the triangles a base to tip length of 30 µm with a thickness of 10 µm. Fig. 6.16 shows field plots of the time averaged electric field in a plane cutting through the particles halfway from their base to their top. The field plots show that the area covered by high electric fields is large compared to the size of the particles. These areas of large fields are a useful feature for sensor applications as it extends the highest region of sensitivity to the molecules to be detected. The triangle pairs also show a large enhancement factor of over 300.

6.2.2 Varying sharpness

As sharper particles relative to the wavelength are achievable at terahertz frequencies compared to optical frequencies an investigation into changing the sharpness may allow for a greater understanding of this physical phenomenon. Three ways of varying the sharpness of a triangles are illustrated in fig. 6.17, truncating the point (fig. 6.17(a)), rounding the point (fig. 6.17(b)), and changing the angle (fig. 6.17(c)).

Rounding tends to be a natural occurrence. Fig. 6.18 shows two triangle models overlaid on one another, one is pointed and the other rounded. The rounded triangle is similar to that imaged in fig. 6.6(c) fabricated using a FIB method. Here the polarisation is in the direction of the long axis of the particles. The particle thickness is 10 µm, the long axis 61 µm and they are modelled for an array with a pitch of 150 µm. The transmission response for these two arrays is shown in fig. 6.19, the curved triangles are shown as the solid line and the pointed as the dashed. Surprisingly

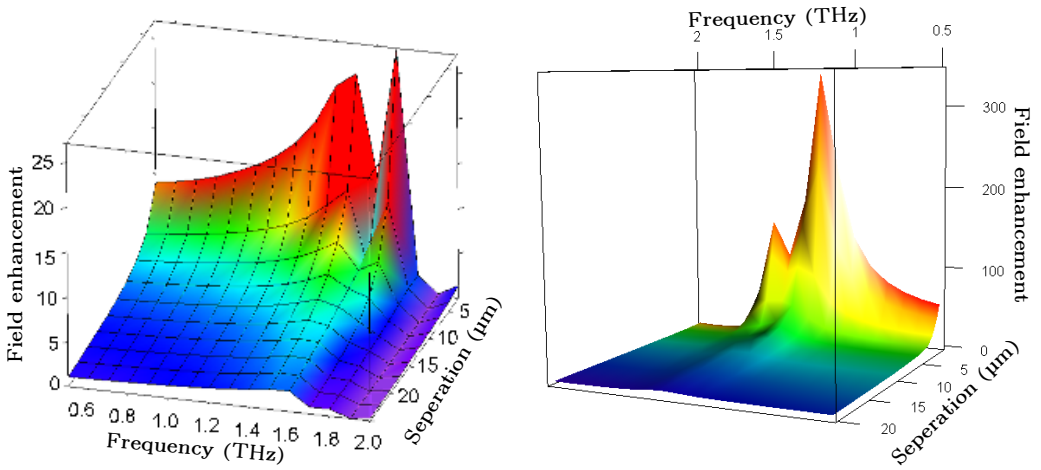

(a) (b)

Figure 6.15: Spectra of field enhancement in between the particles of particle pairs as the separation distance is decreased. These are shown for (a) spherical particles and (b) triangular particles.

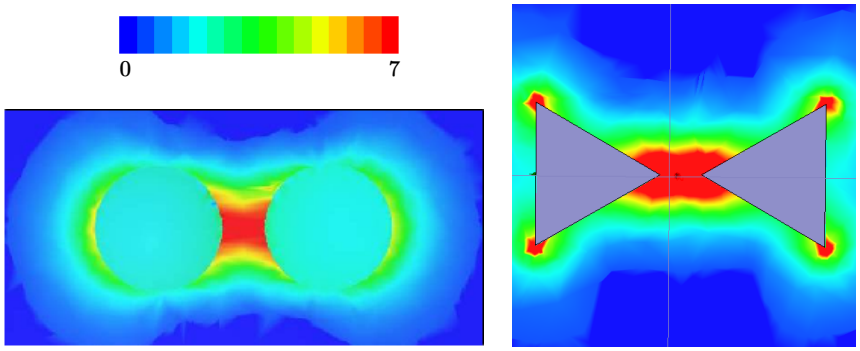

(a) (b)

Figure 6.16: Field plots of the time averaged electric field in a plane cutting through the particles halfway from their base to their top. The spheres have a diameter of 30 μm and the triangles a base to tip length of 30 μm with a thickness of 10 μm.

the curved triangles show a deeper minima, this is possibly due to the larger material content or that the particle is slightly wider which Kottmann et al. suggests provides deeper resonances [46, 47] .

Figs. 6.20 and 6.21 show the time averaged electric field profiles on a plane cut through the middle of the particles. Each pane is produced for each of the minima shown in the spectra. The colour scale is logarithmic, showing that the pointed particles have a larger area of highest field enhancement, and therefore a higher peak enhancement, as expected. The curvature around the sides of the particles seems to have increased

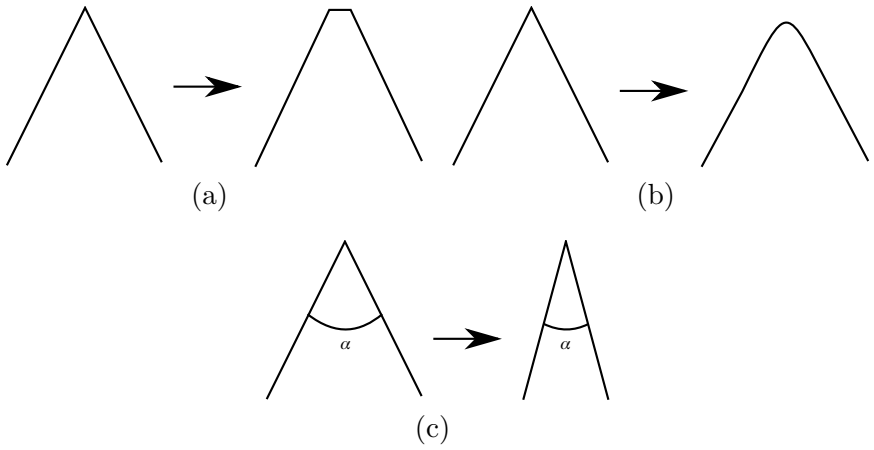

Figure 6.17: Three different methods of altering the sharpness of particles, (a) truncation, (b) rounding and (c) changing the internal angle (α).

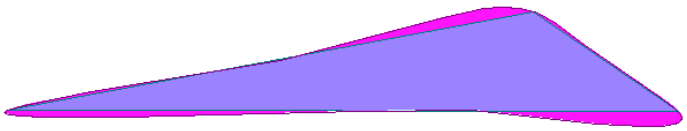

Figure 6.18: Rounded and pointed triangles overlaid showing the difference between the two modelled particle shapes.

the overall enhanced field area compared to the pointed triangles, this is likely to contribute to the deeper particle resonance. For some sensing applications a larger area of increased field may be preferred to a smaller region of much higher fields.

Truncated triangles have not been modelled here but there has been work conducted on them in the literature at optical frequencies [181]. They are noteworthy due to the ease of using the same photolithography mask for both triangles and truncated triangles. Fig. 6.22 shows two arrays of triangles fabricated using the same photolithography mask. The difference being the truncated triangles are formed by slightly overexposing the photoresist.

The photolithography mask produced for this project has three regions of different sharpness triangles, as shown in fig. 6.23(a). The transmission modelling results for arrays of these three triangles with a pitch of 200 μm are shown in fig. 6.23(b). The sharpest particles, with an internal angle (α) of 15° are shown as the solid line, the intermediary particles ($\alpha = 30°$) as the dashed line, and the broad particles ($\alpha = 60°$) as the dotted line. There are three noticeable changes. For the narrower particles, the resonances are sharper, the resonance has split into two distinct peaks, and the minima

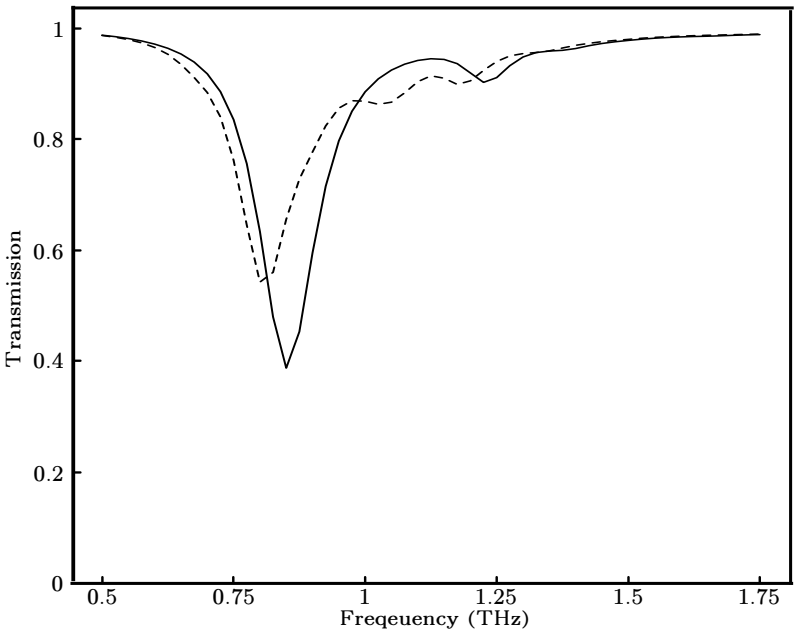

Figure 6.19: Transmission response for rounded and pointed triangle arrays, the curved triangles are shown as the solid line and the pointed as the dashed.

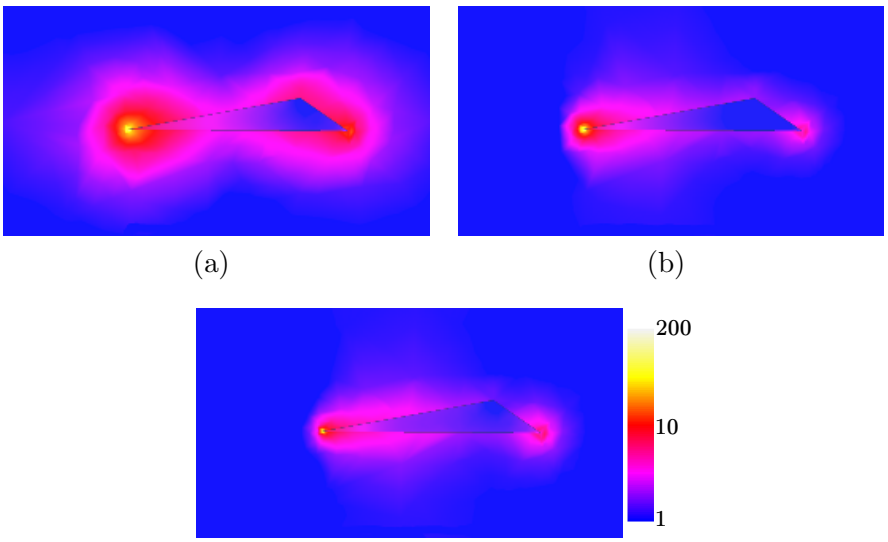

Figure 6.20: Time averaged electric field profiles on a plane cut through the middle of the particle, modelled in an infinite array. The particle thickness is 10 μm, the long axis 61 μm and they are modelled for an array with a pitch of 150 μm. These field plots are for pointed particles as shown, at (a) 0.8 THz, (b) 1.025 THz, and (c) 1.175 THz.

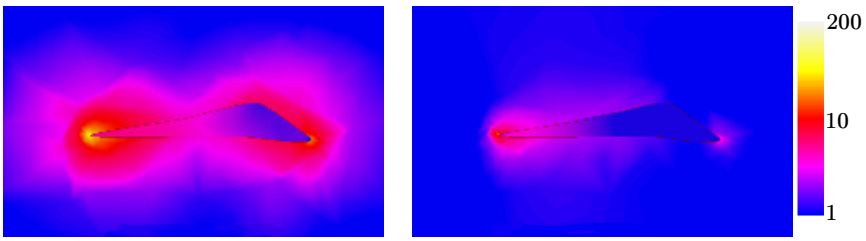

(a) (b)

Figure 6.21: Time averaged electric field profiles on a plane cut through the middle of the particle, modelled in an infinite array. The particle thickness is 10 µm, the long axis 61 µm and they are modelled for an array with a pitch of 150 µm. These field plots are for curved particles as shown, at (a) 0.85 THz, and (b) 1.125 THz.

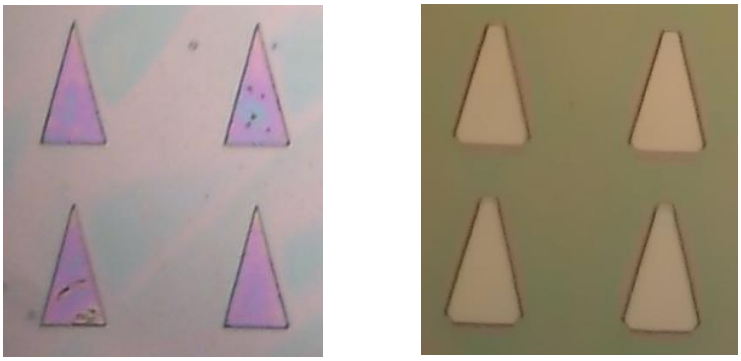

(a) (b)

Figure 6.22: Optical microscopy images of two arrays of (a) triangles and (b) truncated triangles fabricated using the same photolithography mask.

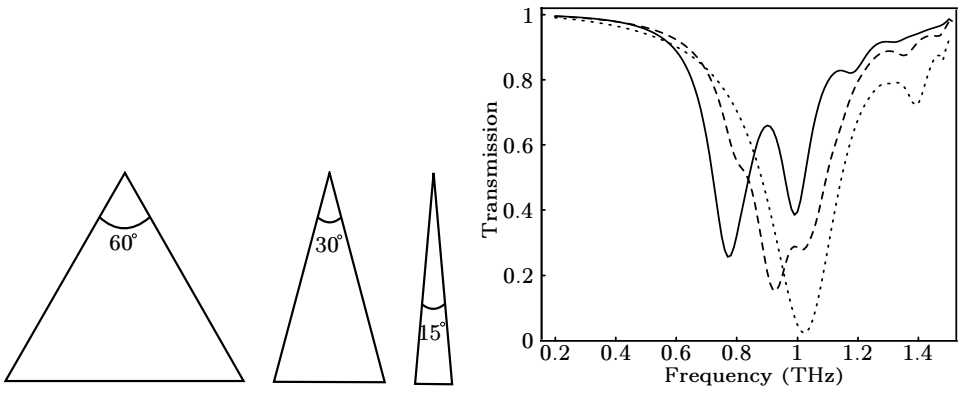

(a) (b)

Figure 6.23: (a)A schematic of the three triangle types reproduced on the photolithography mask. (b) The transmission through modelled arrays of these three triangles. The sharpest triangles ($\alpha = 15°$) are shown as the solid line, the intermediary particles ($\alpha = 30°$) as the dashed line, and the broad particles ($\alpha = 60°$) as the dotted line.

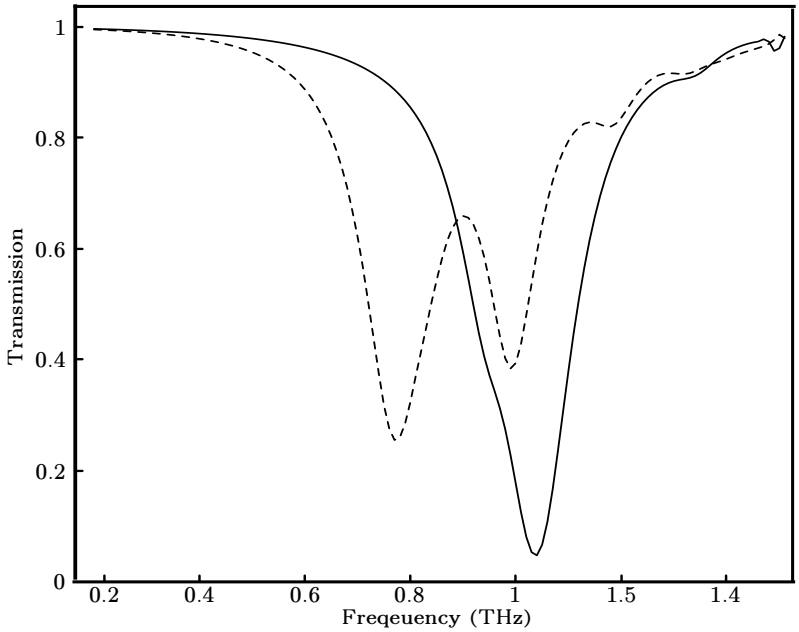

Figure 6.24: Calculated transmission through arrays of InSb triangles, the dashed line is the normal response with the solid line showing the effect of an increase in carrier concentration of 1×10^{16} cm^{-3} an increase of 50%.

reduced. The reduction of the resonant minima can be attributed to the reduced fraction of the area covered by InSb. The sharpness of the resonance can be attributed to the increased sharpness of the particles as seen by Kottmann [46]. Similar splitting is also observed in [46, 47]. The field profiles for both resonances are remarkably similar, the larger resonance at 0.77 THz has slightly larger fields at the pointed end relative to the base end, with larger fields inside the particle than are observed for the resonance at 0.99 THz but this is marginal. The direction of the electric fields at a single point in phase are reversed for each resonance. For one resonance they are pointing into the point and away from the base, for the other into the base and out of the point, which is which depends on the point in phase that is evaluated.

6.2.3 Photomodulation

As discussed in chapter 5 the permittivity of a semiconductor can be modified by illumination. It is relatively easy to model this to a first approximation by changing N, the carrier concentration in (2.23) for use in the Drude model.

Fig. 6.24 shows the transmission for identicle arrays of narrow ($\alpha = 15°$) triangles as used in fig. 6.23. The dashed line uses permittivities with 'normal' parameters in the Drude model for InSb. The solid line represents the case where ω_p is modified by an increase in the carrier concentration of 1×10^{16} cm^{-3}. This shows a photomodulation of

the transmission at 0.77 THz of 65% could be possible if a way to fabricate an idealised sample was found. This compares to a photomodulation of 55% measured by Padilla et al. [157] for a change in carrier concentration of 4×10^{16}, quadruple that used here.

6.3 Conclusions

Terahertz InSb particle plasmons should allow for the probing of some interesting physical phenomena such as non-locality and very large photomodulations. They also have possible practical uses in sensors where the large regions of high fields can be utilised possibly in conjunction with the photomodulation effects, although fabrication of these structures is not trivial and has proved illusive in this project.

Chapter 7

Surface modes on open ended hole arrays

In chapter 2 the surface plasmon dispersion relation is derived, and the physics of the plasmon discussed. From there it is noted that the interesting plasmonic effects occur close to where the real part of a materials permittivity $(\epsilon'_m) = -1$ this is achievable at optical frequencies, as shown in chapter 2 and also using semiconductors at terahertz frequencies, as demonstrated in chapter 5. For metals at terahertz and microwave frequencies the real part of the permittivity is very large and negative, it can in many cases be approximated to a perfect electrical conductor (PEC), where there is no field penetration into the surface so surface plasmon modes cannot be supported.

However, it has been shown that surface plasmons can be mimicked by structuring the surface of the conductor, for example, by introducing periodic arrays of dimples on the surface. Such a structured surface of a highly conducting sample can support surface plasmon-like modes at frequencies well below the surface plasmon frequency of the conductor [182–184]. These surface modes have since become known as "designer" or "spoof" surface plasmon modes, with almost arbitrary dispersion generated through structure rather than material composition. For dimpled metal surfaces, the properties of spoof surface modes were first considered using simple analytical formalisms [182–184], and have since been confirmed by rigorous numerical modelling [185–188] and experiments at microwave [189, 190], and subsequently THz frequencies [191]. These surface modes are investigated further in this chapter.

7.0.1 Terahertz hole array measurement

The focusing terahertz spectrometer discussed in chapter 3 used in reflection, with blades added at the focus of the parabolic mirrors enables coupling to surface modes

as discussed in section 2.1.3. This has been conducted with a square array of circular dimples in an aluminium sheet, as shown by the scanning electron microscope image in fig. 7.1(a). The etched area is 4 mm in lateral width, and 1 cm in the direction of propagation. It can be considered as a strip waveguide, where surface waves are allowed, compared to the surrounding metal surface. The circular holes have a diameter of 50 μm and a depth of 90 μm in a square array (pitch 70 μm) at 45° to the propagation direction and were etched by a focused laser beam, they therefore have a conical bottom. Fig. 7.1(b) shows the measured dispersion from this hole array (curved solid line), along with an analytical model taken from [184]. Numerical modelling using the eigenmode solution method discussed in section 3.4 has been conducted but is not shown due to its similarity to the analytical modelling. The analytical model assumes the holes are cylindrical all the way to the bottom, whereas the numerical model has a taper included, the unit cell is shown in 7.1(c).

There is a clear discrepancy between the modelling results and the measured dispersion, this can be attributed to one of several possible causes. A slight angular change of the sample in the spectrometer can add a variation in the measured wavenumber. The edges of the waveguide may be causing a lateral confinement, although some brief modelling of the system suggests that this should only effect the dispersion when the number of unit cells is greatly reduced. The most likely cause of the discrepancy is due to the roughness on the surface caused by the etching. There are areas of deposited material around the edges of the holes. This is not easily modelled due to the irregularity of the surface. Further experiments presented here are for microwave frequencies where phase sensitive measurements can also be conducted, as discussed below. The effects observed are consistent across both frequency regimes. It is advantageous to move to the microwave regime as the wavelength increases so does the feature size. This enables samples to be made by traditional mechanical machining where discrepancies can be minimised compared to the wavelength by filing.

7.0.2 Motivations

As discussed above, surface plasmons are responsible for a host of interesting phenomena. Pendry [192] and others [193–195] highlighted the critical role that surface plasmons play in metal slab superlenses. It is intriguing to know whether the similar anomalous transmission effects observed in two-dimensional arrays of subwavelength, open holes in a highly conducting sheet (shown in fig. 7.2(a)) are due to spoof plasmons; previous work has indicated that a link is highly likely [196, 197].

In this chapter a modified modal matching method, similar to that developed for dimpled conducting surfaces [184], is formulated and compared to phase sensitive mi-

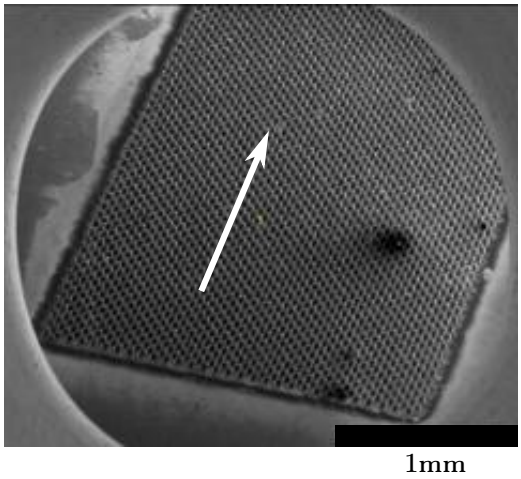

(a)

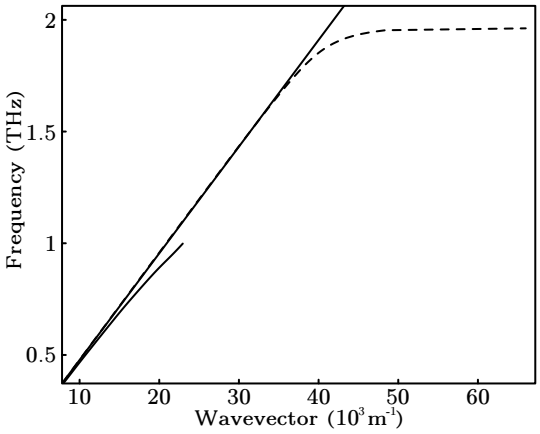

(b)

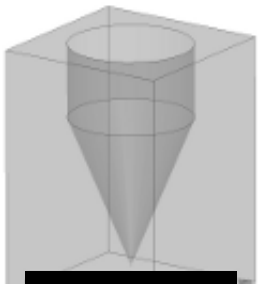

(c)

Figure 7.1: (a) Scanning electron microscope image of the array of dimples in aluminium, with diameter = 50 µm, depth = 90 µm, and pitch = 90 µm. The sample array is square with the direction of propagation, shown by the arrow, at 45° to the lattice vectors. (b) The measured (solid curved line) and analytical modelled (dashed line) dispersion of the terahertz hole array sample. (c) 3D schematic of the unit cell used in numerical modelling.

crowave measurements. A splitting of the surface waves into symmetric and antisymmetric modes is observed; a behaviour analogous to that of surface plasmons in thin metallic films at optical frequencies [198].

7.1 Theoretical formalism

7.1.1 Modal matching approach

A rigorous modal matching method will allow for an easier interpretation of the electromagnetic response of open ended hole arrays, resulting in an understanding of the

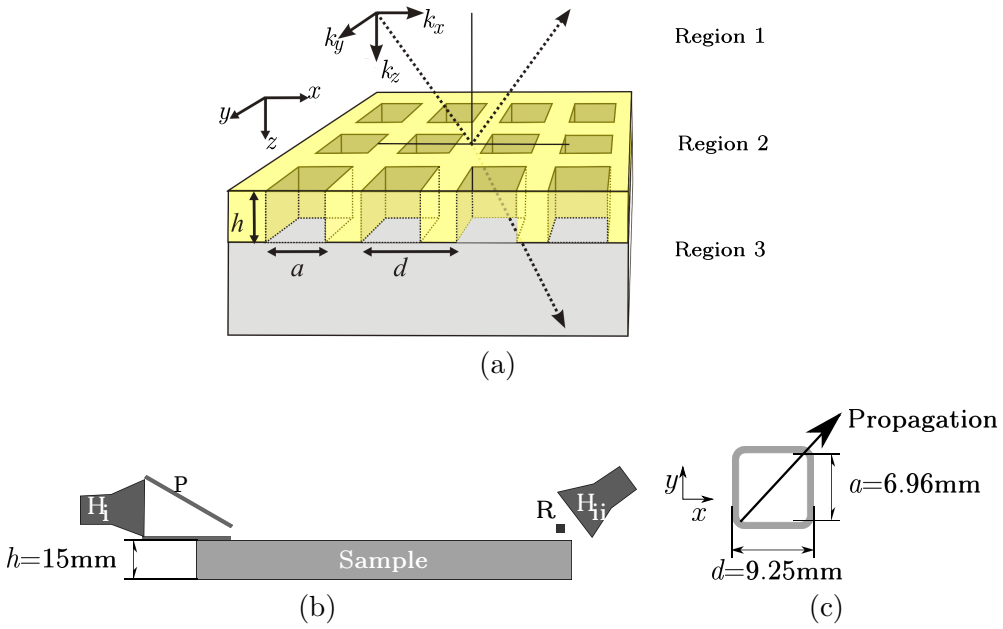

Figure 7.2: (a) Two dimensional, periodic array of square holes in a perfect conductor. The holes considered here are of depth h, side a, separated by distance d and filled by dielectric material with ϵ_h, while the substrate (region 3) is defined by material with dielectric constant ϵ_{sub}. (b) A schematic side view of the experiment: a microwave horn H_i is directed into a wedge waveguide, P. A second horn H_{ii}, is directed at a metal rod, R, $\approx$ 3 mm above the sample, which scatters power from the surface. (c) The unit cell of the sample used in the experiments. The arrow indicates the direction of propagation measured in the experiments.

properties of supported surface waves. This in turn can lead to the physical origins of the phenomena being explained. Sub-wavelength hole arrays in metals at low frequencies (such as the terahertz range and below) have previously been modelled using modal-matching techniques [184, 199, 200]. In brief, this technique works by matching the electromagnetic fields in the superstrate (assumed here to be air) and substrate to the fields of the waveguide modes inside the subwavelength holes [201]. By exploiting continuity of electric and magnetic fields at the boundaries, explicit analytical expressions for transmission and reflection of a square array (period d) of square holes (side a) in a thin metallic sheet of thickness h can be obtained. Allowing for specific mathematical terms to be manipulated and their relationship to the observed phenomena to be probed. Below, the formalism for this is developed based on earlier work [184, 200].

Begin by defining expressions for the electric and magnetic fields in the three regions of a hole array: in the incident vacuum region (superstrate), inside the holes, and in the substrate. For simplicity, note that in the following the time (t) dependent component

to the fields, $\approx \exp(i\omega t)$, where ω is the radial frequency, is omitted. Considering a unit source field incident as shown in fig. 7.2(a). Express the electric field on the incident side of the hole array (region 1) as a sum of the unit plane wave with wavevector, k_x, k_y, and k_z, and a two dimensional Fourier-Floquet expansion of diffracted orders with wavevectors, $k_x^{m_1,m_2}$, $k_y^{m_1,m_2}$, and $k_z^{m_1,m_2}$. Approximating the metal as a PEC, which is a reasonable approximation at terahertz and microwave frequencies as the field penetration into the metal is much smaller than the wavelength as shown in fig. 2.3. PEC materials have an infinite imaginary permittivity, and electric fields are therefore excluded. Therefore, the electric field inside the holes (region 2) is expressed by the fundamental mode of a square cavity of width a, while in the substrate (region 3) there is again a Fourier-Floquet expansion of diffracted orders. These definitions amount to x components of the form:

$$\begin{aligned} E_x^1 &= \exp(ik_x x + ik_y y + ik_z^{0,0} z) \\ &\quad + \sum_{m_1,m_2} r^{m_1,m_2} \psi_1^{m_1,m_2} \exp(-ik_z^{m_1,m_2} z), \end{aligned} \tag{7.1a}$$

$$\begin{aligned} E_x^2 &= \sum_{s_1,s_2} B^{s_1,s_2} \psi_2^{s_1,s_2} \exp(iq_z^{s_1,s_2} z) \\ &\quad - C^{s_1,s_2} \psi_2^{s_1,s_2} \exp(-iq_z^{s_1,s_2} z), \end{aligned} \tag{7.1b}$$

$$E_x^3 = \sum_{n_1,n_2} t^{n_1,n_2} \psi_1^{n_1,n_2} \exp(ik_z^{n_1,n_2}(z-h)), \tag{7.1c}$$

where $\psi_1^{m_1,m_2} = \exp\left(i(k_x + \frac{2m_1\pi}{d})x\right) \exp\left(i(k_y + \frac{2m_2\pi}{d})y\right)$ and $\psi_2^{s_1,s_2} = \sin\left(\frac{s_1\pi}{a}y\right) \cos\left(\frac{s_2\pi}{a}x\right)$. Note that similar expressions for y components of field can also be defined. Equation (7.1a) is made of two parts, the first exponential is due to free space incident wave, with the second term being a sum of the reflections from the hole array. The integer pairs (m_1, m_2) and (n_1, n_2) denote the diffracted orders, on the incident and substrate sides of the hole array, respectively, for a grating of pitch d. The factors r^{m_1,m_2} and t^{n_1,n_2} describe the coupled field reflection and transmission coefficients. The z component of the incident and transmitted wavevectors can be written as

$$k_z^{m_1,m_2} = \sqrt{k_0^2 - \left(k_x + \frac{2m_1\pi}{d}\right)^2 - \left(k_y + \frac{2m_2\pi}{d}\right)^2}, \tag{7.2a}$$

and

$$k_z^{n_1,n_2} = \sqrt{\epsilon_{sub}k_0^2 - \left(k_x + \frac{2m_1\pi}{d}\right)^2 - \left(k_y + \frac{2m_2\pi}{d}\right)^2}, \tag{7.2b}$$

where c is the speed of light, $k_0 = \omega/c$ is the wavenumber of the incident light and ϵ_{sub} is the dielectric constant of the material inside the substrate (region 3). The factors B^{s_1,s_2} and C^{s_1,s_2} describe the electric field amplitudes of the decaying wave in the cavity and the reflected wave from the cavity bottom, respectively, where the integer pair (s_1, s_2) define the waveguide mode within the cavity. It should be noted, that though the formalism is explicitly developed here for square holes, it is relatively straight forward to consider other waveguide shapes with different explicit forms of $\psi_2^{s_1,s_2}$, the infinite waveguide modes, used here as a matching condition for the overlap integrals. For square holes, the propagation constant in the cavity is

$$q_z^{s_1,s_2} = \sqrt{\epsilon_h k_0^2 - \left(\frac{s_1\pi}{a}\right)^2 - \left(\frac{s_2\pi}{a}\right)^2}, \tag{7.3}$$

where ϵ_h is the dielectric constant of the material inside the cavity.

The z components of the electric field can be found for the three regions, and subsequently expressions for the magnetic field $\mathbf{H}$, through the free space Maxwell's relations $\nabla \cdot \mathbf{E} = \mathbf{0}$ and $\nabla \times \mathbf{E} = -\mu_0 \delta\mathbf{H}/\delta t$. This gives the x and y components of the electric and magnetic fields in all regions in terms of the set of unknowns r, t, B and C. In order to eliminate some of these unknowns, boundary conditions can be applied, the x and y (tangential) components of the electric field must be continuous at the vacuum-sample interfaces (i.e. $z = 0$ and $z = h$, where h is the depth of the hole array) over the entire unit cell, while the magnetic field components are continuous only at the hole aperture. Matching the E fields in regions 1 and 2 at $z = 0$, and in regions 2 and 3 at $z = h$, (i.e. multiplying by ψ_1^* and integrating over x and y from 0 to d), and taking into account the orthogonality of the eigenmodes of the system, yields sets of continuity equations of the form

$$(\delta^{m_1,m_2} + r^{m_1,m_2})d^2 = \sum_{s_1,s_2} (B^{s_1,s_2} - C^{s_1,s_2}) Q_1^{m_1,m_2,s_1,s_2}, \tag{7.4a}$$

$$t^{n_1,n_2}d^2 = \sum_{s_1,s_2} (B^{s_1,s_2} e^{iq_z^{s_1,s_2}h} - C^{s_1,s_2} e^{-iq_z^{s_1,s_2}h}) Q_1^{n_1,n_2,s_1,s_2}, \tag{7.4b}$$

where

$$Q_1^{m_1,m_2,s_1,s_2} = \int_0^a \sin\left(\frac{s_1\pi y}{a}\right)\cos\left(\frac{s_2\pi x}{a}\right) \times \exp\left[-i\left(k_x + \frac{2m_1\pi}{d}\right)x\right]\exp\left[-i\left(k_y + \frac{2m_2\pi}{d}\right)y\right]dxdy, \tag{7.4c}$$

is the overlap integral between the diffracted order (m_1, m_2) and the waveguide mode (s_1, s_2) and δ^{m_1,m_2} represents the Kronecker delta function $\delta m_1 \delta m_2$. Separate expressions for the continuity of the y components of electric field can be obtained. These equations define how the fields from one region overlap the fields from the other region.

To obtain a further set of equations, consider the continuity of the $\vec{H}$ field over the holes at $z = 0$ and $z = h$, respectively, i.e. by multiplying $\vec{H}$ by ψ_2, and integrating from 0 to a for x and y. This gives a set of equations containing a second overlap integral:

$$Q_2^{m_1,m_2,s_1,s_2} = \int_0^a \sin\left(\frac{s_1\pi y}{a}\right)\cos\left(\frac{s_2\pi x}{a}\right) \times \exp\left[+i\left(k_x + \frac{2m_1\pi}{d}\right)x\right]\exp\left[+i\left(k_y + \frac{2m_2\pi}{d}\right)y\right]dxdy. \tag{7.4d}$$

These equations, relating x and y components of the electric and magnetic fields, define a complete set of equations describing the components of the fields in terms of the unknown sets $r^{m_1,m_2}, t^{n_1,n_2}, B^{s_1,s_2}$ and C^{s_1,s_2}. The number of equations present in the set depends on the number of diffracted orders and waveguide modes included in the calculation, but the system of equations is always uniquely defined (i.e. the number of unknowns equals the number of equations). For a rigorous solution to the system of equations, a high number of diffraction orders and waveguide modes must be included. It is then straight forward, if rather laborious, to solve the continuity equations, eliminating the coefficients B^{s_1,s_2} and C^{s_1,s_2}, to obtain the complex reflection and transmission coefficients, r^{m_1,m_2} and t^{n_1,n_2}. It should be noted that the continuity equations can also be solved eliminating r^{m_1,m_2} and t^{n_1,n_2} to find the field equations B^{s_1,s_2} and C^{s_1,s_2}.

7.1.2 Dispersion relations

In order to satisfactorily separate the diffractive effects (photonic band gap) from the dispersion of a spoof plasmon, it is necessary to study effects far from the Brillouin zone boundary (at $k_x = \pi/d$). In the experiments (section 7.2.1) this is achieved by studying

surface modes in the (1,1) direction of the unit cell. It is therefore appropriate to derive the dispersion relations of the surface modes propagating in this direction (i.e. with $k_x = k_y$ and $E_x = E_y$) and for now restrict the discussion to the dispersion when both regions 1 and 3 are air (i.e. $\epsilon_{sub} = 1$). For such circumstances, the Fourier components of the fields in regions 1 and 3 have mode wavevector in the z direction which can be written as

$$k_z^{m_1,m_2} = \sqrt{k_0^2 - \left(\frac{k_\parallel}{\sqrt{2}} + \frac{2m_1\pi}{d}\right)^2 - \left(\frac{k_\parallel}{\sqrt{2}} + \frac{2m_2\pi}{d}\right)^2}, \tag{7.5}$$

where $k_\parallel$ is the component of the wavevector parallel to the surface.

Even while restricting the system to surface modes in the (1,1) direction, a solution including large numbers of diffracted orders and waveguide modes must be found numerically. However, there are a number of simplifications commonly applied in modal matching which can drastically reduce the complexity of the problem and make an analytical solution possible. The simplifications will firstly be introduced, and their validity discussed thereafter. The simplest solution can be limited to considering only the first order waveguide mode ($s_1 = 1, s_2 = 0$) in the cavity and specular reflection/transmission ($m_1 = m_2 = n_1 = n_2 = 0$). This is the approximation used by Pendry et al. [182] and Garcia-Vidal et al. [183] to derive analytical dispersion relations for spoof surface plasmons on dimpled conducting surfaces. The approximation is valid only in the limit $a \ll d \ll \lambda_0$, where λ_0 is the vacuum wavelength. Then, the summations in, (7.4a), (7.4b) and those in the continuity equations for magnetic fields, are removed. This allows for the easy solving of the continuity equations, eliminating the coefficients $B^{1,0}$ and $C^{1,0}$. The transmission coefficient found is

$$t^{0,0} = -\frac{2q_z^{1,0}k_0^2}{k_z}\frac{a^2}{d^2}\frac{Q_1^{0,0,1,0}Q_2^{0,0,1,0}}{\exp(iq_z^{1,0}h)\left(F - \frac{a^2q_z^{1,0}}{2}\right)^2 - \exp(-iq_z^{1,0}h)\left(F + \frac{a^2q_z^{1,0}}{2}\right)^2}, \tag{7.6a}$$

where

$$F = \frac{Q_1^{0,0,1,0}Q_2^{0,0,1,0}}{d^2}\left(\frac{k_0^2}{k_z^{0,0}}\right). \tag{7.6b}$$

From this solution, the dispersion of surface modes can be inferred, given by the poles in transmission:

$$\exp(iq_z^{1,0}h)\left(F - \frac{a^2q_z^{1,0}}{2}\right)^2 - \exp(-iq_z^{1,0}h)\left(F + \frac{a^2q_z^{1,0}}{2}\right)^2 = 0. \tag{7.6c}$$

It should be noted that as the hole depth is increased to infinity the dispersion

relation for spoof plasmons in arrays with infinitely deep, square holes, found by Pendry et al. $F = \frac{a^2 q_z^{1,0}}{2}$, is precisely recovered from (7.6c) [182, 183].

Near the cut-off frequency of the cavities, it can be qualitatively argued that considering only the lowest order TE waveguide mode (i.e. $s_1 = 1, s_2 = 0$) is a reasonable assumption: the higher order waveguide modes with the correct symmetry are very strongly evanescent (i.e. in (7.3), $q_z^{s,t}$ is large and imaginary) and will therefore have little effect on the surface mode dispersion. However, numerical (using finite element method [195], modal expansion [182] and finite time domain [183]) and analytical (modal matching [184]) modelling has shown that hole period can be particularly critical in determining the precise dispersion relation of the surface mode supported by these samples. This is because diffracted evanescent waves change the boundary conditions at the entrance and exit of the cavities. It has been shown for dimpled surfaces that including higher diffraction orders while describing the fields inside the cavities using only the first order waveguide mode provides an accurate dispersion relation [184]. For the holey metal layers discussed here, this approximation gives the transmission coefficient

$$t^{m_1,m_2} = -\frac{2q_z^{1,0}k_0^2}{k_z}\frac{a^2}{d^2}\frac{Q_1^{m_1,m_2,1,0}Q_2^{0,0,1,0}}{\zeta}, \tag{7.7a}$$

where

$$\begin{aligned}\zeta =& \exp(iq_z^{1,0}h)\left(\sum_{m_1,m_2} F^{m_1,m_2} - \frac{a^2 q_z^{1,0}}{2}\right)^2 \\ &- \exp(-iq_z^{1,0}h)\left(\sum_{m_1,m_2} F^{m_1,m_2} + \frac{a^2 q_z^{1,0}}{2}\right)^2,\end{aligned}$$

and

$$F^{m_1,m_2} = \frac{Q_1^{m_1,m_2,1,0}Q_2^{0,0,1,0}}{d^2}\left(\frac{k_0^2 + (\frac{K_\parallel}{\sqrt{2}} + \frac{2m_1\pi}{d})(\frac{2m_2\pi}{d} - \frac{2m_1\pi}{d})}{k_z^{m_1,m_2}}\right), \tag{7.7b}$$

with surface mode dispersion given by

$$\begin{aligned}&\exp(iq_z^{1,0}h)\left(\sum_{m_1,m_2} F^{m_1,m_2} - \frac{a^2 q_z^{1,0}}{2}\right)^2 \\ &- \exp(-iq_z^{1,0}h)\left(\sum_{m_1,m_2} F^{m_1,m_2} + \frac{a^2 q_z^{1,0}}{2}\right)^2 = 0.\end{aligned} \tag{7.7c}$$

The summations over the integer diffracted orders are typically carried out for $m_1 = -1, 0, +1$ and $m_2 = -1, 0, +1$ as in [184].

It should be noted that the modal matching solutions presented above are only strictly valid for frequencies well below the cut-off frequency of the second order waveguide mode.

7.2 Results and discussion

7.2.1 Measurement of surface mode dispersion

In order to validate the dispersion relations derived in the previous section, the surface modes supported by open hole array structures have been measured in the microwave frequency region.

To experimentally observe the dispersion of these surface waves, a closed packed array of hollow, square-ended brass tubes, with side length $d = 9.25$mm, inner length $a = 6.96$mm and height $h = 15$mm is used, similar to that presented in [190]. The cut off frequency of the holes is defined as, $\omega_{co} = \frac{\pi c}{a\sqrt{\epsilon_h}}$, where ϵ_h is the dielectric constant of the material inside the tubes. It is desirable to observe the surface modes unperturbed by effects due to the Brillouin zone boundary, therefore it is required that ω_{co} is far below the diffraction edge associated with the sample. In this case the diffraction edge in the (1,0) direction occurs at 17.7 GHz. To first minimise the effects of the proximity of the Brillouin zone boundary the holes are filled with dielectric material ($\epsilon_h = 2.29$), giving a cut-off frequency of 14.4 GHz for the cavities in the sample. Since this is close to the (1,0) diffraction edge of the sample, it would be expected that the dispersion of surface modes in the (1,0) direction is strongly perturbed by the band gap at the Brillouin zone boundary. In experiment, the measurement is therefore taken in the diagonal of the unit cell (i.e. $k_y = k_x$); the diffraction edge in the (1,1) direction is 22.3 GHz, significantly greater than the cut-off frequency of the holes, thereby reducing the perturbation due to diffraction. This perturbation is discussed in more depth in section 7.2.2.

As discussed in chapter 3 there are several methods by which the dispersion of surface modes can be observed. Prism coupling usually only allows for coupling only to antisymmetric surface waves (i.e. modes where the fields do not exhibit mirror symmetry in the plane of the sample), whereas, coupling to a surface mode via a grating typically leads to significant distortion of the dispersion [198]. To avoid these drawbacks, a blade coupling method, similar to that discussed in 2.1.3 at microwave frequencies, is used with a vector network analyser (VNA) with broadband (10 $\rightarrow$ 50 GHz) microwave horns. A VNA uses a frequency mixing method to measure the

relative phase of the measured radiation [202]. Fig. 7.2(b) shows the experimental set-up used. At 'i' in fig. 7.2(b) a horn is directed into a vertically tappered waveguide with a 5 mm exit aperture, the first 'blade'. At 'ii', a horn is directed towards a long thin metallic rod positioned 3 mm above the sample surface, the second 'blade'. The height of this rod can be varied to modify the coupling efficiency to each of the surface modes of the sample.

The dispersion is obtained from phase measurements of a propagating surface wave. The difference in phase between two surface waves ($\Delta\phi$) is related to the difference in the in-plane wavevector component ($\Delta k_{\|}$)) through the simple relation

$$\omega = \frac{d\phi}{dt} = \frac{2\pi c_{sw}}{\lambda} \quad \Rightarrow \quad \Delta k_{\|} = \frac{\Delta\phi}{L}, \tag{7.8}$$

where c_{sw} is the speed of the surface wave, and L is the propagation length from the source. This is the same as (3.9) used to find the dispersion relation from eigenmode solutions discussed in section 3.4. In these experiments, a propagation length of 30 cm was used. To obtain the absolute magnitude of the in-plane wavevector component, a reference measurement is required. The measured sample phase is compared to the phase of a surface wave on a planer metal sheet (which is assumed to possess a surface mode propagating at the speed of light in vacuum). Taking the phase difference between these two measurements and dividing by the propagation length gives $\Delta k_{\|}$ from a free space wave, represented by the light line in figures 7.3 → 7.7, and therefore yields a dispersion curve. The dispersion curves for the open ended hole array (i.e. $\epsilon_{sub} = 1$) are shown in fig. 7.3(a), the circles are extracted from the measured phase information as described above. Surfaces modes are clearly observed in the frequency range of interest. However, it should be noted that the measured dispersion for a higher frequency surface mode (triangles) is obtained in a non-rigorous manner, by assuming the onset of this mode occurs at the lightline for frequencies above the asymptotic frequency of the lower frequency mode. Despite this assumption, both of these modes exhibit good agreement with the analytical model from (7.7c) (solid curved lines). Fig. 7.4 shows the measured transmission across (not through) the sample, this spectrum is complicated and difficult to analyse when compared to the measured phase information. This is due to the difficulty of normalising the signal. The reference transmission is very small due to the poorly defined mode across the metal sheet. This results in a poorly defined spectrum still including effects of the frequency dependence of the system.

Full numerical finite element method (FEM) modelling of the surface eigenmodes supported by the sample has also been conducted as described in section 3.4 [89]. The numerical modelling predicts surface mode dispersions which correlate extremely closely to those from the analytical model derived above (FEM modelling is shown as

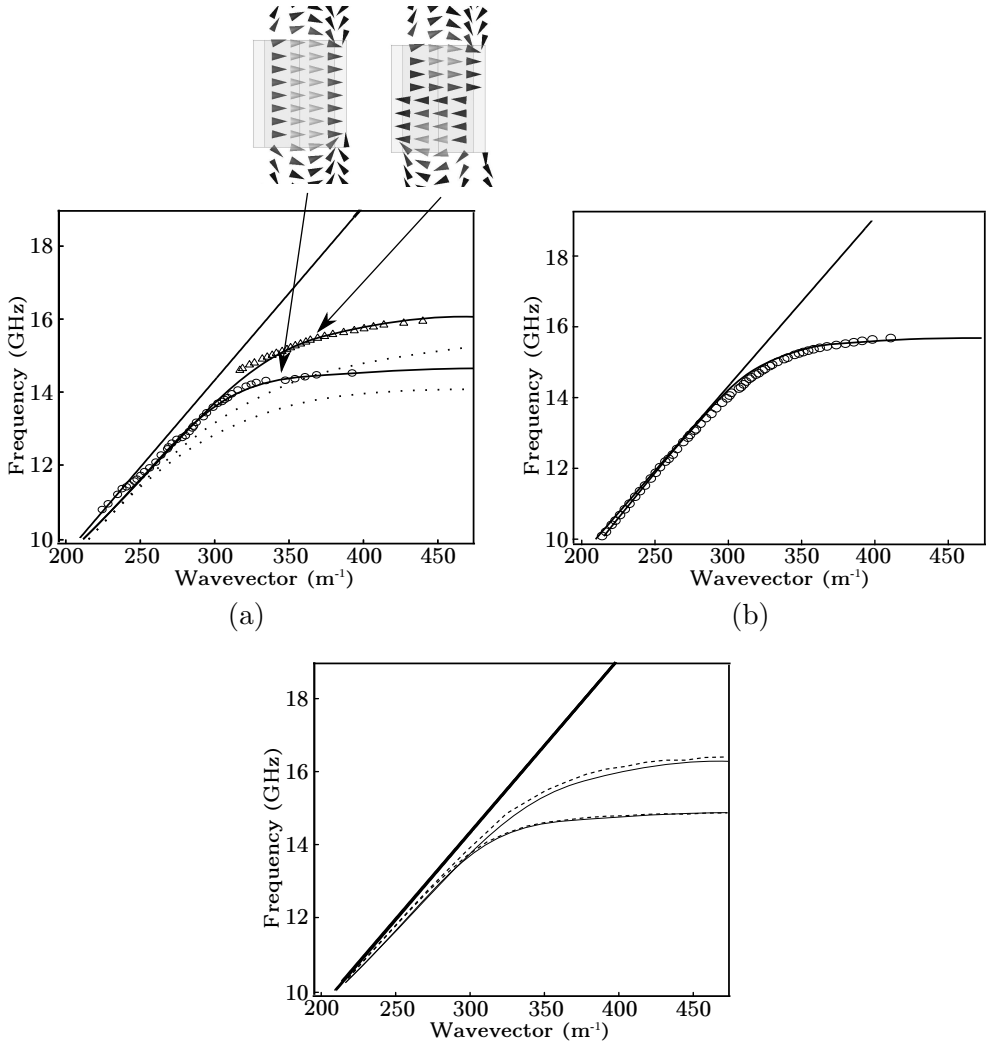

Figure 7.3: (a) Experimentally determined spoof surface plasmon dispersion curves (circles and triangles) compared to the analytical models (solid curved lines), for an open ended hole array defined by $d = 9.25$ mm, $a = 6.96$ mm, $h = 15$ mm, $\epsilon_h = 2.29$). For an open ended hole array (i.e. $\epsilon_{sub} = 1$), one observes both low frequency (symmetric) and higher frequency (antisymmetric) modes. In the inset the arrows indicate the electric field profiles calculated using the finite element method (FEM) [89]. These show the direction of the electric fields inside the hole for a particular phase (with the lighter colour indicating a strong electric field) highlighting the symmetric and antisymmetric nature of the two surface modes. The dotted line in this figure shows the analytical results for both modes when diffracted orders are not taken into account. (b) For a dimpled surface array (i.e. perfect metal with $\epsilon_{sub} = i\infty$) with the same parameters as the open hole case, only one surface wave is observed, with an assymptoptic frequency higher than the cut-off frequency of the holes (see text). The experimental data is shown as the circles and the analytical model as the curved solid line. (c) Comparison between analytical (solid lines) and numerical (FEM, dashed lines) [89] models. The straight solid line represents the vacuum light line.

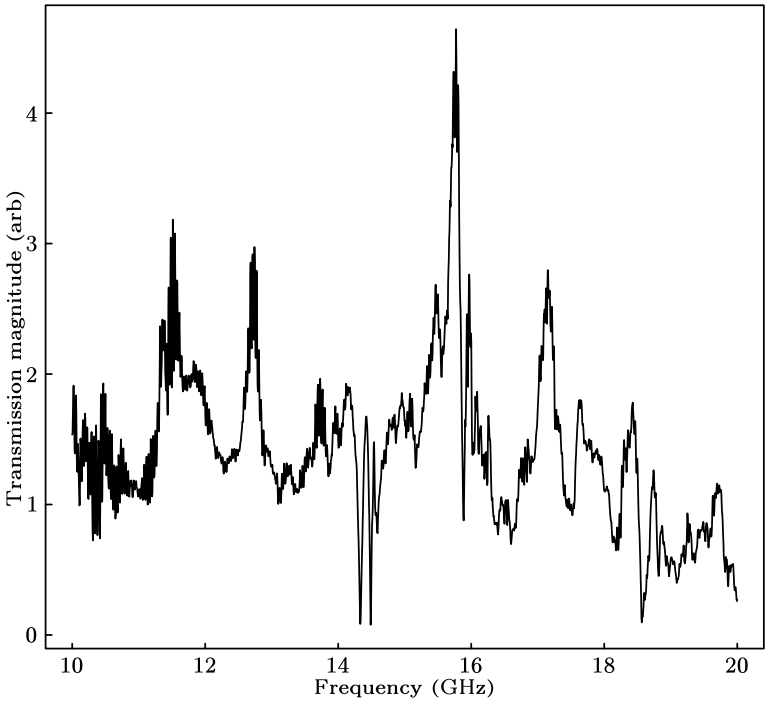

Figure 7.4: The transmission measured across the surface of an array of open ended square holes defined by $d = 9.25$mm, $a = 6.96$mm, $h = 15$mm, and $\epsilon_h = 2.29$, normalised against the transmission across a flat metal surface.

the dashed line in fig. 7.3(c), while the analytical model is represented by the solid line). Field distributions associated with each surface mode can also be obtained: the boxes above fig. 7.3(a) show the electric fields inside the hole region, with the direction of the electric field represented at the same point in phase cycle. These show the low frequency mode as having a symmetric electric field distribution while the higher frequency mode has an antisymmetric distribution. Numerical modelling has also been conducted for square holes with rounded corners similar to that of the real sample, this shows no measurable difference to the dispersion with square holes.

The splitting of the surface mode into symmetric and antisymmetric modes is very reminiscent of the behaviour of surface plasmons in thin metallic films at optical frequencies [23]. However, such splitting is not observed for the surface modes on dimpled surfaces (i.e. with closed holes, where region 3 is a perfect metal with $\epsilon_{sub} = i\infty$) considered in [183, 184, 187, 189–191]. The dispersion of the spoof plasmon measured on a dimpled surface with the same dimensions as the hole array is shown in fig. 7.3(b). The measurements are compared to the analytical modal matching solution for a dimpled surface from [184]. For both the measurement and the analytical model only one spoof plasmon mode asymptotically diverging from the light line is observed. This behaviour

arises due to the boundary conditions between region 2 and 3, which, for closed holes, forces the transverse component of the electric field to zero at this interface. For open holes this restriction is lifted, and a node can appear in the middle of the holes ($z = \frac{h}{2}$): this is the defining feature of antisymmetric surface mode of the open hole arrays.

In addition to the mode splitting, which appears for the open holes and is absent from closed holes, there is a clear difference in the asymptotic frequencies of the dispersions for the two cases. This is addressed in the next section.

7.2.2 Asymptotic frequencies and mode splitting

For the simplest modal matching solution, i.e. considering only the *first order waveguide mode* ($s_1 = 1, s_2 = 0$) in the cavity and *specular reflection/transmission* ($m_1 = m_2 = n_1 = n_2 = 0$), the dispersion relation from (7.6c) is obtained. From this simplified form of the dispersion relation, the asymptotic frequencies for dispersion of the surface waves can easily be obtained. The lowest frequency asymptote is given by the cut-off frequency of the holes, $\omega_{co} = \frac{\pi c}{a\sqrt{\epsilon_h}}$. It should be noted that, in contrast to the spoof surface plasmon of dimpled metal surfaces [184], the asymptotic frequency of the lowest frequency surface mode in these hole arrays is *independent of hole depth*. This behavior can be seen in the low frequency dispersion of a thicker hole array ($h = 40$mm, solid curves in fig. 7.5(a)), which displays the same asymptotic frequency as the sample ($h = 15$mm, dashed curves in fig. 7.5(a)). However, for the higher order antisymmetric mode as thickness increases the asymptotic frequency decreases.

In addition to the two spoof surface plasmons, for structures with larger h (fig. 7.5(a)) several higher order modes which do not asymptote to the light line are observed. Indeed, this is actually a complete family of surface modes with asymptotic frequencies derived from the condition $q_z^{1,0} h = 0$, i.e. with asymptotic frequencies, ω_{as}, given by

$$\omega_{as} = \omega_{co}, \sqrt{\omega_{co}^2 + \left(\frac{\pi c}{h\sqrt{\epsilon_h}}\right)^2}, \sqrt{\omega_{co}^2 + 2\left(\frac{\pi c}{h\sqrt{\epsilon_h}}\right)^2} \ldots \tag{7.9}$$

Since $k_x > k_0$, all modes exhibit fields which are evanescent in regions 1 and 3, above and below the hole array, similar to that observed in surface plasmons in 2.1, and so can be termed surface modes. However, the fields inside the holes distinguish each of the modes: the lowest frequency mode, defined by the asymptote at the cut-off frequency of the holes exhibits electric fields inside the hole which are hyperbolic and symmetric. Though not explicitly shown here, it is straight forward to solve the continuity equations for the factors B and C which determine the electric field profiles. The second lowest frequency mode, with an asymptotic frequency at $\sqrt{\omega_{co}^2 + \left(\frac{\pi c}{h\sqrt{\epsilon_h}}\right)^2}$, exhibits a node in the electric field in the middle of the hole (see inset of fig. 7.3(a)). The fields of

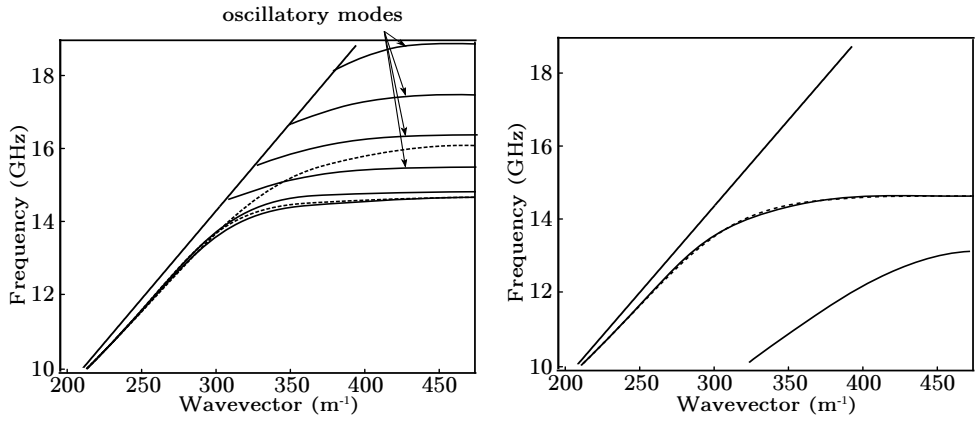

Figure 7.5: (a) Surface mode dispersion for larger array thickness $h = 40$ mm. The asymptotic frequency of the symmetric mode remains relatively unchanged, while the asymptotic frequency of the antisymmetric mode has reduced in frequency. In addition, one observes the surface modes associated with the higher frequency waveguide modes, marked with arrows. (b) The effect of introducing a substrate (region 3) with non-unity dielectric constant, $\epsilon_{sub} = \epsilon_h = 2.29$ is to split the surface mode, with each mode following a different light line associated with the material on each interface. The dashed lines in both figures show the dispersion for the measured sample (defined by $d = 9.25$mm, $a = 6.96$mm, $h = 15$mm, $\epsilon_h = 2.29$ and $\epsilon_{sub} = 1$).

this mode are hyperbolic and *antisymmetric* in form for frequencies below ω_{co}. These two lowest order modes are reminiscent of the symmetric and antisymmetric surface plasmons in thin metal films [23], and are therefore labelled here as the "spoof plasmon" modes of the hole array. Similar to the behaviour of symmetric and antisymmetric surface plasmons, both the symmetric and antisymmetric spoof plasmon modes have dispersion which is asymptotic to the light line.

The fields inside the hole for the higher order modes are oscillatory in nature (labelled "oscillatory modes" here), with field maxima at the hole entrance and exit plus two or more nodes. The oscillatory fields inside the holes are below their asymptotic frequencies, these modes exist only in the frequency domain $\omega > \omega_{co}$, and are therefore not asymptotic to the light line. When the depth of the holes is increased (fig. 7.5(a)) one observes a reduction in the asymptotic frequencies of these modes. For infinitely deep holes, the asymptotic frequencies of these modes converge onto that of the symmetric spoof surface plasmon mode.

Above, the surface mode dispersion is discussed in its very simplest form by considering only specular reflection and transmission mediated by the first order waveguide modes of the hole array. However, numerical (using finite element method [195], modal

expansion [182] and finite time domain [183]) and analytical (modal matching [184]) modelling has shown that diffracted evanescent waves can be crucial to obtain an accurate dispersion relation [184]. In fig. 7.3(a) for the dimensions of the measured hole arrays, the measured dispersion (symbols) to the dispersion relations from (7.6c) and (7.7c) are compared (excluding and including evanescent diffracted orders, respectively). Clearly the important role that evanescent diffracted fields play in determining surface mode dispersion can be seen. These higher order Fourier components of the electromagnetic fields not only perturb the frequency dependence of the dispersion, but also lead to slightly higher asymptotic frequencies than predicted by (7.9). This behaviour has previously been observed for spoof surface plasmons on dimpled metal surfaces [184], and is related to a modification by the evanescent diffracted fields of the boundary conditions at the entrance and exit of the cavities (which in turn perturbs the quantization of the field inside the holes).

Increasing the pitch of the array while holding the other parameters constant, reducing Brillouin zone boundary wavevector. The effects of the Brillouin zone boundary can be observed. Fig. 7.6 shows the dispersion for $d = 15$mm (solid curved line) and $d = 9.25$mm (dashed curved lines) when $a = 6.96$mm, $h = 15$mm, and $\epsilon_h = 2.29$. The zone boundary for $d = 15$mm at the pinnacle of the curve, perturbs the dispersion to such an extent that the antisymmetric mode is no longer distinguishable from the symmetric, the asymptotic frequency is also highly modified. It is apparent from this why it is desirable to observe these modes far from the Brillouin zone boundary.

In addition to the diffracted fields, surface mode dispersion is also perturbed by the presence of a substrate. In figure 7.5(b), the dispersion for a structure with a dielectric substrate ($\epsilon_{sub} = \epsilon_h = 2.29$ in region 3) is shown as a solid line. The presence of a substrate results in a further splitting of the symmetric and antisymmetric spoof surface plasmons. The lower frequency mode asymptotes to the light line in a material of ϵ_{sub}, while the higher frequency mode asymptotes to the vacuum light line. This behaviour is again reminiscent of surface plasmons in thin metallic films on a dielectric substrate [23]. FEM modelling shows that the electric fields are strongest in the dielectric to which their mode is associated.

7.3 Role of surface modes in hole arrray transmission

7.3.1 Near field transmission of hole arrays

Discovered originally by Pendry [192], an interesting property of surface plasmons is their ability to focus light to spots smaller than the diffraction limit for light, an effect referred to as superlensing. The simplest form of a superlens consists of a metallic

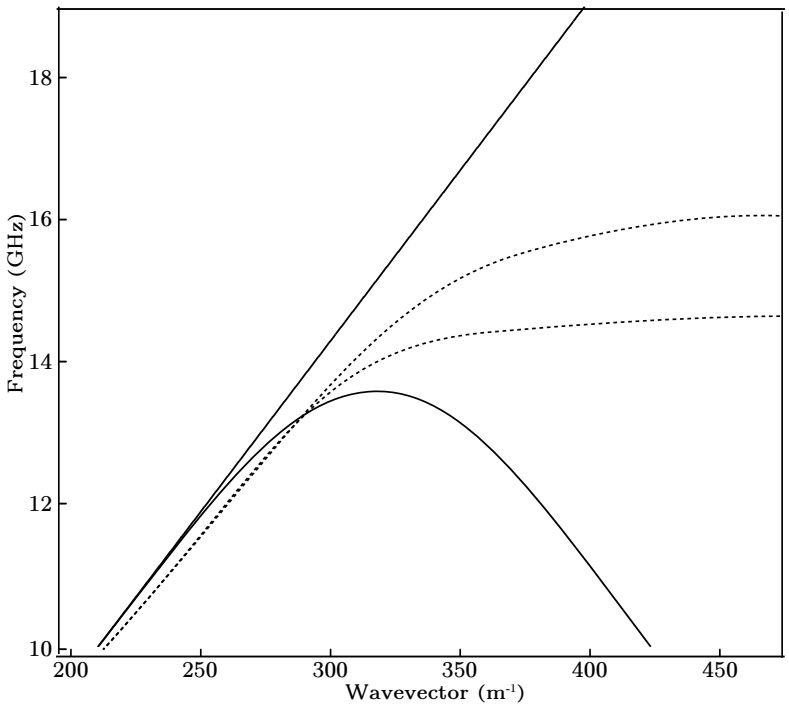

Figure 7.6: Dispersion relations for an open ended hole array defined by $a = 6.96$mm, $h = 15$mm, and $\epsilon_h = 2.29$ when $d = 15$mm (solid curved line) and $d = 9.25$mm (dashed curved lines).

film which exhibits superlensing effects near the surface plasmon resonance condition in the near ultraviolet frequency region [193–195]. This effect occurs when a near field source of radiation couples to the symmetric surface plasmon of a thin metal film. An important question to answer is therefore: can a symmetric spoof surface plasmon exhibit similar superlensing properties?

The electromagnetic fields scattered by an object may be represented by a Fourier sum. In order to form a perfect image from the field scattered by an object, all Fourier components of the field in an image plane must be restored. However, Fourier components associated with the large lateral wavevectors $k_{\|}$ satisfying $|k_{\|}| > |k_0|$ give rise to evanescent waves which have imaginary values for k_z. These near field components are confined to the subwavelength vicinity of the object. Hence, it is usual when using a normal lens to only capture wavevectors satisfying the condition $|k_{parallel}| < |k_0|$, limiting the resolution of image formation to approximately the wavelength of light. In the last decade it has, however, become clear that it is possible to design superlenses which can restore at least some of these near field components, allowing subwavelength resolution in images [192]. In this section, the transmission of near fields of the hole

arrays within the analytical formalism from section 7.1 is considered. Below it is shown that spoof surface plasmons play an important role in determining the near field transmission characteristics of a hole array.

Ignoring the effects of diffraction for now, the field transmission function of interest is given by (7.6a). In general, the transmission function introduces some perturbations of the fields which are dependent on $k_{\|}$. However, for frequencies near the surface mode resonances given by (7.9), the conditions $e^{iq_z h} \approx 1$ and $e^{-iq_z h} \approx 0$ apply, and (7.6a) simplfies to $t^{0,0} \to 1$ for $k_{\|} \to \infty$. This means that, in the absence of diffraction, near fields defined by large lateral wavevectors will be perfectly transmitted through a hole array. This effect has recently been pointed out by Jung et al. [203], who described hole array structures as "perfect endoscopes", i.e. structures which are capable of perfectly transforming a source of field from the input to output surfaces without losses, while maintaining subwavelength resolution. This interesting property occurs for an array of *any* hole depth, i.e. input fields can be transferred to the output interface of a hole array over an arbitararily large distance.

In practice, perfect transmission will not be achieved due to the effects of diffraction. Including diffracted orders, the relevant transmission is given by (7.7a). For frequencies near to ω_{co} (i.e. where the condition $q_z^{1,0} h \approx 0$ applies), (7.7a) simplifies to $t^{0,0} \approx F^{0,0} / \sum m_1, m_2 F^{m_1,m_2}$. This results in perfect transmission only for $|F^{0,0}| >> |F^{m_1,m_2}|$, i.e. when $|k_z^{0,0}| << |k_z^{m_1,m_2}|$. Hence, the Brillouin zone boundary sets a limit for transmission of evanescent fields to those with $|k_{\|}| < \frac{2\pi}{d}$ (see (7.5)). this is in agreement with the numerical modelling of Jung et al. [203], who found that resoluton of their hole array endoscope is limited by the periodicity of the array.

However, it should be noted that a "perfect endoscope" is not the same as a "perfect lens" [192]. For a plasmonic metal film at the surface plasmon frequency, it is straight forward to show that the thin film transmission $t \to \exp(-ik_z h)$ for $k_{\|} \to \infty$ [192]. Therefore, for evanescent field components with imaginary k_z, the fields are effectively amplified on transmission through the metallic film. This highlights one of the fundamental differences between a surface plasmon and a spoof surface plasmon: while surface plasmons in metallic films can give rise to lensing effects for evanescent fields, spoof surface plasmons in hole arrays *cannot* give rise to such effects. This difference is due to the nature of the fields inside the materials: at their asymptotic frequency, surface plasmons exhibit fields inside the metal which are evanescent in nature as described in 2.1. At the asymptotic cut-off frequency of a symmetric spoof surface plasmon, meanwhile, the fields inside the cavities lose their evanescent character. Hence, no amplification of near fields is possible for spoof surface plasmons. Since spoof surface plasmons have very different near field characteristics to surface plasmons, the term "spoof surface plasmon" may be something of a misnomer. However,

note that superfocussing at microwave and THz frequencies may still be possible with semiconductor surface plasmons [36].

7.3.2 Far field transmission of hole arrays

Recent interest in the enhanced optical transmission through arrays of sub-wavelength holes in metal films was sparked by the seminal work of Ebbesen et al. [3], who observed peaks in transmission at wavelengths close to the lattice periodicity. Since this visible-frequency observation of enhanced optical transmission through hole arrays, similar effects have been observed at infrared [204], terahertz [205–209], and microwave frequencies [210, 211], with applications suggested in designing filters [212] optical sensors,[213], microwave devices [214] and THz optical components [215].

Since the first experimental observations, consensus has been gradually developing that surface modes (surface plasmons at optical frequencies) play a crucial role in enhanced optical transmission. In this respect, perhaps the most physically insightful model applied to hole arrays has been the 'Fano-type' mechanism [196, 216]: in this picture, transmission is interpreted in terms of the interference between two transmission channels: one non-resonant (direct) channel describes transmission through individual, uncoupled holes whilst the resonant channel describes light which transverses the grating through adjacent holes via diffractive coupling to surface modes. Within this model, the origin of peaks in the transmission spectra of the hole-arrays can be understood in terms of constructive interference conditions, reached when the wavelength of the light is approximately equal to the spacing of the hole-array lattice. In this section the role that spoof surface plasmons play in this process is highlighted. The effects discussed below are entirely scalable with wavelength and array size: therefore it is appropriate to normalise all length scales by the period of the array d and normalise frequency and wavevector by the grating frequency and vector respectively:

$$\omega_{diff} = \frac{2\pi c}{d}, \; k_{diff} = \frac{2\pi}{d}. \tag{7.10}$$

For simplicity, the discussion is restricted to surface waves propagating in the (1,0) direction of the unit cell. Note that the evanescent surface modes, which strictly exist only in the region described by $k_x > k_0$, do not contribute to transmission in the far field. However, the influence of surface modes in the region $k_x < k_0$ can be considered by employing a reduced zone representation of surface modes. Briefly, the surface mode dispersions are found without any diffraction effects. Then, periodicity is introduced by adding and subtracting grating vector components of magnitude k_{diff} through $k'_x = k_x \pm m_1 k_{diff} \pm m_2 k_{diff}$. A similar approach is commonly employed to analyse the effects

of surface plasmons in optical gratings [217]. Note that the opening of band gaps near the Brillouin zone boundary is neglected, and so this approach should only be treated as approximate. In figs. 7.7(a) and (b), black lines represent mode wavevectors, k_x, in the absence of diffraction (from (7.6c)), while dashed lines represent k'_x under first order diffraction (i.e. $m_1 = 1, m_2 = 0$). In this reduced zone representation, for hole arrays defined by $\omega_{co} < \omega_{diff}$ (fig. 7.7(a)), a number of modes appear in the region $k_x < k_0$. Multimodal features in transmission are therefore expected. The two lowest frequency transmission features arise from diffractive coupling to the spoof plasmon surface modes, while the higher frequency features arise from coupling to the oscillatory modes of the cavity. Transmission spectra of these large hole structures can therefore be very complex, since many peaks associated with each diffraction order are expected. For hole arrays with $\omega_{co} > \omega_{diff}$ (fig. 7.7(b)), only the two lowest frequency modes below ω_{diff} are observed. This is because only symmetric and antisymmetric surface plasmon modes are asymptotic to the light line (as discussed in section 7.2.2). For such a structure bimodal features are expected in transmission.

Multimodal and bimodal behaviour can be observed in figs. 7.7(c) and (d), respectively. The transmission, calculated using (7.7a), is plotted as a function of hole height h for a large hole array with $a = 0.8d$, and a small hole array with $a = 0.4d$. For the array with large holes, the transmission typically contains several convoluted peaks, each associated with diffracted coupling to a different surface mode. As h decreases, higher order modes extend towards the light line and converge at $\omega/\omega_{diff} = 1$. the transmission resonances associated with these modes can become very narrow as dephasing decreases [196]. For the array with small holes, on the other hand, transmission is mediated only by diffractive coupling to the symmetric and antisymmetric surface plasmon modes. By tuning the hole size so that ω_{co} lies above or below ω_{diff}, one can therefore easily change from bimodal to multimodal transmission regimes. It is clear from fig. 7.7 that such simple structures can be specifically designed as either narrowband or broadband transmission filters with a relatively small change to structural dimensions.

7.4 Conclusions

Phase sensitive microwave experiments have been conducted to measure the dispersion of surface modes for a structure consisting of arrays of holes in a highly conducting sheet. Two separate surface modes were observed and shown to have field distributions analogous to the symmetric and antisymmetric surface plasmon modes found in thin metal films. In order to analyse the measurements, explicit analytical expressions for the transmission function of the hole arrays using a modal matching method has been

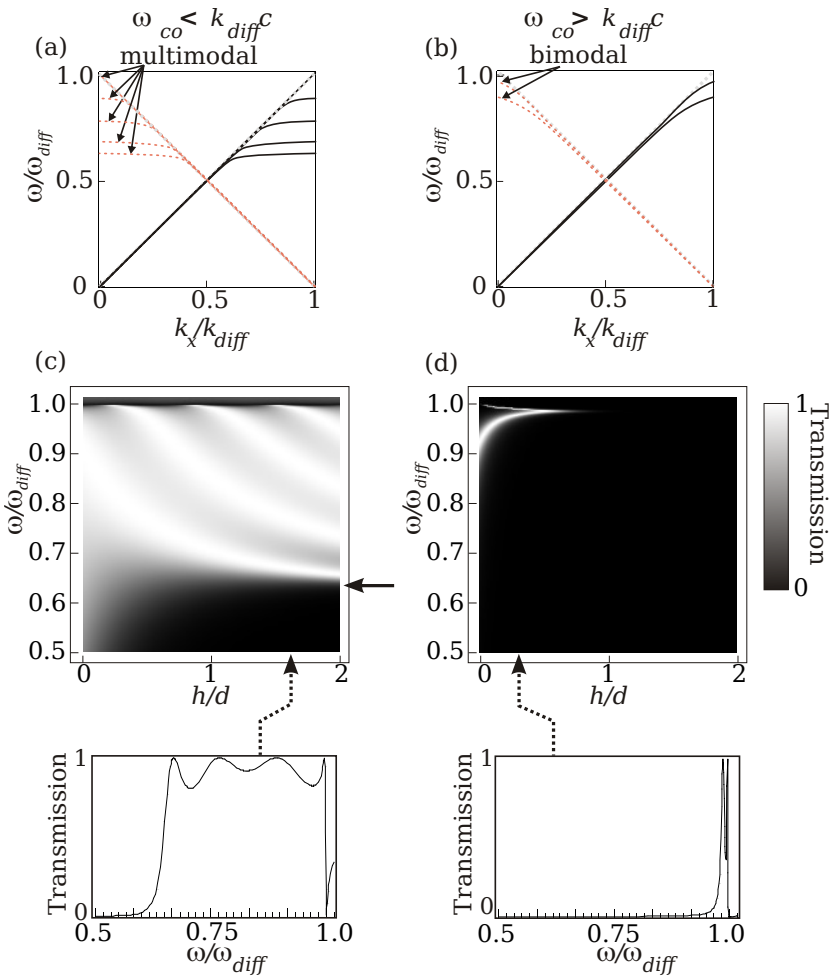

Figure 7.7: (a) Spoof surface mode dispersion relations in the reduced zone representation. For hole arrays defined by $\omega_{co} < \omega_{diff}$, a number of modes associated with each grating vector are observable in the 1st Brillouin zone. For hole arrays with $\omega_{co} > \omega_{diff}$ (b), only the first two (surface plasmon) modes are defined below cut-off. (c) Transmission as a function of hole height h for an array with dimensions $a = 0.8d$. One can clearly observe the multimodal transmission, with several peaks in the frequency region between the cut-off frequency (marked by a solid arrow) and $\omega = \omega_{diff}$. (d) Transmission as a function of hole height h for an array with dimensions $a = 0.4d$, showing the transmission mediated by the symmetric and antisymmetric surface plasmon modes. The lower panels show transmission spectra at heights indicated by dotted arrows. All calculations are for $\epsilon_h = 1$.

developed. The dispersion relations found from this approach have shown very close agreement to the measurements. The analytical functions are then used to analyse the role of these spoof surface plasmon modes in near and far field transmission of hole arrays. Spoof surface modes have been shown to play an important role in enhanced optical transmission, and elucidate the hole and depth behaviour in the transmission of such structures. In the near field transmission, the role these surface modes play in endoscopic transmission (the transfer of a field profile from the incident to output interfaces) is discussed, and the theoretical limit for near field spatial resolution is the period of the hole array is shown. However, superfocussing effects which are present for surface plasmons in metallic films have been shown to be absent for hole arrays, i.e. no amplification of near fields is possible for spoof surface plasmons. While many of the apparent properties of spoof surface plasmons resemble those of surface plasmons in thin metallic films, the analogy is therefore incomplete.

Chapter 8

Conclusions and future work

Throughout this thesis the interaction of electromagnetic radiation with materials has been probed using a range of experimental and theoretical methods. Very simple models were derived to explain the power dependency of generating terahertz radiation from arrays of particles (chapter 4). This simple model supported the propossed generation method of accelerated photoemitted electrons. It was also shown that the strength of the generated terahertz radiation depends on the field enhancements surrounding the nanoscale particles.

Finite element method modelling has been used to show that InSb particle plasmons should exhibit very strong photomodulations (chapter 6). This modelling has also shown that should well formed particles be fabricated at terahertz frequencies they will allow for the probing of some interesting physical phenomena. Chapter 6 also includes a discussion of the fabrication processes that were tried. It has proven illusive to fabricate InSb particles and to accurately measure the photoexcited decay time of InSb. It was shown, however, that different semiconductors with varying carrier concentrations can support surface plasmons at terahertz frequencies (chapter 5). The measurements conducted on InSb together with data from the literature show that this material is the most suitable for surface plasmon applications in this frequency regime.

In chapter 7 the dispersion of open ended hole arrays were investigated using modal matching modelling, finite element method modelling and phase sensitive experiments. It was shown that these structures support surface modes similar to symmetric and antisymmetric surface plasmon modes on thin metal films at optical frequencies. The discussion was extended to superlenses where it was shown that the surface waves could not perform the same lensing observed at optical frequencies. This identified one of the differences between surface plasmons and so called spoof surface plasmons.

For the future it is hoped that the work described above can help those who follow to fabricate large area arrays of terahertz particle plasmons (chapter 6). It is not

unreasonable to speculate about the feasibility of affordable chemical detectors utilising the physics described in this thesis. These could utilise the small femtosecond lasers now being developed [218], with plasmonic generation possibly cooled using liquid nitrogen and plasmonic sensor elements. Photomodulation of the sensor may allow some tuning of the device to different circumstances. There is also the possibility of probing physical phenomena such as non-locality using small semiconductor particle plasmons.

Generation of terahertz radiation from particle arrays leads to some interesting possibilities. For example, breaking the centrosymetric nature of the samples and conducting experiments at different pressures should add significantly to the optical rectification/photoemission debate. At the time of writing low temperature measurements of islandised films have shown a large increase in the generated signal (≈ 100 times) providing an efficiency comparable to ZnTe. There may also be some feasible method for building a 3D generating structure possibly with layers suspended on graphene which would allow for samples with much higher efficiencies than existing technologies.

8.1 Publications

Some of the above chapters are based on papers which have been previously published.

Chapter 4
The generation of terahertz radiation from plasmonic nanoparticle arrays, D. K. Polyushkin, E. Hendry, E. K. Stone, and W. L. Barnes, Nano Lett., 2011, *11* (11), 4718

Chapter 7
Dispersion of spoof surface plasmons in open-ended metallic hole arrays, E. K. Stone, and E. Hendry, Phys. Rev. B *84*, 035418 (2011)

Other parts of this thesis may be included in publications after submission.

References

[1] Faraday, M. The bakerian lecture: Experimental relations of gold (and other metals) to light. *Philosophical Transactions of the Royal Society of London*, **147**, (1857). 1, 4, 15

[2] Moskovits, M. Surface-enhanced spectroscopy. *Reviews of Modern Physics*, **57**, 783 (1985). 1, 18

[3] Ebbesen, T.W., Lezec, H.J., Ghaemi, H.F., Thio, T., and Wolff, P.A. Extraordinary optical transmission through sub-wavelength hole arrays. *Nature*, **391**, 667 (1998). 2, 117

[4] Nie, S. and Emory, S.R. Probing single molecules and single nanoparticles by surface-enhanced Raman scattering. *Science*, **275**, 1102 (1997). 2, 18

[5] Glass, A., Wokaun, A., Heritage, J., Bergman, J., Liao, P., and Olson, D. Enhanced two-photon fluorescence of molecules adsorbed on silver particle films. *Physical Review B*, **24**, 4906 (1981). 2, 18

[6] Hertz, H. The forces of electric oscillations treated according to maxwell's theory. *Nature*, **39**, 402 (1889). 2

[7] Newton, I. *Opticks, or a treatise of the reflections, refractions, inflections and colours of light*. Biblioteca digital Dioscórides. William Innys (1730). 2

[8] Zernike, F. and Berman, P. Generation of far infrared as a difference frequency. *Physical Review Letters*, **15**, 999 (1965). 2

[9] Faries, D., Gehring, K., Richards, P., and Shen, Y. Tunable far-infrared radiation generated from the difference frequency between two ruby lasers. *Physical Review*, **180**, 363 (1969). 2

[10] Williams, B.S. Terahertz quantum-cascade lasers. *Nature Photonics*, **1**, 517 (2007). 2

[11] Amersfoort, P.W., Best, R.W.B., van der Geer, C.A.J., Mastop, W.J., Meddens, B.J.H., van der Meer, A.F.G., Oepts, D., and van der Wiel, M.J. Felix: the dutch free electron laser for infrared experiments. *Proceedings of EPAC*, page 430 (1988). 2

[12] van Exter, M., Fattinger, C., and Grischkowsky, D. High-brightness terahertz beams characterized with an ultrafast detector. *Applied Physics Letters*, **55**, 337 (1989). 2

[13] Nahata, A., Weling, A.S., and Heinz, T.F. A wideband coherent terahertz spectroscopy system using optical rectification and electro-optic sampling. *Applied Physics Letters*, **69**, 2321 (1996). 2, 19, 21, 22, 27, 49

[14] Dickinson, J.C., Goyette, T.M., Gatesman, A.J., Joseph, C.S., Root, Z.G., Giles, R.H., Waldman, J., and Nixon, W.E. Terahertz imaging of subjects with concealed weapons. *Proceedings of SPIE*, **6212**, 62120Q (2006). 2

[15] De Leebeeck, A., Kumar, L.K.S., de Lange, V., Sinton, D., Gordon, R., and Brolo, A.G. On-chip surface-based detection with nanohole arrays. *Anal. Chem.*, **79**, 4094 (2007). 2

[16] Homola, J. Present and future of surface plasmon resonance biosensors. *Analytical and bioanalytical chemistry*, **377**, 528 (2003). 2, 12

[17] Peale, R.E., Muravjov, A.V., Cleary, J.W., Brusentsova, T., Fredricksen, C.J., Boreman, G.D., Vaks, V.L., Maslovsky, A.V., and Nikifirov, S.D. Terahertz spectroscopy of acetone vapor. *Optical Terahertz Science and Technology*, **MD**, MD13 (2007). 3

[18] Haring Bolívar, P., Nagel, M., Richter, F., Brucherseifer, M., Kurz, H., Bosserhoff, A., and Büttner, R. Label-free THz sensing of genetic sequences: towards 'THz biochips'. *Philos Transact A Math Phys Eng Sci*, **362**, 323 (2004).

[19] Taday, P.F. Applications of terahertz spectroscopy to pharmaceutical sciences. *Philos Transact A Math Phys Eng Sci*, **362**, 351 (2004). 3

[20] Wood, R.W. On a remarkable case of uneven distribution of light in a diffraction grating spectrum. *Proceedings of the Physical Society of London*, **18**, 269 (1902). 4, 11

[21] Lezec, H.J., Degiron, A., Devaux, E., Linke, R.A., Martin-Moreno, L., Garcia-Vidal, F.J., and Ebbesen, T.W. Beaming light from a subwavelength aperture. *Science*, **297**, 820 (2002). 4

[22] Fano, U. The theory of anomalous diffraction gratings and of quasi-stationary waves on metallic surfaces (sommerfeld's waves). *Journal of the Optical Society of America*, **31**, 213 (1941). 4

[23] Economou, E. Surface plasmons in thin films. *Physical Review*, **182**, 539 (1969). 4, 111, 113, 114

[24] Zenneck, J. Über die fortpflanzung ebener elektromagnetischer wellen längs einer ebenen leiterfläche und ihre beziehung zur drahtlosen telegraphie. *Annalen der Physik*, **328**, 846 (1907). 4

[25] Sommerfeld, A. The broadening of the waves and the wireless telegraph. *Annalen Der Physik*, **28**, 665 (1909). 4

[26] Raether, H. *Surface Plasmons*. Spring-Verlag, New York (1986). 4, 5, 11, 16, 77

[27] Barnes, W.L. Surface plasmon–polariton length scales: a route to sub-wavelength optics. *Journal of Optics A Pure and Applied Optics*, **8**, S87 (2006). 7, 8, 10, 57, 68

[28] Hibbins, A.P., Sambles, J.R., and Lawrence, C.R. Excitation of remarkably nondispersive surface plasmons on a nondiffracting, dual-pitch metal grating. *Applied Physics Letters*, **80**, 2410 (2002). 11

[29] Glass, N.E., Maradudin, A.A., and Celli, V. Theory of surface-polariton resonances and field enhancements in light scattering from bigratings. *Journal of the Optical Society of America*, **73**, 1240 (1983). 11

[30] Carron, K.T. Resonances of two-dimensional particle gratings in surface-enhanced raman scattering. *Journal of the Optical Society of America B*, **3**, 430 (1986). 11

[31] Sánchez-Gil, J., García-Ramos, J., and Méndez, E. Near-field electromagnetic wave scattering from random self-affine fractal metal surfaces: Spectral dependence of local field enhancements and their statistics in connection with surface-enhanced raman scattering. *Physical Review B*, **62**, 10515 (2000). 11

[32] Hecht, E. *Optics (4th Edition)*. Addison Wesley, fourth edition (2001). ISBN 0805385665. 11, 23

[33] Otto, A. Excitation of nonradiative surface plasma waves in silver by the method of frustrated total reflection. *Zeitschrift für Physik*, **216**, 398 (1968). 11

[34] Kretschmann, E. and Raether, H. Radiative decay of non radiative surface plasmons excited by light. *Z. Naturforsch.*, **23A**, 2135 (1968). 11

[35] Stewart, C.E., Hooper, I.R., and Sambles, J.R. Surface plasmon differential ellipsometry of aqueous solutions for bio-chemical sensing. *Journal of Physics D: Applied Physics*, **41**, 105408 (2008). 12

[36] Isaac, T.H., Barnes, W.L., and Hendry, E. Determining the terahertz optical properties of subwavelength films using semiconductor surface plasmons. *Applied Physics Letters*, **93**, 241115 (2008). 12, 19, 22, 29, 59, 63, 67, 117

[37] Ashcroft, N.W. and Mermin, D.N. *Solid State Physics*. Thomson Learning, Toronto, first edition (1976). ISBN 0030839939. 12, 13, 15

[38] Kittel, C. *Introduction to Solid State Physics*. John Wiley & Sons, Inc., New York, 6th edition (1986). 13, 57, 58, 59, 65, 70

[39] Paraskevopoulos, K., Hatzikraniotis, E., Vinga, E., Ozer, M., Anagnostopoulos, A., and Polychroniadis, E. n–p transformation in $TlBi_{(1-x)}Sb_xTe_2$ system. *Journal of Alloys and Compounds*, **467**, 65 (2009). 15

[40] Mie, G. Contributions to the optics of turbid media, particularly of colloidal metal solutions. *Annalen der Physik*, **25**, 377 (1908). 16

[41] Bohren, C.F. and Huffman, D.R. *Absorption and Scattering of Light by Small Particles (Wiley Science Paperback Series)*. Wiley-VCH (1998). ISBN 0471293407. 16

[42] Griffiths, D.J. *Introduction to electrodynamics*. Prentice Hall, third edition (1999). ISBN 9780138053260. 17

[43] Hannay, J.H. The clausius-mossotti equation: an alternative derivation. *European Journal of Physics*, **4**, 141 (1983). 17

[44] J P Kottmann, O J F Martin, D.R.S. and Schultz, S. Field polarization and polarization charge distributions in plasmon resonant nanoparticles. *New Journal of Physics*, **2**, 27 (2000). 18

[45] Kelly, K., Coronado, E., Zhao, L., and Schatz, G. The optical properties of metal nanoparticles: The influence of size, shape, and dielectric environment. *Journal Of Physical Chemistry B*, **107**, 668 (2003). 18, 41

[46] Kottmann, J.P. Non-regularly shaped plasmon resonant nanoparticle as localized light source for near-field microscopy. *Journal of Microscopy*, **202**, 60 (2001). 79, 93, 97

[47] Kottmann, J., Martin, O., Smith, D., and Schultz, S. Spectral response of plasmon resonant nanoparticles with a non-regular shape. *Opt. Express*, **6**, 213 (2000). 18, 79, 93, 97

[48] Sosa, I.O., Noguez, C., and Barrera, R.G. Optical properties of metal nanoparticles with arbitrary shapes. *The Journal of Physical Chemistry B*, **107**, 6269 (2003). 18

[49] Grand, J., de la Chapelle, M., Bijeon, J.L., Adam, P.M., Vial, A., and Royer, P. Role of localized surface plasmons in surface-enhanced raman scattering of shape-controlled metallic particles in regular arrays. *Physical Review B*, **72**, 033407 (2005). 18, 45, 77

[50] Auguié, B. and Barnes, W. Collective resonances in gold nanoparticle arrays. *Physical Review Letters*, **101**, 143902 (2008). 18

[51] Auguié, B. and Barnes, W.L. Diffractive coupling in gold nanoparticle arrays and the effect of disorder. *Optics Letters*, **34**, 401 (2009). 18, 33

[52] Gotschy, W., Vonmetz, K., Leitner, A., and Aussenegg, F.R. Thin films by regular patterns of metal nanoparticles: Tailoring the optical properties by nanodesign. *Applied Physics B Laser and Optics*, **63**, 381 (1996). 18

[53] Hulteen, J.C. and Van Duyne, R.P. Nanosphere lithography: A materials general fabrication process for periodic particle array surfaces. *Journal of Vacuum Science & Technology A: Vacuum, Surfaces, and Films*, **13**, 1553 (1995). 18, 39

[54] Grischkowsky, D., Keiding, S., Exter, M.v., and Fattinger, C. Far-infrared time-domain spectroscopy with terahertz beams of dielectrics and semiconductors. *Journal of the Optical Society of America B*, **7**, 2006 (1990). 19, 32

[55] van Exter, M. and Grischkowsky, D. Characterization of an optoelectronic terahertz beam system. *IEEE Transactions on Microwave Theory and Techniques*, **38**, 1684 (1990). 19, 24, 28

[56] Mathis, Y.L., Gasharova, B., and Moss, D. Terahertz radiation at anka, the new synchrotron light source in karlsruhe. *Journal of Biological Physics*, **29**, 313 (2003). 19

[57] Cherkassky, V., Knyazev, B., Kubarev, V., Kulipanov, G., Kurysshev, G., Matveenko, A., Petrov, A., Popik, V., Scheglov, M., and Shevchenko, O. Imaging techniques for a high-power THz free electron laser. *Nuclear Instruments and Methods in Physics Research Section A: Accelerators, Spectrometers, Detectors and Associated Equipment*, **543**, 102 (2005). 19

[58] Lewen, F. Terahertz laser sideband spectroscopy with backward wave oscillators. *Journal of Molecular Spectroscopy*, **183**, 207 (1997). 19

[59] Coherent Legend Elite HE (2008). http://www.coherent.com/products/?1505/Legend-Elite-Series. 19, 21

[60] Drierite - du-cal drierite. Technical report (2011). secure.drierite.com/catalog3/page4d.cfm. 21

[61] Lee, Y.S. *Principles of terahertz science and technology.* Lecture Notes in Physics. Springer (2008). ISBN 9780387095394. 21, 23, 24, 25, 26, 27, 28, 32, 77

[62] Zhao, G., Mors, M.t., Wenckebach, T., and Planken, P.C.M. Terahertz dielectric properties of polystyrene foam. *Journal of the Optical Society of America B*, **19**, 1476 (2002). 21

[63] Wu, Q. and Zhang, X.C. Ultrafast electro-optic field sensors. *Applied Physics Letters*, **68**, 1604 (1996). 22

[64] Wu, Q., Litz, M., and Zhang, X.C. Broadband detection capability of ZnTe electro-optic field detectors. *Applied Physics Letters*, **68**, 2924 (1996). 22, 29

[65] Wu, Q. and Zhang, X.C. 7 terahertz broadband gap electro-optic sensor. *Applied Physics Letters*, **70**, 1784 (1997).

[66] Jepsen, P., Winnewisser, C., Schall, M., Schyja, V., Keiding, S., and Helm, H. Detection of THz pulses by phase retardation in lithium tantalate. *Physical Review E*, **53**, R3052 (1996). 22

[67] Schmuttenmaer, C.A. Exploring dynamics in the far-infrared with terahertz spectroscopy. *ChemInform*, **35**, 1759 (2004). 23

[68] Fattinger, C. and Grischkowsky, D. Terahertz beams. *Applied Physics Letters*, **54**, 490 (1989).

[69] Liu, T.A., Tani, M., and Pan, C.L. THz radiation emission properties of multienergy arsenic-ion-implanted gaas and semi-insulating gaas based photoconductive antennas. *Journal of Applied Physics*, **93**, 2996 (2003).

[70] Auston, D. and Nuss, M. Electrooptical generation and detection of femtosecond electrical transients. *IEEE Journal of Quantum Electronics*, **24**, 184 (1988).

[71] Smith, P., Auston, D., and Nuss, M. Subpicosecond photoconducting dipole antennas. *IEEE Journal of Quantum Electronics*, **24**, 255 (1988).

[72] Hussain, A. and Andrews, S.R. Ultrabroadband polarization analysis of terahertz pulses. *Optics Express*, **16**, 7251 (2008). 23, 28

[73] Zhao, G., Schouten, R.N., van der Valk, N., Wenckebach, W.T., and Planken, P.C.M. Design and performance of a THz emission and detection setup based on a semi-insulating GaAs emitter. *Review of Scientific Instruments*, **73**, 1715 (2002). 24

[74] Ferguson, B. and Zhang, X.C. Materials for terahertz science and technology. *Nature materials*, **1**, 26 (2002). 24, 27

[75] Bass, M., Franken, P., and Ward, J. Optical rectification. *Physical Review*, **138**, A534 (1965). 24, 25, 29

[76] Yajima, T. and Takeuchi, N. Far-infrared difference-frequency generation by picosecond laser pulses. *Japanese Journal of Applied Physics*, **9**, 1361 (1970).

[77] Bass, M., Franken, P., Ward, J., and Weinreich, G. Optical rectification. *Physical Review Letters*, **9**, 446 (1962). 24, 25

[78] Reitz, J., Milford, F., and Christy, R. *Foundations of electromagnetic theory*. Addison-Wesley series in physics. Addison-Wesley Pub. Co. (1960). 25, 33, 60

[79] Jones, N., Norris, C., Nicklin, C., Steadman, P., Baker, S., Johnson, A., and Bennett, S. Atomic structure of the InSb(001)-c(8×2) reconstruction determined by x-ray diffraction. *Surface Science*, **409**, 27 (1998). 26, 67

[80] van der Valk, N.C.J., Wenckebach, T., and Planken, P.C.M. Full mathematical description of electro-optic detection in optically isotropic crystals. *Journal of the Optical Society of America B*, **21**, 622 (2004). 29

[81] Planken, P.C.M., Nienhuys, H.K., Bakker, H.J., and Wenckebach, T. Measurement and calculation of the orientation dependence of terahertz pulse detection in znte. *Journal of the Optical Society of America B*, **18**, 313 (2001). 29

[82] Adam, A.J.L., Brok, J.M., Seo, M.A., Ahn, K.J., Kim, D.S., Kang, J.H., Park, Q.H., Nagel, M., and Planken, P.C.M. Advanced terahertz electric near-field measurements at sub-wavelength diameter metallic apertures. *Optics express*, **16**, 7407 (2008). 29

[83] Castro-Camus, E., Lloyd-Hughes, J., Johnston, M.B., Fraser, M.D., Tan, H.H., and Jagadish, C. Polarization-sensitive terahertz detection by multicontact photoconductive receivers. *Applied Physics Letters*, **86**, 254102 (2005). 29

[84] Bakunov, M.I., Maslov, A.V., and Bodrov, S.B. Phase-matched generation of a terahertz surface wave by a subluminous optical strip. *Journal of Applied Physics*, **98**, 033101 (2005). 29

[85] Hirori, H., Yamashita, K., Nagai, M., and Tanaka, K. Attenuated total reflection spectroscopy in time domain using terahertz coherent pulses. *Japanese Journal of Applied Physics*, **43**, L1287 (2004). 29

[86] *SPICE 3's User Guide* (2009). newton.ex.ac.uk/teaching/cdhw/Electronics2/userguide/. 29

[87] Storey, N. *Electronics: a systems approach*. Pearson Education Canada (2009). ISBN 9780273719182. 30

[88] Edwards, S.J. and Langley, A.J. On producing colours using birefringence property of transparent, colourless stretched cellophane. *Leonardo*, **14**, 187 (1981). 32

[89] HFSS, high-frequency structure simulator versions 10 - 13 finite-element package, Ansoft Corporation, Pittsburgh, PA. (2008-11). 33, 109, 110

[90] Dhatt, G. and Touzot, G. *The Finite Element Method Displayed*. John Wiley & Sons, Chichester (1984). 34

[91] Tretyakov, S. *Analytical modeling in applied electromagnetics*. Artech House electromagnetic analysis series. Artech House (2003). ISBN 9781580533676. 35

[92] Zijlstra, P., Chon, J.W.M., and Gu, M. Five-dimensional optical recording mediated by surface plasmons in gold nanorods. *Nature*, **459**, 410 (2009). 37

[93] Loo, C., Lowery, A., Halas, N., West, J., and Drezek, R. Immunotargeted nanoshells for integrated cancer imaging and therapy. *Nano Lett.*, **5**, 709 (2005). 37

[94] Kim, S., Jin, J., Kim, Y.J., Park, I.Y., Kim, Y., and Kim, S.W. High-harmonic generation by resonant plasmon field enhancement. *Nature*, **453**, 757 (2008). 37

[95] Irvine, S., Dombi, P., Farkas, G., and Elezzabi, A. Influence of the carrier-envelope phase of few-cycle pulses on ponderomotive surface-plasmon electron acceleration. *Physical Review Letters*, **97**, 146801 (2006). 37

[96] Gloskovskii, A., Valdaitsev, D., Cinchetti, M., Nepijko, S., Lange, J., Aeschlimann, M., Bauer, M., Klimenkov, M., Viduta, L., Tomchuk, P., and Schönhense, G. Electron emission from films of Ag and Au nanoparticles excited by a femtosecond pump-probe laser. *Physical Review B*, **77**, 195427 (2008). 37, 49

[97] Kupersztych, J., Monchicourt, P., and Raynaud, M. Ponderomotive acceleration of photoelectrons in surface-plasmon-assisted multiphoton photoelectric emission. *Physical Review Letters*, **86**, 5180 (2001). 37

[98] Kupersztych, J. and Raynaud, M. Anomalous multiphoton photoelectric effect in ultrashort time scales. *Physical Review Letters*, **95**, 147401 (2005). 37

[99] Jackson, J.D. *Classical Electrodynamics Third Edition*. Wiley, third edition (1998). ISBN 047130932X. 37

[100] Kadlec, F., Kuzel, P., and Coutaz, J.L. Optical rectification at metal surfaces. *Optics Letters*, **29**, 2674 (2004). 37, 38

[101] Kadlec, F., Kuzel, P., and Coutaz, J.L. Study of terahertz radiation generated by optical rectification on thin gold films. *Optics Letters*, **30**, 1402 (2005). 37, 38

[102] Welsh, G., Hunt, N., and Wynne, K. Terahertz-pulse emission through laser excitation of surface plasmons in a metal grating. *Physical Review Letters*, **98**, 026803 (2007). 37, 38, 49

[103] Welsh, G.H. and Wynne, K. Generation of ultrafast terahertz radiation pulses on metallic nanostructured surfaces. *Optics Express*, **17**, 2470 (2009). 37, 38, 51

[104] Ramakrishnan, G. and Planken, P.C.M. Percolation-enhanced generation of terahertz pulses by optical rectification on ultrathin gold films. *Opt Lett*, **36**, 2572 (2011). 37, 38

[105] BOOT, H.A.H. and R.-S.-HARVIE, R.B. Charged particles in a non-uniform radio-frequency field. *Nature*, **180**, 1187 (1957). 37

[106] Rácz, P., Irvine, S.E., Lenner, M., Mitrofanov, A., Baltuška, A., Elezzabi, A.Y., and Dombi, P. Strong-field plasmonic electron acceleration with few-cycle, phase-stabilized laser pulses. *Applied Physics Letters*, **98**, 111116 (2011). 37, 53

[107] Ramakrishnan, G., Kumar, N., Planken, P.C.M., Tanaka, D., and Kajikawa, K. Surface plasmon-enhanced terahertz emission from a hemicyanine self-assembled monolayer. *Optics Express*, **20**, 4067 (2012). 38

[108] Polyushkin, D.K., Hendry, E., Stone, E.K., and Barnes, W.L. THz generation from plasmonic nanoparticle arrays. *Nano Lett.*, **11**, 4718 (2011). 38

[109] Gao, Y., Chen, M.K., Yang, C.E., Chang, Y.C., Yin, S., Hui, R., Ruffin, P., Brantley, C., Edwards, E., and Luo, C. Analysis of terahertz generation via nanostructure enhanced plasmonic excitations. *Journal of Applied Physics*, **106**, 074302 (2009). 38

[110] Kümmerlen, J., Leitner, A., Brunner, H., Aussenegg, F.R., and Wokaun, A. Enhanced dye fluorescence over silver island films: analysis of the distance dependence. *Molecular Physics*, **80**, 1031 (1993). 39

[111] Ding, S. Optical percolation and nonlinearity of sputtered ag island films. *Optics Express*, **14**, 1541 (2006). 39

[112] Wustholz, K.L., Henry, A.I., McMahon, J.M., Freeman, R.G., Valley, N., Piotti, M.E., Natan, M.J., Schatz, G.C., and Van Duyne, R.P. Structure-activity relationships in gold nanoparticle dimers and trimers for surface-enhanced raman spectroscopy. *J. Am. Chem. Soc.*, **132**, 10903 (2010). 42

[113] García-Vidal, F. and Pendry, J. Collective theory for surface enhanced raman scattering. *Physical Review Letters*, **77**, 1163 (1996). 43

[114] Jensen, T.R., Malinsky, M.D., Haynes, C.L., and Van Duyne, R.P. Nanosphere lithography: tunable localized surface plasmon resonance spectra of silver nanoparticles. *The Journal of Physical Chemistry B*, **104**, 10549 (2000). 44

[115] Parsons, J., Burrows, C., Sambles, J., and Barnes, W. A comparison of techniques used to simulate the scattering of electromagnetic radiation by metallic nanostructures. *Journal of Modern Optics*, **57**, 356 (2010). 45

[116] Murray, W.A., Suckling, J.R., and Barnes, W.L. Overlayers on silver nanotriangles: Field confinement and spectral position of localized surface plasmon resonances. *Nano Lett.*, **6**, 1772 (2006). 45, 52

[117] Lynch, D, W. and Hunter, W, R. *Handbook of Optical Constants of Solids*. Ed. E. D. Palik, Academic Press Inc. (1985). 45

[118] Irvine, S.E. and Elezzabi, A.Y. Ponderomotive electron acceleration using surface plasmon waves excited with femtosecond laser pulses. *Applied Physics Letters*, **86**, 264102 (2005). 49

[119] Chelvayohan, M. and Mee, C.H.B. Work function measurements on (110), (100) and (111) surfaces of silver. *Journal of Physics C: Solid State Physics*, **15**, 2305 (2000). 50

[120] Tsang, T., Srinivasan-Rao, T., and Fischer, J. Surface-plasmon field-enhanced multiphoton photoelectric emission from metal films. *Physical Review B*, **43**, 8870 (1991). 50, 53

[121] Keldysh, L.V. Ionization in the field of a strong electromagnetic wave. *JETP*, **20**, 1307 (1965). 51

[122] Hao, E. and Schatz, G.C. Electromagnetic fields around silver nanoparticles and dimers. *J Chem Phys*, **120**, 357 (2004). 52

[123] LaVilla, R. and Mendlowitz, H. Optical constants of aluminum in vacuum ultraviolet. *Physical Review Letters*, **9**, 149 (1962). 57

[124] Sambles, J.R., Bradbery, G.W., and Yang, F. Optical excitation of surface plasmons: An introduction. *Contemporary Physics*, **32**, 173 (1991). 57

[125] Yu, P.Y. and Cardona, M. *Fundamentals of Semiconductors: Physics and Materials Properties*. Springer, Berlin (2005). ISBN 3540254706. 58, 59

[126] Rivas, J., Kuttge, M., Bolivar, P., Kurz, H., and Sánchez-Gil, J. Propagation of surface plasmon polaritons on semiconductor gratings. *Physical Review Letters*, **93**, 256804 (2004). 59, 68

[127] Rivas, J., Janke, C., Bolivar, P., and Kurz, H. Transmission of THz radiation through InSb gratings of subwavelength apertures. *Optics Express*, **13**, 847 (2005).

[128] Gómez Rivas, J., Kuttge, M., Kurz, H., Haring Bolivar, P., and Sánchez-Gil, J.A. Low-frequency active surface plasmon optics on semiconductors. *Applied Physics Letters*, **88**, 082106 (2006). 59, 68

[129] Isaac, T., Gómez Rivas, J., Sambles, J., Barnes, W., and Hendry, E. Surface plasmon mediated transmission of subwavelength slits at thz frequencies. *Physical Review B*, **77**, 113411 (2008). 59, 63, 67, 80, 89

[130] Rivas, J.G. and Berrier, A. Terahertz plasmonics with semiconductor surfaces and antennas. In *2009 Asia Pacific Microwave Conference*, page 1293 (2009).

[131] Hendry, E., Garcia-Vidal, F., Martin-Moreno, L., Rivas, J., Bonn, M., Hibbins, A., and Lockyear, M. Optical control over surface-plasmon-polariton-assisted thz transmission through a slit aperture. *Physical Review Letters*, **100**, 123901 (2008). 59

[132] Berrier, A., Ulbricht, R., Bonn, M., and Rivas, J.G. Ultrafast active control of localized surface plasmon resonances in silicon bowtie antennas. *Optics Express*, **18**, 23226 (2010). 59

[133] Ulrich, R. and Tacke, M. Submillimeter waveguiding on periodic metal structure. *Applied Physics Letters*, **22**, 251 (1973). 61

[134] Liu, P. and Maan, J. Optical properties of InSb between 300 and 700 K. II. Magneto-optical experiments. *Physical Review B*, **47**, 16279 (1993). 63

[135] Oskooi, A.F., Roundy, D., Ibanescu, M., Bermel, P., Joannopoulos, J.D., and Johnson, S.G. Meep: A flexible free-software package for electromagnetic simulations by the fdtd method. *Computer Physics Communications*, **181**, 687 (2010). 63

[136] Schottky, W.F. and Bever, M.B. On the thermodynamic properties of the iii–v compounds InSb, GaSb, and InAs. *Acta Metallurgica*, **6**, 320 (1958). 65

[137] Leibiger, G., Gottschalch, V., Rheinländer, B., Šik, J., and Schubert, M. Model dielectric function spectra of GaAsN for far-infrared and near-infrared to ultraviolet wavelengths. *Journal of Applied Physics*, **89**, 4927 (2001). 66, 67

[138] Jeon, T.I. and Grischkowsky, D. Characterization of optically dense, doped semiconductors by reflection THz time domain spectroscopy. *Applied Physics Letters*, **72**, 3032 (1998). 66, 67

[139] Huggard, P.G., Cluff, J.A., Moore, G.P., Shaw, C.J., Andrews, S.R., Keiding, S.R., Linfield, E.H., and Ritchie, D.A. Drude conductivity of highly doped gaas at terahertz frequencies. *Journal of Applied Physics*, **87**, 2382 (2000). 66, 67, 68

[140] Hendry, E., Koeberg, M., Pijpers, J., and Bonn, M. Reduction of carrier mobility in semiconductors caused by charge-charge interactions. *Physical Review B*, **75**, 233202 (2007). 66, 67

[141] Dixon, J. and Riedl, H. Electric-susceptibility hole mass of lead telluride. *Physical Review*, **138**, A873 (1965). 66, 67

[142] Howells, S.C. and Schlie, L.A. Transient terahertz reflection spectroscopy of undoped InSb from 0.1 to 1.1 THz. *Applied Physics Letters*, **69**, 550 (1996). 66, 67

[143] van Exter, M. and Grischkowsky, D. Carrier dynamics of electrons and holes in moderately doped silicon. *Physical Review B*, **41**, 12140 (1990). 66, 68

[144] Nashima, S., Morikawa, O., Takata, K., and Hangyo, M. Measurement of optical properties of highly doped silicon by terahertz time domain reflection spectroscopy. *Applied Physics Letters*, **79**, 3923 (2001). 66

[145] Pashkin, A., Kempa, M., Němec, H., Kadlec, F., and Kužel, P. Phase-sensitive time-domain terahertz reflection spectroscopy. *Review of Scientific Instruments*, **74**, 4711 (2003). 66, 69

[146] Vaicikauskas, V. Far infrared surface electromagnetic waves propagation on A^3B^5 semiconductors. *International Journal of Infrared and Millimeter Waves*, **15**, 303 (1994). 67

[147] Tsai, T.R., Chen, S.J., Chang, C.F., Hsu, S.H., Lin, T.Y., and Chi, C.C. Terahertz response of GaN thin films. *Optics Express*, **14**, 4898 (2006). 67

[148] Metzger, W.K., Wanlass, M.W., Gedvilas, L.M., Verley, J.C., Carapella, J.J., and Ahrenkiel, R.K. Effective electron mass and plasma filter characterization of n-type InGaAs and InAsP. *Journal of Applied Physics*, **92**, 3524 (2002). 67

[149] Yang, T., Cheng, Y., Wang, J., and Chuanfeng, Z. Optical and transport properties of InSb thin films grown on gaas by metalorganic chemical vapor deposition. *Thin Solid Films*, **498**, 158 (2006). 67

[150] Sanderson, R. Far infrared optical properties of indium antimonide. *Journal of Physics and Chemistry of Solids*, **26**, 803 (1965). 67

[151] Hu, Z.G., Rinzan, M.B.M., Matsik, S.G., Perera, A.G.U., Von Winckel, G., Stintz, A., and Krishna, S. Optical characterizations of heavily doped p-type $Al_xGa_{1-x}As$ and GaAs epitaxial films at terahertz frequencies. *Journal of Applied Physics*, **97**, 093529 (2005). 68

[152] Belovolov, M.I., Vavilov, V.S., Egorov, V.D., and Kulakovskii, V.D. Plasma reflection in pure and doped bismuth-antimony alloys. *Soviet Physics Journal*, **19**, 139 (1976). 68

[153] Ahn, H., Pan, C.L., and Gwo, S. Terahertz emission and spectroscopy on inn epilayer and nanostructure. In *Proceedings of SPIE*, page 72160T (2009). 68

[154] Barnes, W.L., Kitson, S.C., Preist, T.W., and Sambles, J.R. Photonic surfaces for surface-plasmon polaritons. *Journal of the Optical Society of America A*, **14**, 1654 (1997). 68

[155] Giannattasio, A., Hooper, I.R., and Barnes, W.L. Dependence on surface profile in grating-assisted coupling of light to surface plasmon-polaritons. *Optics Communications*, **261**, 291 (2006). 68

[156] Watts, R.A., Hibbins, A.P., and Sambles, J.R. The influence of grating profile on surface plasmon polariton resonances recorded in different diffracted orders. *Journal of Modern Optics*, **46**, 2157 (1999). 68, 69

[157] Padilla, W.J., Taylor, A.J., and Averitt, R.D. Dynamical electric and magnetic metamaterial response at terahertz frequencies. *Physical Review Letters*, **96**, 107401 (2006). 70, 98

[158] Littler, C.L. and Seiler, D.G. Temperature dependence of the energy gap of InSb using nonlinear optical techniques. *Applied Physics Letters*, **46**, 986 (1985). 70

[159] Grober, R.D., Drew, H.D., Burdge, G.L., and Bennett, B.S. Direct measurement of the recombination rates in bulk InSb by time-resolved photoluminescence. *Journal of Applied Physics*, **71**, 5140 (1992). 71, 72

[160] Sundaram, S.K. and Mazur, E. Inducing and probing non-thermal transitions in semiconductors using femtosecond laser pulses. *Nat Mater*, **1**, 217 (2002). 72, 74

[161] O'Neil, M., Marohn, J., and McLendon, G. Dynamics of electron-hole pair recombination in semiconductor clusters. *The Journal of Physical Chemistry*, **94**, 4356 (1990). 74

[162] Gupta, S., Whitaker, J., and Mourou, G. Ultrafast carrier dynamics in iii-v semiconductors grown by molecular-beam epitaxy at very low substrate temperatures. *IEEE Journal of Quantum Electronics*, **28**, 2464 (1992). 74

[163] Hoffmann, M., Hebling, J., Hwang, H., Yeh, K.L., and Nelson, K. Impact ionization in InSb probed by terahertz pump—terahertz probe spectroscopy. *Physical Review B*, **79**, 161201 (2009). 74

[164] Hooper, I. and Sambles, J. Dispersion of surface plasmon polaritons on short-pitch metal gratings. *Physical Review B*, **65** (2002). 77, 78

[165] Murray, W. and Barnes, W. Plasmonic materials. *Advanced Materials*, **19**, 3771 (2007). 77

[166] Landau, L.D. and Lifshitz, E.M. *Electrodynamics of continuous media*. Pergamon international library of science, technology, engineering, and social studies. Pergamon (1984). ISBN 9780080302751. 77

[167] Tan, W.C., Preist, T., Sambles, J., and Wanstall, N. Flat surface-plasmon-polariton bands and resonant optical absorption on short-pitch metal gratings. *Physical Review B*, **59**, 12661 (1999). 78

[168] Sendur, K. and Challener, W. Near-field radiation of bow-tie antennas and apertures at optical frequencies. *Journal of Microscopy*, **210**, 279 (2003). 79

[169] Chang, K.M., Luo, J.J., Chiang, C.D., and Liu, K.C. Wet etching characterization of InSb for thermal imaging applications. *Japanese Journal of Applied Physics*, **45**, 1477 (2006). 80

[170] van Dijk, M.A., Tchebotareva, A.L., Orrit, M., Lippitz, M., Berciaud, S., Lasne, D., Cognet, L., and Lounis, B. Absorption and scattering microscopy of single metal nanoparticles. *Phys Chem Chem Phys*, **8**, 3486 (2006). 85

[171] Frost, F. Reactive ion beam etching of InSb and InAs with ultrasmooth surfaces. *Semiconductor Science and Technology*, **13**, 523 (1998). 86

[172] Mileham, J.R. Dry etching of GaSb and InSb in CH4/H2/Ar. *Semiconductor Science and Technology*, **12**, 338 (1997). 86

[173] Indium antimonide etching (InSb): Oxford instruments. *goo.gl/IXDwx* (6th February 2012). 86

[174] Hays, D. Selective dry etching using inductively coupled plasmas part i. GaAs/AlGaAs and GaAs/InGaP. *Applied Surface Science*, **147**, 125 (1999). 86

[175] Marxer, C., Thio, C., Gretillat, M., Derooij, N., Battig, R., Anthamatten, O., Valk, B., and Vogel, P. Vertical mirrors fabricated by deep reactive ion etching for fiber-optic switching applications. *Journal Of Microelectromechanical Systems*, **6**, 277 (1997). 86

[176] Jansen, H., de Boer, M., Burger, J., Legtenberg, R., and Elwenspoek, M. The black silicon method ii:the effect of mask material and loading on the reactive ion etching of deep silicon trenches. *Microelectronic Engineering*, **27**, 475 (1995). 89

[177] Fromm, D.P., Sundaramurthy, A., Schuck, P.J., Kino, G., and Moerner, W.E. Gap-dependent optical coupling of single "bowtie" nanoantennas resonant in the visible. *Nano Letters*, **4**, 957 (2004). 91

[178] Schuck, P.J., Fromm, D.P., Sundaramurthy, A., Kino, G.S., and Moerner, W.E. Improving the mismatch between light and nanoscale objects with gold bowtie nanoantennas. *Physical Review Letters*, **94** (2005).

[179] Gunnarsson, L., Rindzevicius, T., Prikulis, J., Kasemo, B., Käll, M., Zou, S., and Schatz, G.C. Confined plasmons in nanofabricated single silver particle pairs: experimental observations of strong interparticle interactions. *J Phys Chem B*, **109**, 1079 (2005).

[180] Zoriniants, G. and Barnes, W.L. Fluorescence enhancement through modified dye molecule absorption associated with the localized surface plasmon resonances of metallic dimers. *New Journal of Physics*, **10**, 105002 (2008). 91

[181] Chen, S. and Carroll, D.L. Synthesis and characterization of truncated triangular silver nanoplates. *Nano Letters*, **2**, 1003 (2002). 94

[182] Pendry, J.B., Martín-Moreno, L., and Garcia-Vidal, F.J. Mimicking surface plasmons with structured surfaces. *Science*, **305**, 847 (2004). 99, 106, 107, 114

[183] Garcia-Vidal, F.J., Martín-Moreno, L., and Pendry, J.B. Surfaces with holes in them: new plasmonic metamaterials. *Journal of Optics A: Pure and Applied Optics*, **7**, S97 (2005). 106, 107, 111, 114

[184] Hendry, E., Hibbins, A., and Sambles, J. Importance of diffraction in determining the dispersion of designer surface plasmons. *Physical Review B*, **78**, 235426 (2008). 99, 100, 102, 107, 108, 111, 112, 114

[185] García de Abajo, F. and Sáenz, J. Electromagnetic surface modes in structured perfect-conductor surfaces. *Physical Review Letters*, **95**, 233901 (2005). 99

[186] Lan, Y.C. and Chern, R.L. Surface plasmon-like modes on structured perfectly conducting surfaces. *Optics Express*, **14**, 11339 (2006).

[187] Shen, L., Chen, X., and Yang, T.J. Terahertz surface plasmon polaritons on periodically corrugated metal surfaces. *Optics Express*, **16**, 3326 (2008). 111

[188] Maier, S.A. and Andrews, S.R. Terahertz pulse propagation using plasmon-polariton-like surface modes on structured conductive surfaces. *Applied Physics Letters*, **88**, 251120 (2006). 99

[189] Hibbins, A.P., Evans, B.R., and Sambles, J.R. Experimental verification of designer surface plasmons. *Science*, **308**, 670 (2005). 99, 111

[190] Hibbins, A.P., Hendry, E., Lockyear, M.J., and Sambles, J.R. Prism coupling to 'designer' surface plasmons. *Optics Express*, **16**, 20441 (2008). 99, 108

[191] Williams, C.R., Andrews, S.R., Maier, S.A., Fernández-Domínguez, A.I., Martín-Moreno, L., and García-Vidal, F.J. Highly confined guiding of terahertz surface plasmon polaritons on structured metal surfaces. *Nature Photonics*, **2**, 175 (2008). 99, 111

[192] Pendry, J.B. Negative refraction makes a perfect lens. *Physical Review Letters*, **85**, 3966 (2000). 100, 114, 115, 116

[193] Fang, N., Lee, H., Sun, C., and Zhang, X. Sub-diffraction-limited optical imaging with a silver superlens. *Science*, **308**, 534 (2005). 100, 115

[194] Giannattasio, A., Hooper, I.R., and Barnes, W.L. Transmission of light through thin silver films via surface plasmon-polaritons. *Optics Express*, **12**, 5881 (2004).

[195] Smith, D.R., Schurig, D., Rosenbluth, M., Schultz, S., Ramakrishna, S.A., and Pendry, J.B. Limitations on subdiffraction imaging with a negative refractive index slab. *Applied Physics Letters*, **82**, 1506 (2003). 100, 107, 113, 115

[196] Isaac, T., Barnes, W., and Hendry, E. Surface-mode lifetime and the terahertz transmission of subwavelength hole arrays. *Physical Review B*, **80**, 115423 (2009). 100, 117, 118

[197] Hibbins, A., Lockyear, M., Hooper, I., and Sambles, J. Waveguide arrays as plasmonic metamaterials: Transmission below cutoff. *Physical Review Letters*, **96**, 073904 (2006). 100

[198] Hooper, I. and Sambles, J. Coupled surface plasmon polaritons on thin metal slabs corrugated on both surfaces. *Physical Review B*, **70**, 045421 (2004). 101, 108

[199] Bravo-Abad, J., Martín-Moreno, L., García-Vidal, F., Hendry, E., and Gómez Rivas, J. Transmission of light through periodic arrays of square holes: From a metallic wire mesh to an array of tiny holes. *Physical Review B*, **76**, 241102 (2007). 102

[200] McPhedran, R.C., Derrick, G.H., and Botten, L.C. *Electromagnetic Theory of Gratings*. Springer-Verlag, Berlin (1980). ISBN 0387101934 9780387101934. 102

[201] Pozar, D.M. *Microwave engineering*. Wiley (1997). ISBN 9780471170969. 102

[202] Anritsu, VectorStar MS4644A (2010). downloadfiles.anritsu.com/Files/en-US/Manuals/Datasheets/11410-00432.pdf. 109

[203] Jung, J., García-Vidal, F., Martín-Moreno, L., and Pendry, J. Holey metal films make perfect endoscopes. *Physical Review B*, **79**, 153407 (2009). 116

[204] de Dood, M., Driessen, E., Stolwijk, D., and van Exter, M. Observation of coupling between surface plasmons in index-matched hole arrays. *Physical Review B*, **77**, 115437 (2008). 117

[205] Cao, H. and Nahata, A. Resonantly enhanced transmission of terahertz radiation through a periodic array of subwavelength apertures. *Optics Express*, **12**, 1004 (2004). 117

[206] Miyamaru, F. and Hangyo, M. Finite size effect of transmission property for metal hole arrays in subterahertz region. *Applied Physics Letters*, **84**, 2742 (2004).

[207] O'Hara, J.F., Averitt, R.D., and Taylor, A.J. Terahertz surface plasmon polariton coupling on metallic gratings. *Optics Express*, **12**, 6397 (2004).

[208] Qu, D., Grischkowsky, D., and Zhang, W. Terahertz transmission properties of thin, subwavelength metallic hole arrays. *Opt Lett*, **29**, 896 (2004).

[209] Hendry, E., Lockyear, M., Rivas, J., Kuipers, L., and Bonn, M. Ultrafast optical switching of the THz transmission through metallic subwavelength hole arrays. *Physical Review B*, **75**, 235305 (2007). 117

[210] Beruete, M., Sorolla, M., Campillo, I., Dolado, J.S., Martín-Moreno, L., Bravo-Abad, J., and García-Vidal, F.J. Enhanced millimeter-wave transmission through subwavelength hole arrays. *Optics Letters*, **29**, 2500 (2004). 117

[211] Caglayan, H., Bulu, I., and Ozbay, E. Extraordinary grating-coupled microwave transmission through a subwavelength annular aperture. *Opt Express*, **13**, 1666 (2005). 117

[212] Lee, H.S., Yoon, Y.T., Lee, S.s., Kim, S.H., and Lee, K.D. Color filter based on a subwavelength patterned metal grating. *Optics Express*, **15**, 15457 (2007). 117

[213] Dhawan, A., Gerhold, M.D., and Muth, J.F. Plasmonic structures based on subwavelength apertures for chemical and biological sensing applications. *IEEE Sensors Journal*, **8**, 942 (2008). 117

[214] Beruete, M., Sorolla, M., Campillo, I., and Dolado, J. Increase of the transmission in cut-off metallic hole arrays. *IEEE Microwave and Wireless Components Letters*, **15**, 116 (2005). 117

[215] Pan, C.L., Hsieh, C.F., Pan, R.P., Tanaka, M., Miyamaru, F., Tani, M., and Hangyo, M. Control of enhanced THz transmission through metallic hole arrays using nematic liquid crystal. *Optics Express*, **13**, 3921 (2005). 117

[216] Genet, C., van Exter, M., and Woerdman, J. Fano-type interpretation of red shifts and red tails in hole array transmission spectra. *Optics Communications*, **225**, 331 (2003). 117

[217] Barnes, W., Preist, T., Kitson, S., and Sambles, J. Physical origin of photonic energy gaps in the propagation of surface plasmons on gratings. *Physical Review B*, **54**, 6227 (1996). 118

[218] Schultz, M., Karow, H., Prochnow, O., Wandt, D., Morgner, U., and Kracht, D. All-fiber ytterbium femtosecond laser without dispersion compensation. *Optics Express*, **16**, 19562 (2008). 122